Raman Microspectroscopy for *in-situ* Measurement of Concentration Polarization in Nanofiltration

zur Erlangung des akademischen Grades eines
DOKTORS DER INGENIEURWISSENSCHAFTEN (Dr.-Ing.)

von der KIT-Fakultät für Chemieingenieurwesen und Verfahrenstechnik des
Karlsruher Instituts für Technologie (KIT)
genehmigte

DISSERTATION

von

Dipl. Ing. Oliver Jung
aus Dresden

Tag der mündlichen Prüfung: 27.11.2020
Erstgutachter: Prof. Dr. Harald Horn
Zweitgutachter: Prof. Dr. Cristian Picioreanu

Acknowledgements

I would like to thank Prof. Harald Horn for giving me the opportunity to do my doctorate in his department and under his guidance. I especially appreciate his open and pragmatic leadership as well as his knowledge and enthusiasm for his work. Above all, I am grateful that he has established a friendly working relationship within the institute and has shown a sincere interest in the success of me and my colleagues.

I would especially like to thank Dr. Cristian Picioreanu for the general idea to use Raman microspectroscopy for direct measurement of the concentration polarization layer as well as Dr. Michael Wagner, Dr. Florencia Saravia and Prof. Harald Horn for their help in setting up this research. Florencia has been a dedicated, knowledgeable and very supportive supervisor. For this and for her guidance throughout my doctoral studies I am extremely grateful.

Furthermore, I want to thank Stefan Heißler for introducing me to the world of vibrational spectroscopy and his technical support with Raman equipment and measurements, Alfred Herbst and colleagues for their expertise and enthusiasm in constructing a very special flow cell, as well as my fellow colleagues for their supportive attitudes, inspiring work, helpful discussions and joint leisure activities.

I would like to thank Ursula Schäfer and Sylvia Heck for their help and support in all administrative matters as well as for their amicable personalities.

I want to thank Dr. Gudrun Abbt-Braun for all she is doing for the students and the EBI. Her work ethic and organization are exemplary.

My special thanks go to Dr. Andrea Hille-Reichel and Dr. Ewa Borowska for being my friends, supporters and exceptional conversationalists.

Finally, I would like to thank my mother and brother for their unconditional love and support throughout my life. My partner Lisa has patiently supported me and joined me on my journey for the past years. For this and for her continuing love I am especially grateful.

Abstract

Concentration polarization (CP) is a phenomenon of mass transport in membrane feed channels. It occurs on a microscale and involves charged and non-charged materials, which are dissolved in the water matrix. Thus, CP is particularly hard to observe. Consequently, general research applies mostly indirect methods to study the phenomenon and focuses on parameters, which are more accessible, yet allow conclusions about the fundamental mechanisms. This work takes a direct approach and establishes a measurement concept to study CP *in-situ*.

In this work, a laboratory flat-sheet cross-flow nanofiltration (NF) membrane unit was designed to measure the concentration polarization layer (CPL) of sulfate *in-situ* using Raman micro-spectroscopy (RM). The focus of this work is to introduce RM as a new tool for the study of mass transport inside membrane feed channels for NF and reverse osmosis (RO) applications. Thus, this work presents a proof-of-concept for RM to locally resolve the CPL in a membrane unit representative of commonly applied RO/NF spiral wound modules (feed channel height about 0.7 mm, equipped with feed spacer).

The NF membrane unit was operated at constant system pressure of 10 bar with a feed of aqueous magnesium sulfate solution. General filtration performance parameters were recorded, i.e. recovery, permeate flux and permeate conductivity. Membrane rejection towards magnesium sulfate was at least 96%. CPL's were measured for sulfate concentrations of 10 and 20 $g \cdot L^{-1}$ in the feed with cross-flow velocity ranging from 0.004 to 0.2 $m \cdot s^{-1}$ at multiple positions along the feed channel, with and without the presence of a commercial feed spacer. 1D depth profiles as well as 3D scans of the CPL were obtained. The RM measurements were consistent with filtration performance parameters showing increased sulfate concentrations at the membrane surface along with increased permeate recovery. At a cross-flow velocity of 0.004 $m \cdot s^{-1}$, an influence of membrane orientation was observed. Filtration against gravitational force showed increased permeate flux and permeate quality. The RM measurements revealed improved mass transport in the feed channel consistent with Rayleigh-Taylor-Instability (RTI), a phenomenon of natural convection. Thus, this study also presents the first time RTI has been measured *in-situ* in a NF system. The concentration distribution inside spacer elements showed great similarity with simulation results of velocity distributions in spacer filled channels presented in published literature.

The applicability of RM to study combined membrane fouling was investigated by measuring the influence of biofouling on CP. The NF membrane unit was subjected to enhanced biofouling conditions with a culture of *Bacillus subtilis*. Optical coherence tomography (OCT) was used

for analysis of the biofouling layer. It was found that biofilm properties were connected to operational parameters of membrane filtration. CPL's were measured with RM for four biofouling layers of varying thickness ranging from 20 to 100 µm. The results confirmed biofilm enhanced osmotic pressure (BEOP) as a mechanism for flux decline in biofouling.

The ability of RM to provide accurate concentration profiles is discussed thoroughly throughout this work. Spherical aberration due to refraction presents one of the main challenges of the measurement concept causing loss in signal intensity and deterioration of depth resolution. Complex flow fields introducing variations in refractive power along the optical axis introduce further measurement uncertainty, leading to underestimation of concentration values. Variations of biofilm thickness due to compressibility conflicts with the experimental methodology and causes overestimation of concentration values with thicker biofouling layers.

This work presents locally resolved and directly measured concentration profiles of the concentration boundary layer in a NF membrane feed channel. The proposed measurement concept is readily available, user friendly and permits application of feed spacers and the study of combined fouling phenomena.

Zusammenfassung

Konzentrationspolarisation (CP) beschreibt ein Phänomen des Stofftransports gelöster Teilchen an der Membranoberfläche druckbetriebener Membrananlagen. Die sich bildende Grenzschicht hat eine Dicke in der Größenordnung von Mikrometern. Daher ist CP experimentell nur schwer zugänglich, weshalb das Phänomen in der allgemeinen Forschung meist mit indirekten Methoden untersucht wird. Diese Arbeit verfolgt jedoch einen direkten Ansatz und stellt ein neues Messkonzept für die non-invasive Untersuchung der CP *in-situ* vor.

Mittels Raman-Mikrospektroskopie (RM) wurde die Konzentrationspolarisationsgrenzschicht (CPL) von Sulfat im Labor *in-situ* gemessen. Dafür wurde eigens eine Nanofiltrations-(NF)-Flachkanalzelle entwickelt, die es erlaubt die CPL in einer Umgebung zu messen, welche repräsentativ für in der Praxis verwendete Wickelmodule ist (Kanalhöhe 0.7 mm, ausstattbar mit kommerziellen Spacern). Ziel dieser Arbeit ist es, RM als neue Messtechnik für die ortsaufgelöste Untersuchung von Konzentrationsgradienten in der NF und Umkehrosmose (RO) vorzustellen.

Die NF-Membrananlage wurde mit einer Modelllösung (Magnesiumsulfat gelöst in demineralisiertem Wasser) bei einem konstanten Systemdruck von 10 bar betrieben. Übliche Messparameter zur Bestimmung der Filtrationsleistung, u.a. Ausbeute, Leitfähigkeit im Permeat etc., wurden aufgezeichnet. Der Membranrückhalt betrug mindestens 96%. Konzentrationsprofile wurden mit und ohne Spacer für Sulfatkonzentrationen von 10 und 20 $g \cdot L^{-1}$ im Zulauf an mehreren Positionen entlang des Membrankanals gemessen. Die Strömungsgeschwindigkeit wurde im Bereich 0,004 bis 0,2 $m \cdot s^{-1}$ variiert, wodurch eine Ausbeute zwischen 0.5 und 31% erreicht wurde. Es wurden sowohl 1D-Tiefenprofile als auch 3D-Scans durchgeführt. Die Messergebnisse zeigten übereinstimmend, dass eine höhere Ausbeute zu einer Konzentrationserhöhung an der Membranoberfläche führt. Zudem wurde bei Strömungsgeschwindigkeiten in der Größenordnung $mm \cdot s^{-1}$, ein Einfluss der Membranorientierung beobachtet. Filtration entgegen der Schwerkraft hatte eine höhere Ausbeute und Permeatqualität zur Folge. Die RM Messungen zeigten, dass dafür ein verbesserter Stofftransport an der Membranoberfläche durch natürliche Konvektion (Rayleigh-Taylor-Instabilität, RTI) verantwortlich ist. Damit wurde hierin auch erstmals RTI in einem NF-System *in-situ* gemessen. Bei den RM Messungen mit Spacer zeigte sich bei geringen Strömungsgeschwindigkeiten eine charakteristische Konzentrationsverteilung. Der Vergleich mit simulierten Strömungsprofilen in der Fachliteratur zeigte eine große Ähnlichkeit zwischen Simulations- und Messergebnissen.

Inwieweit RM auch auf die Untersuchung komplexer Foulingphänomene in der Membranfiltration angewendet werden kann, wurde anhand von Biofouling untersucht. Dazu wurde die NF-Anlage mit einer Nährlösung betrieben, welcher Kulturen von *Bacillus subtilis* zugesetzt wurden. Ziel war es, den Einfluss eines Biofilms an der Membranoberfläche auf die CPL zu untersuchen. Zur Analyse des Biofilms wurde die optische Kohärenztomographie (OCT) verwendet. Dabei wurde festgestellt, dass die mechanischen Eigenschaften des Biofilms mit den Betriebsparametern der Membranfiltration zusammenhängen. Insbesondere führten Änderungen des Permeatflusses zu Änderungen der Biofilmdicke durch Kompression und Relaxation. Es wurden Konzentrationsprofile für vier Biofilme unterschiedlicher Dicke im Bereich von 20 bis 100 µm gemessen. Die Ergebnisse bestätigten, dass Biofilme zu einer Erhöhung der Salzkonzentration an der Membranoberfläche führen und damit weitere Foulingtypen, insbesondere Scaling, gefördert werden.

Die Möglichkeiten und Schwierigkeiten der Messmethode werden durchgängig kritisch diskutiert. Sphärische Aberration aufgrund der Lichtbrechung beim Durchgang durch verschiedene Medien mit unterschiedlichen Brechungsindizes stellt eine der größten Herausforderungen für das Messprinzip dar. Sie führt zu Verlust von Signalintensität und hat eine Verminderung der Tiefenschärfe zur Folge. Komplexe Strömungsfelder, welche eine Schichtung von Salzlösung unterschiedlicher Brechkraft zur Folge haben, führen zu einer Unterbewertung der Salzkonzentration an der Membranoberfläche. Die beobachtete Komprimierbarkeit der Biofilme stellt eine weitere Problematik für die Messmethodik dar und hat bei größeren Filmdicken eine deutliche Überbewertung der Salzkonzentration an der Membranoberfläche zur Folge.

In dieser Arbeit wurden Konzentrationsprofile in der Grenzschicht über einer NF Membran direkt, non-invasiv und ortsaufgelöst gemessen. Das vorgeschlagene Messkonzept ist praktisch nutzbar, benutzerfreundlich und erlaubt darüber hinaus die Nutzung von Spacern, sowie die Untersuchung komplexer Foulingphänomene.

Table of Contents

List of Figures

List of Tables

List of Abbreviations

BEOP	biofilm enhanced osmotic pressure
CP	concentration polarization
CPF	concentration polarization factor
CPL	concentration polarization layer
EPS	extracellular polymeric substances
FWHM	full width at half maximum
KHI	Kelvin-Helmholz-Instability
NF	nanofiltration
OCT	optical coherence tomography
PSF	point spread function
RM	Raman microspectroscopy
RTI	Rayleigh-Taylor-Instability
RO	reverse osmosis
TLV	threshold limit value
TMP	transmembrane pressure

Terminology

Concentration Polarization Layer (CPL) means the concentration boundary layer in membrane filtration caused by the phenomenon of concentration polarization, an accumulation of rejected solute at the membrane surface during permeate production.

Full Width At Half Maximum (FWHM) is a measure for the depth resolution in microscopy. It is defined as the width of the point spread function at half its maximum intensity.

Point Spread Function (PSF) is the intensity signal over *z* (optical axis) generated by a point source recorded at the detector of a microscope.

Membrane Signal means the Raman intensity of selected Raman bands allocated specifically to the membrane.

Raman Intensity is the integral area of a Raman band.

Sulfate Signal means the Raman intensity of the Raman band allocated to the linear stretching vibrational mode (1^{st} mode) of sulfate.

Effective Pressure means the ratio of system pressure to osmotic pressure of the feed solution. A positive effective pressure means that osmotic pressure is overcome and permeate is produced. If effective pressure is negative then back diffusion takes place. An effective pressure of 0 bar means that permeate flux is zero.

System Pressure means the pressure at the inlet of the membrane unit. System pressure is defined as excess pressure, meaning that 1 bar absolute is recorded as 0 bar system pressure. With no concentration polarization present, system pressure is equal to transmembrane pressure.

Transmembrane Pressure (TMP) means the pressure difference between membrane walls at the feed and permeate side. Without concentration polarization TMP is equal to system pressure. Concentration polarization diminishes TMP without effecting system pressure.

1 Introduction

Inside the vast field of membrane separation processes involving fluids, this work focuses on membrane filtration for water treatment and, more specifically, picks nanofiltration as a model process. Membrane filtration has quickly become the most effective and economical method of water and wastewater treatment available (Hamingerova et al. 2015). With its ability to remediate stresses in water scarce regions with access to sea and brackish water, water desalination has historically been one of the main drivers for technological development. Today, about 80% of the total desalination plants are reverse osmosis installations (Anis et al. 2019). However, application of membrane-based water and wastewater treatment is by no means limited to regions with severe water scarcity or with a lack of safe drinking water. Membranes are replacing traditional means of water treatment and exploring further fields of application also in established markets. Improvements in detection sensitivity of water contaminants, increased desire and regulations to reuse waste water with complete removal of anthropogenic contaminants such as pesticides, hormones, etc., increasing demand for advanced separation techniques in life sciences, pharmaceuticals and food industry are among today's drivers for membrane implementation in regions such as Europe (Hamingerova et al. 2015, Van der Bruggen et al. 2008).

1.1 Nanofiltration

Membrane processes are based on the fundamental ability to control permeation of the membrane. Hence, membranes in water treatment are selective to which materials can permeate, also called semi-permeable. Membrane processes are classified according to the size of the material they reject. Microfiltration (MF) rejects materials in the range of 0.1 to 10 µm which are mainly suspended solids but also bacteria. Ultrafiltration (UF) removes materials up to 30 nm, e.g. proteins and polysaccharides. Nanofiltration (NF) can reject organic matter and viruses while reverse osmosis (RO) rejects almost all water impurities (Anis et al. 2019, Hamingerova et al. 2015). Due to the size of the materials rejected, MF and UF fouling and rejection mechanism differ from the dense membranes relevant for this work as the rejected material is too large to be largely affected by Brownian diffusion. The removal characteristics and associated operational requirements, e.g. energy consumption, dictate the fields of applicability of these different classes of membrane processes.

Dense membranes have a higher energy consumption but offer superior purification and removal of contaminants such as microorganisms and viruses, dissolved organics and organic

micro pollutants as well as removal of hardness and salinity. Nanofiltration specifically has an interesting range of applicability due to its removal characteristics (Oatley-Radcliffe et al. 2017). With a pore size of about 1 nm and molecular weight cut off between 100 and 500 Dalton, NF has very high retention of dissolved organics and multivalent ions, while monovalent ions mostly pass through the membrane. Hence, NF is applied where fractionation and selective removal of solutes in complex process streams is desired, such as pretreatment in seawater desalination (Anis et al. 2019, Jamaly et al. 2014, Zhou et al. 2015), fractionation and concentration of food products (Nath et al. 2018), wastewater reuse (Egea-Corbacho et al. 2019, Roccaro 2018) and the treatment of hard water to yield soft water (Fang et al. 2013, Labban et al. 2017, Van der Bruggen et al. 2001).

NF and RO membranes owe their existence to the inception of thin film composite (TFC) membranes with high water flux in the late 1970s using interfacial polymerization, a concept which allowed to form a thin polymeric layer onto a substrate (Lau et al. 2012, Yang et al. 2019). The first NF membranes were developed in the late 1980s mainly to combine the removal of organics with removal of hardness (Mohammad et al. 2015, Van der Bruggen et al. 2008). The most successful commercial membranes of the past and present in NF and RO are TFC membranes with an active layer of polyamide on a supporting layer of polysulfone (PSF) (Lau et al. 2012, Yang et al. 2019). These membranes are produced by interfacial polymerization of m-phenylenediamine (MPD) in water and trimesoyl chloride (TMC) in hydrocarbon (Lau et al. 2012). The active layer of a PA-TFC membrane is about 10 to 20 nm in thickness and the whole membrane including support and carrier has a total thickness of less than 200 µm (Yang et al. 2019).

The selectivity of NF membranes towards charged ions as well as the comparatively higher flux to RO drive application of NF and make it an inspiring field of research (Mohammad et al. 2015, Van der Bruggen et al. 2008). In contrast to larger particles, e.g. suspended solids, colloids etc., rejection of charged ions is accompanied by phenomena such as concentration polarization (CP) and the Donnan effect (Labban et al. 2017). Ions can move freely in water and diffuse along concentration gradients. During NF and RO filtration, this leads to the formation of a concentration boundary layer (CBL) over the membrane surface. The Donnan effect describes rejection characteristics due to electrostatic forces, which can lead to negative rejection, meaning that the concentration of a particular ion can be larger in the permeate than in the feed (Labban et al. 2017). In order to predict membrane performance, understanding the mass transfer on the feed side of the membrane is of crucial importance as it directly affects the mass transfer inside the membrane and on the permeate side. Due to the great variability of rejection of species, accurately predicting the mass transfer in NF is even more challenging compared to RO.

1.2 Mass Transport in Reverse Osmosis Processes

Reverse osmosis and nanofiltration seek to separate solute by forcing water to permeate through a semi-permeable membrane. The primary model to describe the permeation process through dense membranes is the solution-diffusion model (Wang et al. 2014, Wijmans and Baker 1995). It proposes that the permeation process is governed by the amount of material, which can dissolve in the membrane and the rate of diffusion, at which it can traverse the membrane (Wijmans and Baker 1995). The fundamental driving force for permeation is a difference in chemical potential (μ) across the membrane with the movement of material (flux) aiming to establish equilibrium. Thus, flux (J) of a component, i, is principally described by

$$J_i = -L_i \frac{d\mu_i}{dz} \tag{1}$$

with *L* being a coefficient of proportionality. Firstly, looking only at the mass transport inside the membrane, the solution-diffusion model only considers a gradient in concentration as driving force, which transposes Eq.1 into Fick's first law of diffusion with the diffusion coefficient, *D*, meaning that mass transport in the membrane is entirely diffusive.

$$J_i = -D_i \frac{dc_i}{dz} \tag{2}$$

Secondly, looking at the conditions across the membrane, concentration and pressure are considered. Pressure gradients are a difference in hydrostatic pressure (p) and a difference in osmotic pressure (π) on the feed and the permeate side of the membrane. The osmotic pressure of the feed solution needs to be overcome by the hydrostatic pressure in order to start the process of reverse osmosis. Under these conditions and with simplifications, Eq.1 for the water flux across the membrane transposes into

$$J = A(\Delta p - \Delta\pi) \tag{3}$$

with *A* being the water permeability constant. This equation assumes that the difference in hydrostatic pressure is much greater than the difference of osmotic pressure, which is the case in most practical RO applications. Similar considerations lead to the simplified expression for salt flux:

$$J_s = B(c_0 - c_d) \tag{4}$$

with *B* being the salt permeability constant and c_0 and c_d being the salt concentration on the membrane surface on the feed (z = 0) and permeate side (z = d) respectively.

Equations 3 and 4 show that water transport is increased mainly by increasing hydrostatic pressure, while salt transport is independent of pressure with the most important parameter being the salt concentration on the feed side membrane surface (c_0). The membrane surface concentration is not simply equal to the salt concentration of the feed solution but rather elevated due to an accumulation of rejected material. This is described by the phenomenon of concentration polarization (CP).

1.2.1 Concentration Polarization

Due to Eq.4 CP has a large influence on membrane separation performance. Additionally, raising the solute concentration has large implications in membrane fouling too. Membrane fouling is defined as an accumulation of deposits of various kinds on the membrane surface (or inside the membrane feed channel) causing a decline in filtration performance. Membrane fouling can be reversible, e.g. through cleaning methods or irreversible and, thus, shorten the lifetime of membrane elements in filtration facilities. Fouling is classified into four major classes, which are scaling, colloidal fouling, organic fouling and biofouling. All these types are fundamentally caused by an accumulation of material. For example, local oversaturation of salts due to CP can lead to crystallization and scaling, a deposition of sparingly soluble salts on the membrane surface (Antony et al. 2011, Shirazi et al. 2010). Hence, it has been a focus in membrane process modeling to predict CP for process design considerations and to better understand membrane surface fouling phenomena (Kim and Hoek 2005). Furthermore, fouling phenomena can be linked, which is why there is a growing interest to model combined fouling phenomena (Radu et al. 2015).

The main model for CP is the film theory (FT) model. FT considers three main mass flows of solute, a convective flow towards the membrane (J_S), a diffusive flow of back diffusion away from the membrane (J_D) and the mass flow through the membrane (J_P). At stationary conditions, a mass balance yields the relationship between the concentration at the membrane surface ($c_m = c_0$), the bulk concentration (c_b) and the permeate concentration (c_p):

$$\frac{c_m - c_p}{c_b - c_p} = exp\left(\frac{u_w \delta}{D}\right) \tag{5}$$

with D being the diffusion coefficient of the species, δ being the thickness of the concentration boundary layer and u_w being the velocity of the water flow through the membrane (permeation).

Assuming complete rejection of salt (c_p = 0), the relationship can be simplified to:

$$c_m = c_b exp\left(\frac{u_w \delta}{D}\right) \tag{6}$$

Hence, the concentration polarization gradient follows an exponential function dependent on diffusivity, permeate flux and feed concentration. The governing mass transport is schematically illustrated in Fig. 1.1.

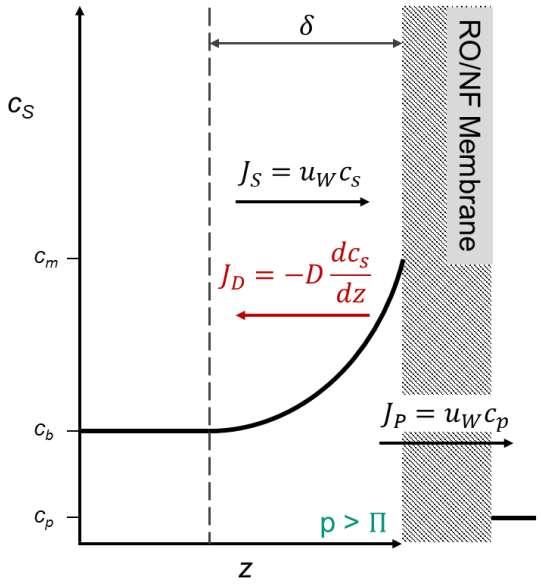

Fig. 1.1 Scheme of the film theory model of concentration polarization. J: solute flux (J_S: convective, J_D: diffusive, J_P: permeate), u_W: velocity, c_S: solute concentration (c_m: at membrane, c_b: in bulk, c_p: in permeate), D: solute diffusion coefficient, δ: concentration boundary layer thickness, π: osmotic pressure, p: hydrostatic pressure

The FT-model approach only considers the axial (z) dimension of the CP phenomenon. However, during cross-flow membrane operation the feed bulk solution is concentrated along the feed channel (x) as well, since permeate is being extracted. Hence, c_b is increasing along the feed channel and the transverse flow is affecting the CP layer (CPL). As a result, the CPL builds up along the feed channel and CP is more severe closer to the outlet of a membrane module and at later stages of a multi-stage NF/RO system. The CPL is stationary and stable given no change in the operational and physical parameters, stable hydrodynamic conditions (laminar flow) and assuming no chemical reactions or nucleation. Equilibrium between the two governing mass flows is achieved quickly.

However, in common practical applications, the local increase in concentration leads to super saturation of sparingly soluble salts, which precedes nucleation and causes the subsequent formation of a scaling layer on the membrane (Benecke et al. 2018, Radu et al. 2014). Thus, it is important to know the extent of CP, i.e. how much higher the concentration of a solute is at the membrane wall (c_m) compared to the bulk concentration (c_b, or feed concentration c_f). This is known as the concentration polarization factor (CPF) or the CP modulus ($c_m \cdot c_b^{-1}$). The CPF is dependent on many design parameters. Feed spacers increase the advective mass transport and therefore reduce the CPL. The length of the feed membrane channel impacts maximum solute concentration. Increased velocity reduces CP by improved mass transfer and decreased recovery. Transmembrane pressure (TMP) and membrane characteristics, e.g. permeability and rejection, influence the CPF also locally. As a result, the CPF is specific to a system, operating conditions and water type.

Thus, in practical cross-flow membrane applications, CP is a complex phenomenon. It is coupled with hydrodynamic conditions, which are influenced by CP and related fouling phenomena, which in turn influence CP. This makes modeling of CP computationally intensive and complex. The problem is further exacerbated by practical design choices aimed to minimize the CPF as well as other fouling phenomena affecting the filtration conditions locally and overall (Kim and Hoek 2005, Picioreanu et al. 2009, Radu et al. 2015). Among current research to reduce the CPF are novel type spacers, pulsating flow, air sparging and low frequency ultrasonic irradiation (Mohammad et al. 2015).

Yet, the theoretical approach has been a focus of CP research and has produced the most advances in describing and predicting the phenomenon. However, lately, the number of publications in the field of modelling NF processes has been in decline despite a generally increasing trend in all other aspects of NF research (Oatley-Radcliffe et al. 2017). It may be necessary for experimental studies to catch up, before further advances in modelling are possible. Experimental studies providing local solute concentration profiles in membrane channels are important to inform, validate and challenge theoretical considerations and results. However, such studies are scarce in literature. Only few experimental studies have been presented for quantification of the CPL (Chen et al. 2004, Chmiel and Fritz 2006, Fernández-Sempere et al. 2010, Sablani et al. 2001). Even fewer studies have tried to measure CP in cross-flow conditions and the author is not aware of a study presenting an experimental setup to quantify the CPL locally in membrane units with general feed channel dimensions and flow velocities present in common spiral wound modules (Chen et al. 2004, Fernández-Sempere et al. 2010, Sablani et al. 2001).

In a review on CP published in 2001, Sablani et al. mention NMR imaging to determine CPL thickness of an oil-water emulsion in cross-flow microfiltration and a laser-based refractometric technique to measure the CPL of a biopolymer solution in dead-end ultrafiltration (Sablani et al. 2001). Since then, Fernández-Sempere et al. used Digital Holographic Interferometry, a variation of common Holographic Interferometry, to measure the CPL of a sodium sulfate solution in cross-flow RO (Fernández-Sempere et al. 2010). The technique enables the study of concentration boundary layers by visualizing local changes in the refractive index of the sample solution.

This scarcity of available experimental techniques is a clear indication to the general difficulty associated with localized *in-situ* study of CP on a micro-scale. However, concentration gradients are present in many applications other than water desalination and measurement of those gradients has often been successful with various techniques. For example, Raman microspectroscopy (RM) has been successfully used to measure concentration gradients *in-situ* within fuel cell membranes (Scharfer et al. 2007). RM is a particular promising technique as it is well established, easy to operate, has great theoretical depth resolution and sensitivity, as well as low interference with water and some common water components (e.g. NaCl) (Murata et al. 1997). For the first time, this work explores RM for the *in-situ* measurement of the CPL in a NF system.

1.3 Thesis Scope and Outline

Concentration polarization (CP) is fundamental to nanofiltration (NF) and reverse osmosis (RO) systems and directly as well as indirectly responsible for filtration performance losses. The aim of this work is to better understand CP in these systems by direct measurement of the concentration polarization layer at various conditions.

This thesis is divided into four chapters, each with a specific focus on the measurement concept as well as the measurement conditions in order to present the technique conclusively. Starting with favorable operating conditions for proof-of-concept, more complex filtration conditions are introduced further into this work, which also relate closer to conditions in practical NF/RO systems. The quality of the obtained data and the applicability of the experimental methodology is critically discussed throughout.

Chapter 2 introduces Raman microspectroscopy generally and a specific methodology is presented, which provides proof-of-concept for the ability of the Raman technique to measure

concentration gradients near the membrane surface caused by CP. A method for interpretation of the raw data is presented, which permits the display of meaningful concentration profiles.

Chapter 3 applies the methodology established in the previous chapter to a variety of operating conditions to demonstrate applicability and robustness of the technique. The results show the differences in the concentration polarization layer (CPL) at varied cross-flow velocity, system pressure and recovery. Feed spacers are introduced and 3D maps of the concentration distribution within the membrane feed channel are presented. The influence of natural convection at low cross-flow velocity is demonstrated.

Chapter 4 introduces membrane fouling to assess the ability of the Raman technique as well as the experimental methodology to show the effect of biofouling on the CPL. The Raman technique is applied jointly with optical coherence tomography (OCT) to measure the CPL with biofouling layers of varying thickness. Fouling layers are developed through a specified enhanced biofouling regimen and the characteristics of the biofouling layer are presented and discussed with regards to the Raman technique. Concentration profiles of the CPL show the effect of biofilm enhanced osmotic pressure (BEOP) as a mechanism for filtration performance losses in membrane systems affected by biofouling.

Chapter 5 summarizes the conclusions of this work and shares an outlook on the applicability of the presented methodology and gives suggestions for further research. With Raman microspectroscopy a user friendly and readily available measurement technique can be added to the toolkit for investigation of CP in membrane feed channels. As such, it is an instrument, which provides non-invasive and direct measurement of the CP phenomenon within a variety of conditions.

2 Raman Microspectroscopy for *In-Situ* Measurement in a flat-sheet cross-flow Nanofiltration Membrane Unit

Raman Microspectroscopy

This work is based on the exploration of Raman microspectroscopy (RM) for the measurement of concentration gradients in aqueous solution. This chapter introduces RM and explains its peculiarities with respect to the main objective of depth profiling in aqueous solution. This is to highlight the mechanism of the technique, the theoretical opportunities it presents and the main pitfalls that are associated.

RM is part of the toolkit of vibrational spectroscopy. It is based on the Raman effect, which was experimentally discovered in 1928 in Calcutta by Raman and Krishnan (Raman and Krishnan 1928). Raman spectroscopy has since become an easy-to-use standard tool for material characterization of any kind, continuously finding new realms of application. Modern research fields include using RM for the characterization of water contaminants such as nitrites, nitrates, chlorates, perchlorates and others (Singh et al. 2019, Zapata and García-Ruiz 2018), contaminants in food (Yaseen et al. 2017), detection of microplastics (Anger et al. 2018, Araujo et al. 2018) as well as monitoring and characterization of membrane fouling, particularly biofouling (Ivleva et al. 2017, Lamsal et al. 2012, Pahlow et al. 2015, Virtanen et al. 2017, Wagner et al. 2009). For this work of particular relevance is also its use for measuring sulfate in natural brackish waters (Murata et al. 1997).

When a sample containing Raman active compounds is exposed to a monochromatic beam of light of a certain wavelength, a portion of the incoming light is deflected from its original direction of propagation (scattered). Most of the scattered light has the same wavelength as the illumination source (Rayleigh scattering/elastic scattering). However, a small portion of the scattered light is of discretely altered wavelength, i.e. light with a significant change in frequency. This shift in wavelength corresponds to a transition in the rotational or vibrational energy state of a molecular system (Keresztury 2002). This phenomenon is called the Raman effect (i.e. Raman scattering/inelastic scattering). Molecules, which exhibit this effect are considered Raman active. The Raman Effect can be used to identify and quantitatively analyze molecules in liquid phases such as water. Combining Raman spectroscopy with a confocal

Parts of this chapter have been published in: Jung, O., Saravia, F., Wagner, M., Heißler, S. and Horn, H. (2019) Quantifying Concentration Polarization – Raman Microspectroscopy for In-Situ Measurement in a Flat Sheet Cross-flow Nanofiltration Membrane Unit. Scientific Reports 9(1), 15885.
Work was set up with contributions from all authors. Data collection, processing and analysis was done by Oliver Jung. Main manuscript text was written by Oliver Jung and reviewed by all authors.

microscope allows for 2D and 3D quantitative analysis of the distribution of Raman active molecular systems in transparent solutions.

RM has a few important characteristics to be aware of (Dhamelincourt 2002, Fredericks 2002, Griffiths 2002, Hendra 2002). First, Raman spectroscopy mostly uses a monochromatic light source in (or close to) the visible spectrum of light. As the spectral transmittance of water is high in the visible range, Raman is well suited for measurements in a water phase. Second, the Raman Effect is a very weak effect with only a very small portion of the incoming light being Raman scattered. This means that a powerful illumination source is required. But, perhaps more importantly, it also means that Raman techniques are generally vulnerable to being masked by brighter light of other sources, i.e. fluorescence or stray light in the system. Third, according to Beer's law, absorbance is proportional to the concentration of the absorbent. Raman spectroscopy, however, relies on light scattering where such proportionality is not the case. The implication is that spectral intensities also depend on the instrument used to measure. Calibrations cannot readily be transferred to another instrument and have to be done with each instrument independently or adjusted (Hendra 2002).

The main drawback of RM is fluorescence, which can mask the weak Raman signal. One option to combat fluorescence is to switch the excitation wavelength to the UV or Near-Infrared (NIR) region where fluorescence is reduced (Fredericks 2002, Griffiths 2002). However, outside the visible range, absorption in water increases sharply, resulting in a weaker signal and the risk of substantial heat transfer into the sample. Also, the Raman intensity scales with the wavenumber of the excitation source to the 4^{th} order (Griffiths 2002). Thus, in NIR, at longer wavelengths, the Raman intensity is much lower than in the visible spectrum. Consequently, the Raman intensity in the UV range is higher due to the shorter wavelengths. Another option to reduce fluorescence is to try to quench it by prolonged irradiation, also referred to as "burning out" (Fredericks 2002). This technique is particularly suitable for RM due to the high energy input into the sample.

Advantages of RM include a high spectral resolution. Typically, the spectral resolution is in the range of 1 – 10 cm^{-1}, which allows for safe distinction of Raman active compounds (Dhamelincourt 2002). Additionally, spatial resolution is high due to RM using an optical microscope. Thus, RM is subject to the Abbe diffraction limit, which states that the minimum resolvable distance (d) of two point sources in air is:

$$\mathrm{d} = \frac{\lambda}{2\mathrm{NA}} \tag{7}$$

Here, λ is the wavelength of the illuminating light and NA stands for numerical aperture, which is a property of the objective lens used in the system. Thus, for RM, spatial resolution is about ≤1 µm^2 in air (Dhamelincourt 2002, Fredericks 2002).

More important for depth profiling is the question of the resolution along the optical axis (depth resolution). According to Juang et al. the minimum depth resolution can be estimated to be as follows (Fredericks 2002):

$$\Delta z \geq \pm \frac{4.4 n \lambda}{2\pi (\mathrm{NA})^2} \tag{8}$$

Thus, the depth resolution depends on the refraction index of the immersion medium *n*, the wavelength of the illuminating light λ and the numerical aperture (NA) of the objective lens. For the RM setup used in this work (water: n = 1.33, lens: NA = 0.7, laser: λ = 532 nm), the minimal depth resolution would be as small as 2 µm. However, as Everall has pointed out, the depth resolution can be substantially worse when the optical beam is refracted due to the occurrence of spherical aberration (Everall 2000, 2010). Figure 2.1 demonstrates what happens to the optical pathway when there is an interface at which the refraction index increases, e.g. air to water. Due to refraction, the focus point is shifted below the nominal focal plane, which would otherwise be determined by the focal length, *f*, of the objective. In depth profiling this causes a foreshortened representation of the actual depth profile and an underestimation of the thickness of the sampled volume. Additionally, the spherical aberration also causes an increasing depth of field, *DOF*, the deeper the focus into the sample. This means that depth resolution degrades when focusing deep into the sample. The use of a confocal aperture can restore some of the lost depth resolution although accompanied by major loss of signal intensity since signal originating from outside the focal plane is clipped at the confocal aperture (Everall 2009). Finally, laser intensity too is decreasing with depth as spherical aberration causes a broadening of the illumination volume. In total, spherical aberration alters the expected depth profile substantially, which has important consequences to the interpretation of the acquired depth profile data as well as to the experimental methodology and setup required.

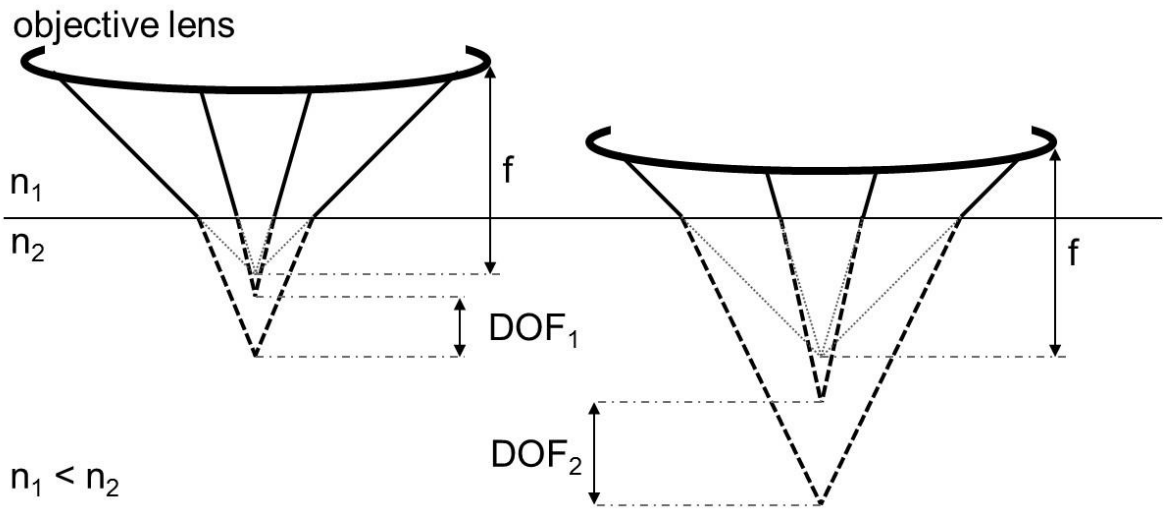

Fig. 2.1 Schematic illustration of the illumination pathway when focusing into a sample with refractive index n_2. Refraction causes a wider depth of field (DOF) and the point of focus is shifted below the nominal focal plane determined by the focal length (f) of the objective. Dotted lines show the path of light for $n_2 = n_1$ *(no refraction)*. Dashed lines show the path of light in the sample with $n_2 > n_1$. n: refractive index

Note: The setup used in this work actually exhibits two inter-faces with changes in refractive index, i.e. air to flow cell window and flow cell window to aqueous solution. Since an objective lens with an adjustable cover glass correction of 1.3 mm is used and for simplicity reasons, the windows' influence on the light path is disregarded throughout this work when discussing spherical aberration.

2.1 Materials & Methods

2.1.1 Experimental Setup

A membrane flow cell has been designed specifically for this work to allow for the simulation of practical conditions in common spiral wound modules in combination with usability for RM (Fig. 2.2). The flow cell is a flat sheet cross-flow membrane unit with a channel length of 11.2 cm and channel width of 3 cm for a total membrane area of 33.6 cm². Thickness of the feed channel is about 700 µm. The flow cell features two sapphire windows of 1.3 mm in thickness to permit 3D Raman sampling while maintaining cell integrity at higher pressures. The cell has been operated successfully at pressures up to 12 bar with the featured window thickness of 1.3 mm. A preliminary test with a sapphire window of smaller size and a thickness of 1 mm

has shown structural integrity at 40 bar, demonstrating the principal applicability of this cell design for the simulation of common RO and NF applications. Window thickness is a critically important parameter as it increases the required working distance of the objective as well as spherical aberration, which both negatively affect depth resolution. The cell windows cover two areas accessible for analysis. One area in the beginning of the flow channel, 1.5 to 3.5 cm from the inlet and another area 7 to 9 cm from the inlet.

The membrane filtration system is a total recirculation system set up to keep all parameters constant. A scheme of the principal setup is shown in Fig. 2.3. Note that the configuration of the microscope is inverted, which means that the membrane is located on top of the feed channel. The sample volume is a 2 L container, which is continuously stirred and temperature regulated. The feed solution is pumped through a 0.22 µm particle filter, which is followed by a high pressure pump. A recirculation bypass including a metering valve is used to regulate feed flow. Permeate is re-joined with the brine behind the pressure valve and then routed back into the feed container. This is done jointly with the recirculation flow. Permeate can also be routed across a balance to determine permeate flux and permeate conductivity. This was not done during Raman measurement operation but rather before and after the start of a measurement series. Measurement parameters were recorded using NI LabVIEW™. Recorded parameters were temperature, feed and permeate conductivity, brine and permeate flow as well as inlet and outlet pressure.

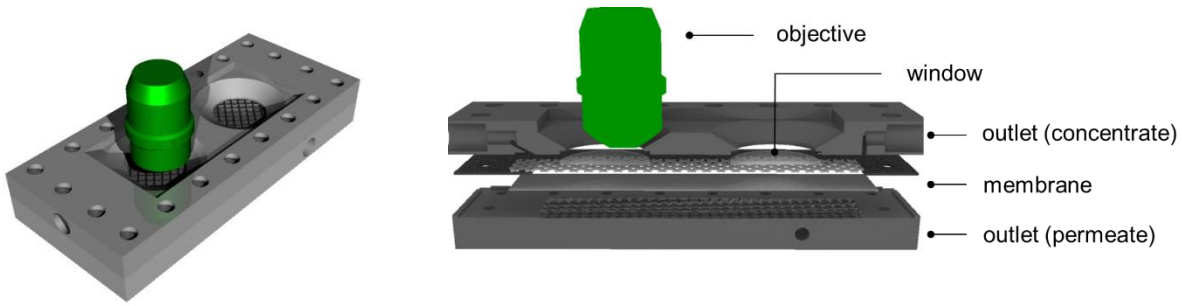

Fig. 2.2 High pressure flat sheet cross-flow membrane cell for use with RM. Active membrane area 33.6 cm^2.

The feed solution is a magnesium sulfate solution of varying concentrations from 7 $g \cdot L^{-1}$ (0.07 $mol \cdot kg^{-1}$) up to 33.5 $g \cdot L^{-1}$ sulfate (0.35 $mol \cdot kg^{-1}$). The solution was prepared with $MgSO_4 \cdot 7H_2O$ from Roth (99.7 % purity) and deionized water. Sulfate is a common component of scaling in the form of gypsum. The solubility of magnesium sulfate is 300 $g \cdot L^{-1}$, thus precluding the

occurrence of scaling in these experiments. Without membrane fouling and with all parameters constant, the CPL is stable after reaching equilibrium conditions and the measurement is not time sensitive. Measurements of the CPL were done with a solution of 10 g·L^{-1} sulfate (0.104 mol·kg^{-1}) at multiple cross-flow velocities and with constant operating pressure of 10 bar.

The Raman system used was an inverted Raman microscope SENTERRA I from Bruker. Recording software was OPUS 7. A 532 nm laser (Cobolt Lasers, Solna, Sweden) with a power of 50 mW was used for all measurements. The objective, Olympus LUCPLFLN 60x, has a NA of 0.7, working distance of 1.5 mm beyond the cover glass, correction collar for a cover glass thickness of up to 1.3 mm and a magnification factor of 60x. The membrane cell was mounted onto the sampling stage of the Raman microscope with windows facing down.

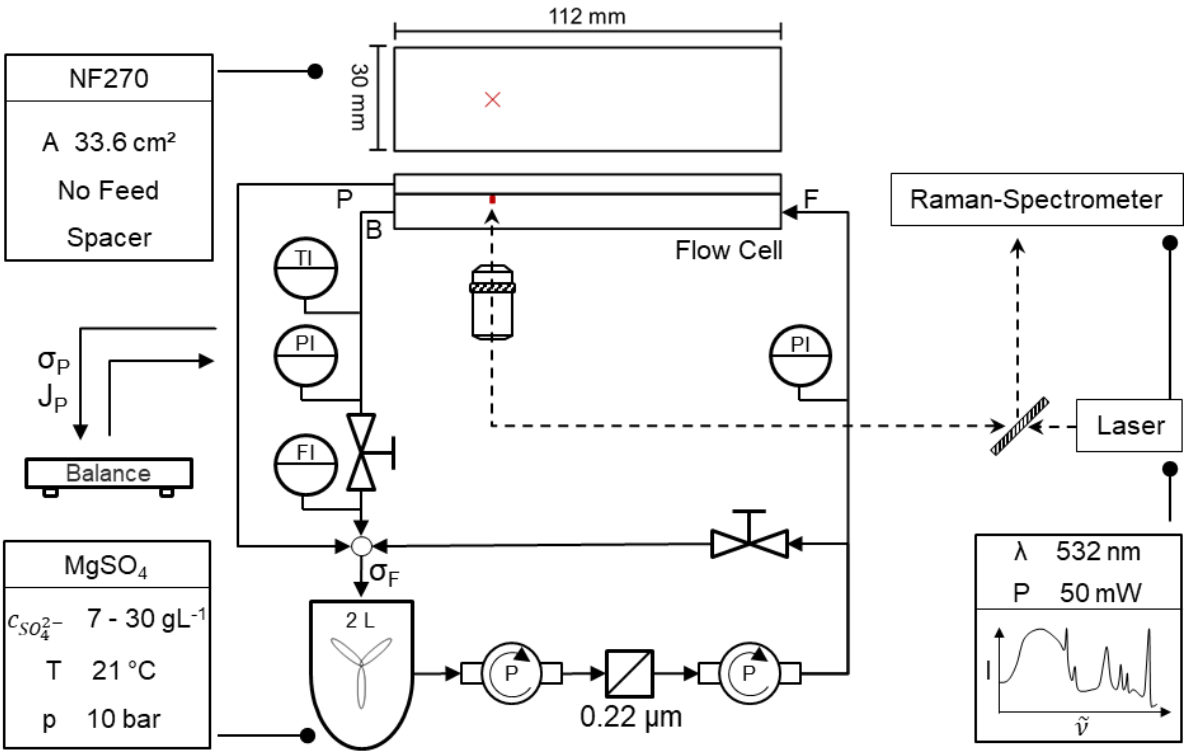

Fig. 2.3 Scheme of the experimental setup combining nanofiltration in recirculation mode and Raman microspectroscopy. The microscope is of inverted configuration. The membrane is positioned on top of the feed channel. Flow, pressure, conductivity, flux and temperature are recorded and kept constant during measurements. The feed solution is a pure magnesium sulfate solution, which is well below saturation. No scaling occurs. The permeate flux is measured by weighing. Red marking shows point of measurement. F: Feed, B: Brine, P: Permeate, σ: electrical conductivity, J: Flux

The Raman system was used to measure the Raman response of sulfate in solution. Sulfate has nine modes of internal vibration that are Raman active of which the linear symmetrical stretching vibrational mode (ν_1) is the strongest. It shows a Raman band with a peak at 981 cm^{-1}. The intensity of the Raman band (integral area 994 – 966 cm^{-1}) is proportional to the concentration of sulfate molecules in the focus point.

All filtration experiments were done with a DOW FILMTEC™ NF270 nanofiltration membrane. The NF270 has a nominal rejection of magnesium sulfate of >97 % and a permeability of 11.1 $L \cdot m^{-2} \cdot h^{-1} \cdot bar^{-1}$ according to the manufacturers specifications. Clean water flux in the filtration cell at 10 bar pressure was 7.36 $mL \cdot min^{-1}$ (Permeability 13.1 $L \cdot m^{-2} \cdot h^{-1} \cdot bar^{-1}$). Rejection of magnesium sulfate solution of 10 $g \cdot L^{-1}$ sulfate was 97.6% in terms of conductivity. The NF270 was chosen for these experiments for its high permeability, high rejection for sulfate, lack of interfering Raman bands in the range of 994 – 966 cm^{-1} (sulfate band area ν_1), lack of fluorescence and widespread commercial use. The NF270 is a polyamide thin-film composite membrane with a supporting layer made of PES, which shows three distinct Raman bands in the range of 1165 – 1060 cm^{-1}. A raw spectrum showing the Raman bands of the membrane and the Raman band ν_1 of sulfate is shown in Fig. 2.4. The intensity of these Raman bands is later referred to as the “membrane signal” and the “sulfate signal” respectively.

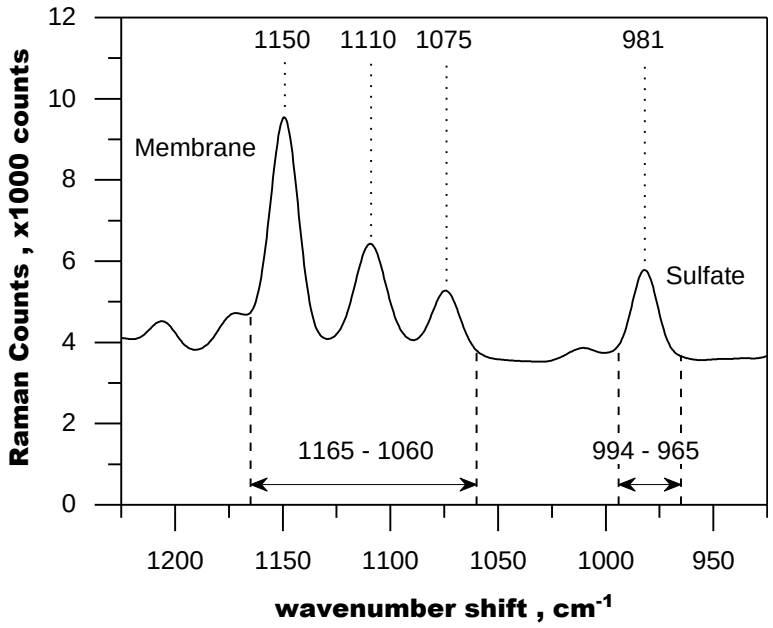

Fig. 2.4. Raw Raman spectrum showing the specific Raman bands for the membrane and the Raman band of sulfate, which were used for analysis. Raman intensity is obtained by integrating from 1165 to 1060 cm^{-1} for the membrane (membrane signal) and from 994 to 965 cm^{-1} for sulfate (sulfate signal).

2.1.2 **Experimental Methodology**

All relevant parameters were kept constant during the recording of the CPL profiles. Consecutive measurements assure steady state was achieved. Feed concentration was set measuring the electrical conductivity at 25 °C with a conductivity of 9.55 $mS \cdot cm^{-1}$ corresponding to a concentration of 10 $g \cdot L^{-1}$ sulfate. Feed pressure was held constant at 10 bar and feed temperature at 21 °C. Depth profiles were recorded for velocities of 0.04 $m \cdot s^{-1}$ and 0.2 $m \cdot s^{-1}$.

The raw data depicts the Raman intensity over *z* (distance from the membrane) and requires a conversion to display the CP profile. For the conversion a calibration was set up to correlate the Raman intensity to the sulfate concentration. Calibration was done with a velocity of 0.2 $m \cdot s^{-1}$, which is a usual value for the operation of commercial spiral wound modules. Feed pressure was about 0.15 bar, which was the minimum pressure required to set the desired velocity. Depth profiles of seven concentrations, 7, 10, 15, 20, 25, 30 and 33.5 $g \cdot L^{-1}$ sulfate, were recorded for one calibration data set. In total four data sets were recorded and averaged. A linear fit across all concentrations for each point of depth was used to give the correlation of sulfate concentration to Raman intensity dependent on the position of the focal plane in relation to the membrane. The calibration data set is included in Appendix Fig.A1. The linear fitting functions for each depth point are listed in Appendix Table A1.

The calibration requirements were set following theoretical considerations about the osmotic pressure of the feed solution. The pressure difference across the membrane is the driving force for reverse osmosis driven membrane processes. However, the effective transmembrane pressure (TMP) differs from operating pressure due to the osmotic pressure (Π) of the feed solution. Flux is induced only when effective TMP exceeds the osmotic pressure of the feed solution. Therefore, system pressure has to be higher than the osmotic pressure of the feed water. Since in the CPL osmotic pressure increases locally towards the membrane wall, CP reduces effective TMP. Consequently, the extent of CP is also limited by the applied operating pressure since effective TMP must be greater zero to allow CP formation in the first place. The osmotic pressure can be estimated using the Van't Hoff equation

$$\Pi = i\phi \mathrm{mRT} \tag{9}$$

with i being the number of dissociation of the salt, m being molality, R being the gas constant, T being the temperature in K and ϕ being the osmotic coefficient (i.e. NaCl: ϕ = 0.925 at 0.2 $mol \cdot kg^{-1}$ (Robinson and Stokes 1949); $MgSO_4$: ϕ = 0.556 at 0.2 $mol \cdot kg^{-1}$) (Guendouzi et al. 2003)).

The relationship between sulfate concentration and osmotic pressure of a pure magnesium sulfate solution in the present range of concentration is thus given by

$$\Pi = 0.091 \cdot m \cdot T \quad (10)$$

with Π in bar, molality in mol·kg^{-1}, temperature in K. For the CPL measurement conditions (0.104 mol·kg^{-1}) the effective TMP at 20 °C, thus, is 7.2 bar initially, before the formation of the CPL. With CPL formation the effective TMP reduces. Osmotic pressure of the feed solution is equal to the applied pressure of 10 bar at a concentration of about 35.5 g·L^{-1} (0.37 mol·kg^{-1}). This value provides an upper reference for the calibration requirements.

Depth profiles were recorded with a step width of 10 µm and a range of 250 µm. The recorded spectra yield the sulfate signal and the membrane signal simultaneously. The point at which the membrane signal reaches maximum value was set to z = 0 µm (set location of the membrane surface). Presented are the measurement values in the range -20 to 170 µm. The measurement parameters for the Raman system were the same for all recordings presented. The total exposure time was split in consecutive five second intervals of exposure (integration time t_i) per measurement position. The software gives a joint output (co-edition) of one spectrum after the total exposure time of 30 seconds (integration time t_i = 5 s, co-edition = 6). Thus, the total measurement time of a depth scan with 25 points is about 14 minutes (including initializing of the Raman spectrograph and background recording). The nominal laser intensity was set to 50 mW power. A background was measured before each measurement. The confocal aperture was set to a 50×1000 µm slit. Although a smaller pinhole aperture (25 µm) was available and would suggest improvements in depth resolution, it was decided against in order to compromise with measurement time. The bigger slit aperture causes much less intensity loss, which allowed for a 20 times shorter integration time without substantially reducing depth resolution. This is further discussed in section 2.2.1.

2.2 Results and Discussion

Measuring CP with RM is not a straight forward technique. After data collection, the Raman intensity needs to be converted into concentration. Due to complex optical effects, which need to be accounted for, the chosen method for data conversion has a large influence on the final shape and quantification of the CPL. The better the conversion method corrects for the optical distortions, the more accurate the plot of the CPL will be. Thus, three steps are necessary to yield accurate results. Firstly, the relationship of Raman intensity with concentration needs to

be established. Secondly, the influence of optical distortions on the Raman intensity distribution through the feed channel (depth profile) needs to be discussed and thirdly, the effect of the optical distortions on the chosen conversion method and on the final CPL profile has to be examined.

2.2.1 Raman Intensity Distribution vs. Sulfate Concentration

Raman spectroscopy provides a spectrum of Raman intensity counts over wavenumber shift. The integral of the Raman band at 981 cm^{-1} (integral area 994 – 965 cm^{-1}) emanating from sulfate is proportional to the sulfate concentration. This is shown in Fig. 2.5 for three positions z = -20, 80 and 170 µm (membrane surface at z = 0 µm, positive values refer to a position inside the feed channel away from the membrane). Similar correlations were done for each point of the depth scale, which are included in appendix Table A1. Indeed, the correlation has to be established for each point of the depth profile individually, since the signal is losing in intensity and the slope is decreasing when focusing deeper into the sample. This is caused by the present refraction interface as shown in Fig. 2.1. To discuss this further, we have to look at how the output data is affected by the spherical aberration.

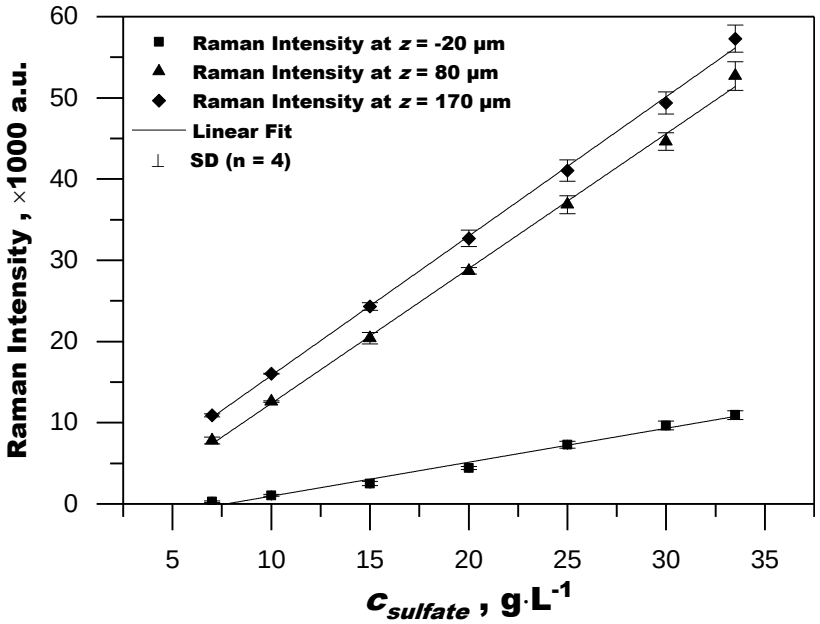

Fig. 2.5 Calibration results. A full calibration (7 – 33.5 $g \cdot L^{-1}$) was performed for every point along the depth profile from z = - 20 µm to z = 170 µm with Δz = 10 µm (z = 0 µm being the position of the membrane surface). For illustration purpose only calibration curves for depth

points z = -20, 80 and 170 µm are presented. Complete calibration results are summarized in Appendix Table A1. SD: standard deviation. $R^2 > 0.978$ for all curves.

The influence of the optical effects on the Raman intensity distribution through the feed channel can be illustrated by plotting the raw data of a depth profile through the whole feed channel with an unpressurized magnesium sulfate solution as shown in Fig. 2.6. Although the sulfate concentration is constant throughout the feed channel, the Raman intensity is continuously decreasing towards the membrane. The Raman intensity distribution can be explained by (1) decreasing laser intensity (i.e. power density: $mW \cdot mm^{-2}$) with deeper penetration into the sample (Everall 2009). The laser intensity decrease is linear and correlates well with the linear decrease of Raman intensity through most of the feed channel. The clipping of the Raman intensity near the borders of the feed channel is caused by (2) overlap of the focal volume (effective illumination volume) with the feed solution and the membrane respectively the cover. The cover (sapphire) and the membrane do not contain relevant concentrations of sulfate and thus do not contribute to signal intensity. The overlap is starting where the signal decrease deviates from linearity. For these reasons, the linear correlation between Raman intensity and sulfate concentration is dependent on the penetration depth. It should also be noted that the feed channel thickness is not represented accurately in Fig. 2.6. This is due to spherical aberration, which causes a foreshortened representation of the feed channel depth as demonstrated in Fig. 2.1.

The clipping of the Raman intensity of sulfate due to the cover is not a sharp cut-off. This is because the focal volume (i.e. DOF) is not a sharp point of focus but rather an intensity distribution. The laser beam is focused through the objective into the sample onto the focal plane. Due to the wave characteristics of light, constructive and destructive interference lead to a pattern with its highest intensity at the focal plane and areas with diminishing intensity to either side of the focal plane. Thus, excitation of Raman active species is not limited to the focal plane but has diminishing contributions from above and underneath the focal plane. The same happens in return, where the scattered light originating at the focal point creates a similar interference pattern at the spectrograph. This particular interference pattern is called a point spread function (PSF).

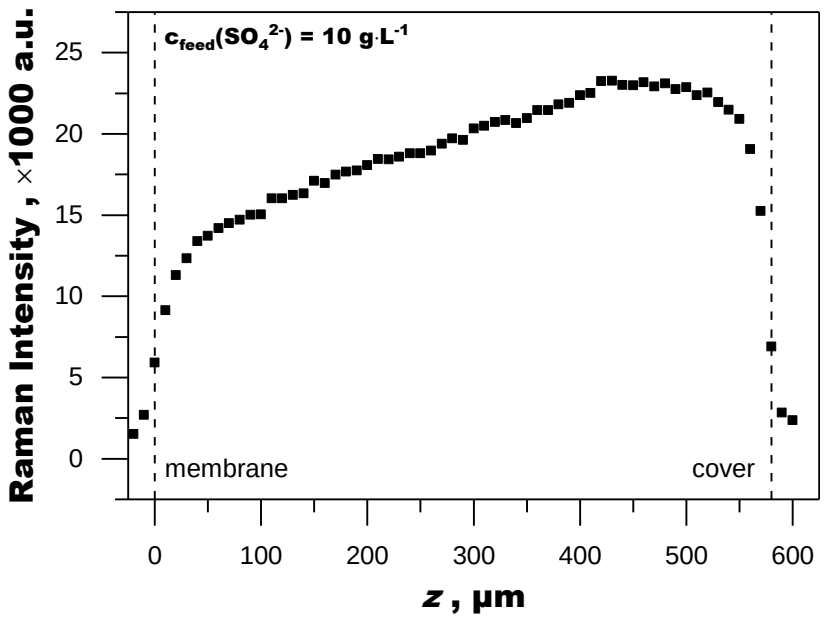

Fig. 2.6 Depth profile through the feed channel of a homogenous magnesium sulfate solution of $c(SO_4^{2-})$ = 10 g·L^{-1}. Plotted is the raw data of the sulfate band area (994 – 965 cm^{-1}). The inhomogeneous intensity distribution is caused by spherical aberration due to refraction. This also causes foreshortening of the profile and thus an inaccurate representation of the thickness of the feed channel which is about 700 µm.

It is helpful to consider the Raman data from the membrane to understand the extent of blurring present with this particular setup. Fig. 2.7 shows the plot of the Raman intensity of the membrane bands (1165 – 1060 cm^{-1}) over *z*. The almost symmetrical shape of the plot is a reasonable representation of the PSF of the present setup. All of the membrane signal originates from a plane at *z* = 0 µm, which is the location of the membrane surface. However, the signal is present (with decreasing intensity) even when focusing away from the membrane surface. The PSF characterizes this distribution.

A PSF is commonly categorized by the full width at half maximum (FWHM), which is the width of the function at half the maximum intensity. The FWHM is a representation of the depth resolution. In an ideal setup, the PSF would be sharp and symmetrical with a maximum depth resolution of 2 µm for the present setup in a dry case scenario (Eq.1). However, due to the refraction in the water phase, the actual PSF is wider, asymmetrical and broadens further the deeper the focus plane. From the plot of the membrane signal in Fig. 2.7 the FWHM of the present setup can be estimated to be about 75 to 82 µm, with the lower value obtained by reading the full width from the graph and the higher value by taking only the positive value and multiplying it by 2 (assuming the graph to be symmetrical). This shows the extent of the influence of spherical aberration due to refraction at the water interface. Any means to mitigate

or account for this effect will substantially improve the measurement technique in terms of depth resolution. The confocal aperture also influences the width of the PSF. A smaller pinhole increases depth resolution by clipping light, which originates from outside the focal plane. However, measurements with the 25 µm pinhole aperture yield a depth resolution of about 65 µm. This is an improvement of roughly 10 to 15% but the loss in intensity is substantial. As a result, measuring time increases about 20-fold to make up for the low intensity, while the depth resolution remains relatively poor. Improvements in depth resolution of 50% or better would be desirable.

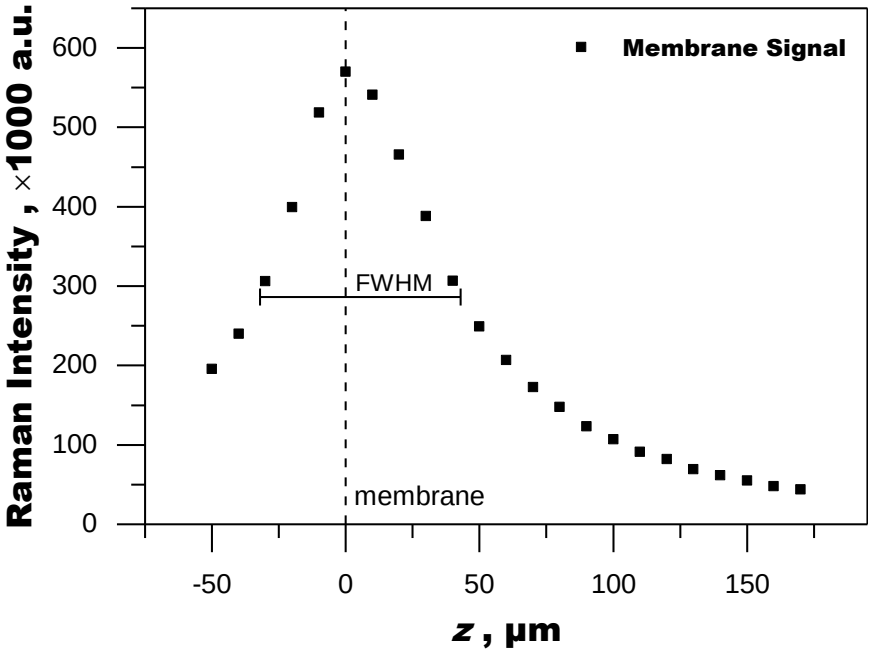

Fig. 2.7 Raman intensity distribution of the membrane bands at 1165 – 1060 cm^{-1} over z (optical axis). The plot represents the PSF (point spread function) with FWHM = 75 µm (full width at half maximum). The maximum intensity is used as the reference for the position of the membrane surface.

A broad PSF means that there is a lot of contribution to the Raman signal intensity from outside the focal plane. This is important to consider when interpreting measurement data. However, the raw signal profiles (Fig. 2.6 - Fig. 2.8) also demonstrate that the Raman measurement is sensitive enough to sufficiently resolve changes in Raman intensity with a resolution smaller than 5 µm. It is thus fair to assume that concentration changes can be recorded similarly and with similar resolution if one accounts for the effect of diminishing Raman intensity with depth.

2.2.2 Concentration Polarization & Calibration as Method for Conversion

The capability of RM to show the CPL is demonstrated well by plotting the raw data of the Raman intensity of the sulfate band of pressurized operation (induced CP) versus the raw data of unpressurized operation (no CP), which is shown in Fig. 2.8. The two depth profiles are clearly distinct and sufficiently resolved. Both depth profiles have been recorded with the same velocity and the same feed solution. The depth profile of the unpressurized system is constantly decreasing as explained in the previous section. The depth profile of pressurized operation shows an increase in Raman intensity with a maximum closer to the membrane. This increase in Raman intensity can only be caused by an increase in sulfate concentration. The shape is the result of superposition of (1) Raman intensity increase due to increased sulfate concentration towards the membrane and (2) diminishing Raman intensity due to overlap of the PSF with the membrane and diminishing laser intensity with depth, which is independent of the mode of operation. Thus, Fig. 2.8 provides proof of concept of RM to measure the CPL in nanofiltration. The CPL is represented in Fig. 2.8 by the area between the two curves. This raw data now needs to be translated into concentration values.

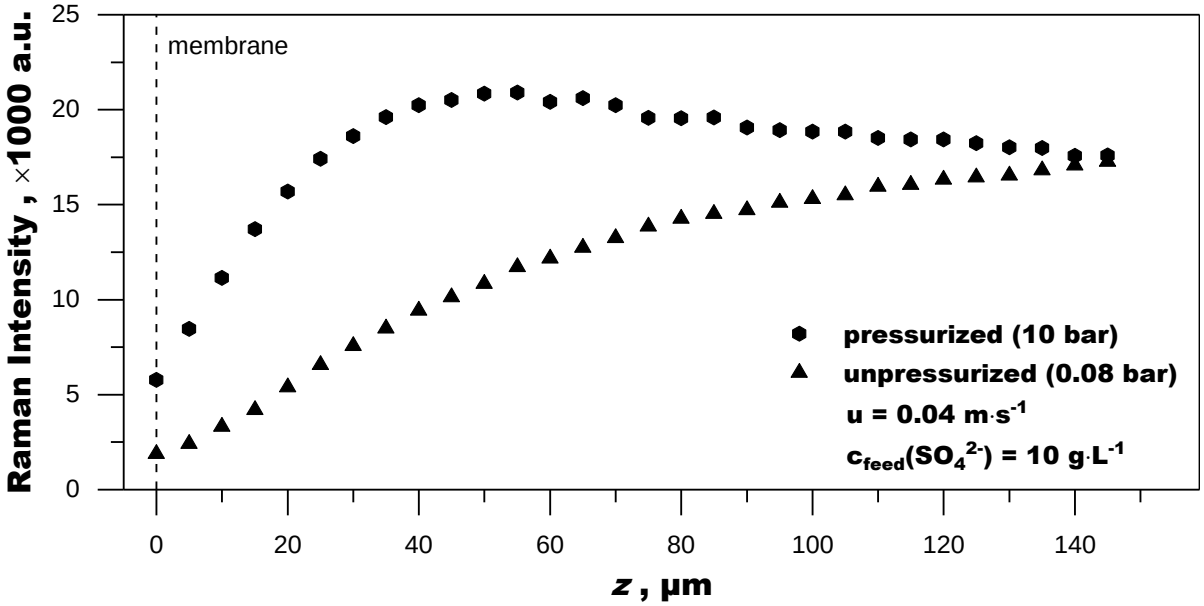

Fig. 2.8. Raman intensity distribution of sulfate (981 cm^{-1}) in the feed channel near the membrane (z = 0 µm) with (pressurized) and without (unpressurized) the presence of concentration polarization (CP). Data acquired at a mean velocity u = 0.04 $m \cdot s^{-1}$. Sulfate concentration in the fully mixed feed was 10 $g \cdot L^{-1}$.

In order to extract a sulfate concentration profile from the Raman intensity data, data processing needs to account for the optical distortions and the blurriness of the focus point. One option to do this conversion is by calibration. The necessary assumption is that the optical effects of spherical aberration are identical with and without the occurrence of CP. This assumption is justified, when the optical pathway remains the same in both cases, which means that there are no changes in the refractive index. Indeed, the change in refractive index expected from the highest concentration in the CPL to the feed concentration is only about 0.15 % total (CRC Handbook of Chemistry and Physics: "Concentrative Properties Of Aqueous Solutions: Density, Refractive Index, Freezing Point Depression, And Viscosity" 2005).

If the influence of changes in refractive index are neglected, then the shape of the PSF are also identical in both modes of operation. This means that the overlay of the PSF with the membrane is the same for both modes with reference to the membrane position, which in turn is fixed to the position of the maximum of the Raman membrane signal. This methodology automatically accounts for the compression of the membrane, which occurs in pressurized operation. For the present setup, compression of the NF270 membrane at 10 bar operational pressure is only about 5 to 10 µm. In pressurized operation, the focus point is shifted deeper into the sample by that amount. This effect can be influential when compression is more severe.

Assuming the PSF identical regardless of sulfate concentration, a practical calibration is possible, which corrects for the loss of Raman intensity due to spherical aberration. However, the calibration has to be done for each individual point of the depth scale, i.e. the calibration data set must be recorded as a depth profile as well. Multiple profiles at varying sulfate concentration in fully mixed conditions then permit to relate the Raman intensity measured during the CPL measurement to sulfate concentration. Fully mixed conditions can be assumed when no flux occurs during cross-flow operation (unpressurized operation). Examples for the linear correlation of Raman intensity to sulfate concentration for three points of the depth scale were shown in Fig. 2.5.

The conversion of the Raman intensity profiles of pressurized operation result in the CP profiles depicted in Fig. 2.9. The CP depths profiles show a gradual increase in concentration with an exponential shape, as would be expected from theory, until z = 20 µm. Closer 20 µm, the data points show a decrease in concentration. This is a result of the methodology and experimental setup. As previously demonstrated with the evaluation of the membrane signal in Fig. 2.7, the focus point is substantially blurred and there is overlap with the opaque membrane. For comprehensive understanding the following issues have to be considered when interpreting the profiles. These issues are all related to the depth resolution. (1) The onset of the CPL (i.e.

CPL thickness), (2) the membrane wall concentration, c_m, which is also c_{max}, and (3) the plausibility of the concentration values. First, the value of CPL thickness can be taken from the graph only with the width of the PSF in mind. Assuming the direction of measurement being towards the membrane, a raise in concentration will be observed before the focal plane matches the actual onset of the CPL. Fig. 2.10 position 1 shows a graphical explanation. This shift depends on the width of the PSF. Hence, FWHM/2 can be used as a correction as shown in Fig. 2.9B. For the setup used to record this data, the FWHM is about 75 µm. Hence, the boundary layer thickness is about 37.5 µm less than the point of first deviation from the baseline.

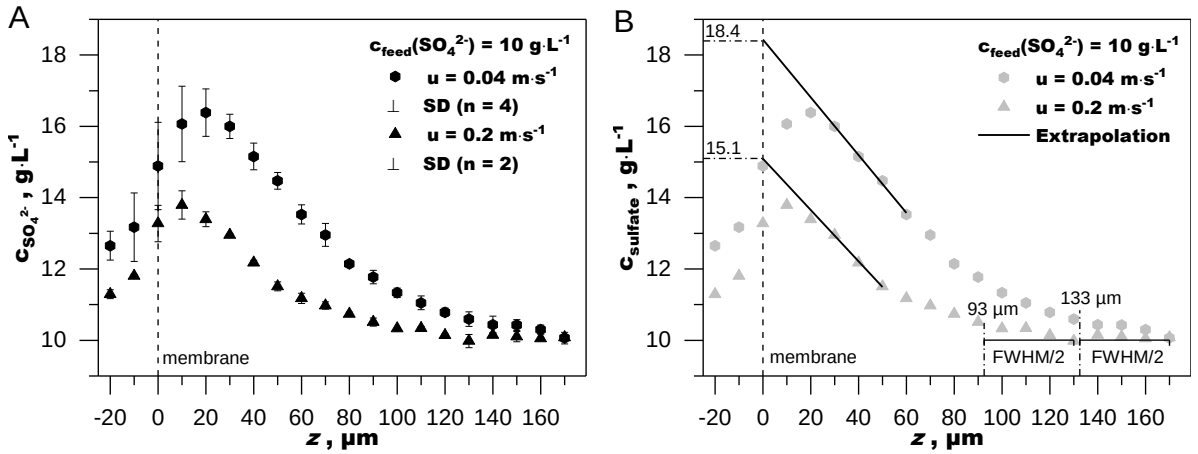

Fig. 2.9 A: CP profiles for a magnesium sulfate solution of 10 g·L^{-1} sulfate at p = 10 bar and velocities u = 0.04 m·s^{-1} and u = 0.2 m·s^{-1}. SD: standard deviation B: Linear extrapolation to the membrane surface to roughly estimate membrane wall concentration and true thickness of CPL after correction with FWHM/2.

The shape of the CPL profile close to the membrane (z < 30 µm) can be explained with similar considerations. As shown in Fig. 2.10 position 3, the contribution to the signal from outside the focus plane originates mainly from an area with lower concentration than present at the focal plane. Whereas in the case of calibration, the concentration at the focal plane is the same as the concentration across the total width of the PSF. This results in the data points close to the membrane being undervalued. In fact, all data points closer than FWHM/2 to the membrane can be assumed to be undervalued. The increasing uncertainty (standard deviation) towards the membrane further demonstrates the challenges with measurement close to the membrane wall. The examination shows that, using this methodology, accurate data is obtained when signal contribution from outside the focus plane matches the signal intensity, which is obtained at the same depth in calibration. In other words, if the added Raman intensity contribution from underneath the focal plane (area I in Fig. 2.10) equals the lesser Raman intensity contribution

from above the focal plane (area II in Fig. 2.10), then the measured value for CP equals the measured calibration value at that specific point of the depth scale. This can be seen in principle in Fig. 2.10 at position P2. It is reasonable to assume such symmetry in the middle (near linear) section of the profile. Hence, the middle section of the profile should yield the most accurate results.

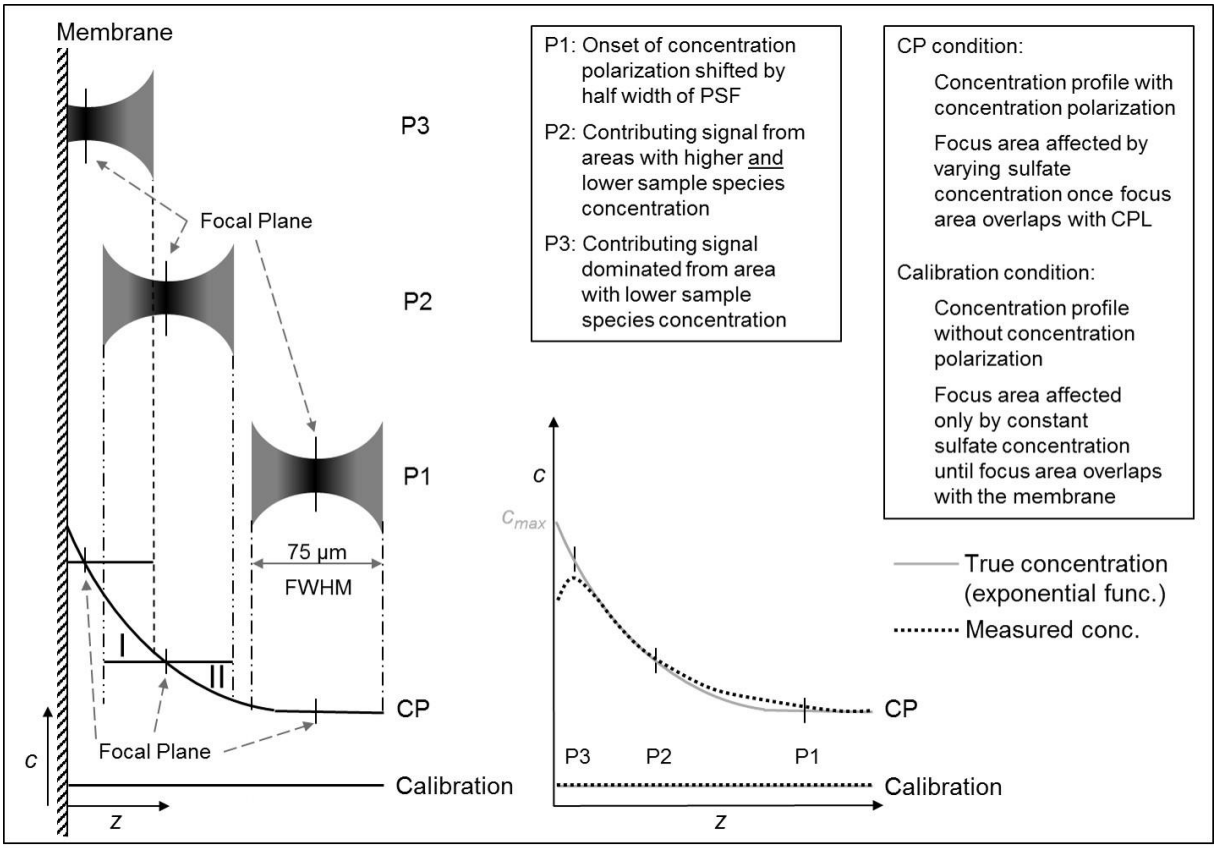

Fig. 2.10 Influence of the PSF on the shape of the sulfate concentration depth profiles shown in Fig. 2.9.

The membrane wall concentration thus cannot, unfortunately, be conveniently extracted from the Raman intensity data using this experimental methodology. A much sharper PSF than achievable with the present setup or a model correcting for the wider PSF in other ways would be required for this task. However, since the mid-section of the CPL is represented accurately, a reasonable estimate of the membrane wall concentration can be achieved by linear extrapolation from the mid-section to z = 0 µm. The membrane wall concentration (c_m) and the CPF ($c_m \cdot c_b^{-1}$; c_b: bulk concentration = feed concentration) derived from it, are important parameters for flux, rejection and scaling considerations. Therefore, the estimate from linear extrapolation provides an important quantification from an *in-situ* measurement method. The membrane wall concentration could also be extrapolated by fitting an exponential function to

the measured profile. This would make sense since the CPL is an exponential function in theory. However, as an exponential function is more sensitive to variations in the gradient, the extrapolated value at $z = 0$ has great uncertainty. Since the purpose of this study is to introduce, demonstrate and discuss this new technique, linear extrapolation avoids the otherwise necessary rigor in mathematical treatment. However, optical improvements reducing the FWHM (e.g. increased NA) would make fitting of an exponential function to the measurement points more feasible and more precise extrapolation of membrane wall concentration could be achieved.

Direct measurement of the membrane wall concentration could be an area of special consideration using the same principal technique. The setup can be adjusted to get close to the achievable optimum of less than 2 µm in depth resolution by using an immersion objective with a high NA. Such a setup would have a much shorter working distance but in turn, due to the immersion, would exhibit less optical distortions decreasing effective depth resolution. The challenge of such a setup would be to solve issues like the obstruction of feed channel flow by the objective, pressure resistance and sealing.

In conclusion, these considerations allow for the extraction of some important parameters from the sulfate concentration plot (Fig. 2.9). For a feed sulfate concentration of 10 $g \cdot L^{-1}$, linear extrapolation (data points z = 30 to 50/60 µm) to the membrane gives a membrane wall concentration (c_m) of sulfate of about 18 $g \cdot L^{-1}$ at a velocity of 0.04 $m \cdot s^{-1}$ (CPF = 1.8) and 15 $g \cdot L^{-1}$ at a velocity of 0.2 $m \cdot s^{-1}$ (CPF = 1.5) at 7.2 bar TMP. The boundary layer thickness is about 130 µm and 90 µm respectively. Both values, thickness and wall concentration, are subject to some uncertainty since they are derived from extrapolation and fitting to the measurement values and should be interpreted accordingly. Reproducibility of measurements is good. Standard deviation (SD) between independent measurements is about 2%, which corresponds to about 0.2 $g \cdot L^{-1}$ absolute for the sample solution of 10 $g \cdot L^{-1}$ sulfate concentration in the feed. The SD increases in the area 0 to 20 µm, which however is inconsequential since the measurement technique fails to produce accurate values in that area due to the overlap of the PSF with the opaque membrane.

The extent of CP (i.e. the CPF) measured with this new method is within plausible range as reported in literature, e.g. Kim and Hoek (2005), Qiu and Davies (2015) and Salcedo-Díaz et al. (2014). However, it is important to note, that a comparison with different setups and simulations in literature is of limited value as the CPL characteristics are very dependent on the system, the operating conditions (see chapter 3.2) and the membrane and water type. Furthermore, most approaches in published literature do not measure the CPL directly but calculate the CP from indirect measurements. An exception is the group of Salcedo-Díaz et

al., who measured CPL using Digital Holographic Interferometry in a slit-type channel with a sodium sulfate solution and about similar active membrane area, Reynolds numbers and channel length, which makes their work the most comparable to the present study. The authors report a CPF between 1.7 and 1.2 for the low Re case and 1.4 and 1.1 for the higher Re case (compared to 1.8 and 1.5 in the present study) (Salcedo-Díaz et al. 2014). When comparing this study to other experimental or theoretical work, at least the following parameters unique to the present study should receive careful consideration: feed of a pure magnesium sulfate solution, which has 40% less osmotic pressure than a sodium chloride solution of the same molality, feed channel dimensions, i.e. height and width, point of measurement along the feed channel, no feed spacer, active membrane only at one side of the feed channel and an active membrane area of only 33.6 cm².

The spherical aberration occurring with the setup used in this work cannot easily be remedied. If the goal is to image CPL in practical RO membrane application, a transparent cover is necessary to enclose the pressurized feed channel and to not obstruct feed channel flow. The feed channel is also of a certain thickness, typically about 0.8 mm in common RO modules, and the working distance of the objective lens has to be long enough to cover the entire feed channel height to the membrane surface. Thus, the objective lens has to correct for the coverslip and deep penetration into refractive media while maintaining a high numerical aperture. These are extraordinary requirements for an objective lens. Mathematical modelling in order to predict depth resolution and depth scale compression is also complex(Everall 2009). The use of a confocal aperture can restore some of the loss in depth resolution but at the cost of significant Raman intensity loss. Nevertheless, the technique shows that CPL can be recorded until close range to the membrane and in practical flow conditions. Furthermore, the technique offers the possibility to also measure CPL with a spacer present in the feed membrane channel since the optical axis is in *z* and the spatial resolution in the xy-plane is high. Thus, 3D measurement of the sulfate concentration distribution inside individual spacer mesh elements is achievable.

2.3 Conclusion

The present work demonstrates the applicability of RM for the measurement of CP in a NF setup representative of commercial spiral wound modules. The major challenge with the setup is the occurrence of spherical aberration, which causes a deterioration of the depth resolution and widening of the PSF. The theoretical minimal achievable depth resolution of about 2 µm cannot be reached with the present setup. Instead, the depth resolution near the membrane

surface is only about 75 µm. Nevertheless, since CP is a continuous concentration profile, depth profiles can be recorded with a resolution of less than 5 µm by observing the changes in Raman intensity throughout the depth profile. Therefore, the main finding of this study is the difference in Raman intensity profiles between unpressurized/no-flux and pressurized/flux operation shown in Fig. 2.8. The difference in profiles is entirely caused by CP. Due to the linear correlation of Raman intensity and sulfate concentration, the Raman intensity data can be converted to quantify CP. However, the conversion of the raw data into concentration values is hindered by the optical distortions present. This study used a calibration approach to correct for the complex optical effects. This approach produces a viable sulfate concentration profile, which however cannot resolve data points close to the membrane surface (0 to 20 µm). A reasonable estimate of the membrane wall concentration and the CPF can be obtained by extrapolation. The thickness of the boundary layer can be corrected with FWHM/2 to account for the broader PSF. Other conversion options, in particular an approach assisted by mathematical modelling of the optical effects, should be explored to improve results.

This work used the best simple setup available as well as a simple calibration routine with no sophisticated mathematical editing. The CPL was imaged successfully within an unobstructed feed channel without feed spacer at velocities of 0.04 $m \cdot s^{-1}$ and 0.2 $m \cdot s^{-1}$. The concentration polarization factor could be estimated from the profile to be about 1.8 for low velocity and 1.5 for high velocity respectively. The present setup did not use spacers nor did it utilize a natural brackish water feed in order to simplify fluid dynamics and optics as well as maximize the CPL. The setup however does not limit the applicability of spacers and Murata et al. have shown that Raman spectroscopy can be used for the measurement of sulfate in natural brackish waters (Murata et al. 1997). Furthermore, since RM is a strong tool for material characterization, it allows for the differentiation of dissolved compounds ($sulfate_{(aq)}$) and solids (e.g. crystals of gypsum). The herein presented method demonstrates on a specific example of NF with sulfate how to achieve quantitative assessment of the CPL of Raman active compounds in membrane applications such as NF and RO. Yet it can be applied more broadly to characterize mass transfer in feed membrane channels and may also be applicable to related fouling phenomena. It provides experimental *in-situ* data in a research area where such data is scarce in literature and which relies primarily on modelling.

3 3D Analysis of Concentration Polarization in a NF Membrane Unit with/without Feed Spacer

In the previous chapter Raman microspectroscopy was established as a principal tool for measuring the concentration gradient in a nanofiltration flow cell. We are now aware of the methodology required and the challenges associated with the technique. However, the previous chapter has only explored one important variable, i.e. cross-flow velocity, and was restricted to a point measurement at a fixed position along the feed channel. Furthermore, the fluid dynamics were deliberately kept as simple as possible to not introduce complexity to the proof-of-concept type study. In this and the next chapter, the measurement technique is explored further to gauge the potential and applicability of the method for standard NF/RO and/or other membrane applications.

Considering the challenges associated with *in-situ* measurement, the focus in understanding mass transport in membrane channels has been on modeling. Unfortunately, experimental studies have not been able to keep up with the advances in modeling. For example, no method so far, has allowed for measurement of mass transport in spacer-filled channels, which is a standard in cross-flow membrane filtration. However, modeling the mass transport and the fluid dynamics in spacer-filled channels has produced valuable results, reducing the apparent need of measured data. For example, Picioreanu et al. (2009) have modeled the flow conditions in a spacer filled channel and combined it further with the event of biofouling. This allowed the authors to make predictions about the fouling impact and the impact of spacer geometry. Particularly, the authors point out how important a realistic model of the spacer geometry is for a representative simulation result. This is exemplary for the challenges the modeling approach faces in having to judge where to most efficiently spend resources to adequately factor the impact of certain parameters. This is why, ideally, modeling and experimental measuring would develop jointly with both approaches informing each other to better understand the phenomenon in question. With experimental studies being so far behind, perhaps as a direct result, modeling research has seen a decline in publications recently, while publications in most other areas of membrane separation are growing (Oatley-Radcliffe et al. 2017). However, understanding the CPL on the feed side in nanofiltration and reverse osmosis is of particular importance, still, as it governs most aspects of membrane performance, impacting not only fluid considerations. For example, García-Martín et al. (2014) are highlighting the importance of obtaining accurate membrane wall concentrations for the trustworthiness of models on pore size distribution for NF membranes.

The studies presented in this chapter aim to reduce the gap by making use of the ability of RM to acquire 3D data of the CPL with and without the presence of a feed spacer. Acquiring measured data in conditions with more complex fluid dynamics are key for challenging current modeling approaches. Furthermore, the collected Raman data is linked to the general performance parameters of the membrane filtration system where applicable.

3.1 Materials & Methods

This study is based on the setup introduced in the previous chapter for RM measurement of the CPL in a cross-flow nanofiltration system representative of practical spiral-wound modules (section 2.1). In addition, a 28 mil feed spacer taken from a commercial DOW FILMTEC™ module was used for some experiments. Furthermore, the system was operated with increased recovery of up to 30%. A scheme of the setup is shown in Fig. 3.1 with the most important measurement conditions specified. The locations accessible to Raman measurements are marked as red squares in the cell and on the membrane. The size of the squares is relative to total membrane dimensions.

The membrane filtration setup is operated in complete recirculation with permeate and concentrate being jointly rerouted into the feed supply with no loss of volume. Hence, the feed is of constant solute concentration throughout the measurement. The membrane unit is operated in cross-flow conditions. A 0.22 µm particle filter is keeping the sample solution free of particles. The feed container is temperature regulated to keep sample temperature constant. The feed solution is concentrated well below saturation to exclude the possibility of scaling. In conclusion, the setup keeps all relevant parameters constant to stabilize the CPL.

NI LabVIEW™ was used to record inlet and outlet pressure, temperature and brine and permeate flow rate. Permeate flow rate was measured before and after Raman measurements by weighing. Salt concentration was determined by conductivity measurements in feed, permeate and concentrate. All experiments were conducted with a pure magnesium sulfate solution of varying concentrations between 7 and 30 $g \cdot L^{-1}$ (0.073 to 0.313 $mol \cdot kg^{-1}$). The solution was made from deionized water and magnesium heptahydrate from Roth (99.7 % purity). The high solubility of about 300 $g \cdot L^{-1}$ (3.13 $mol \cdot kg^{-1}$) at room temperature avoids precipitation in the membrane cell even at the higher recoveries obtained.

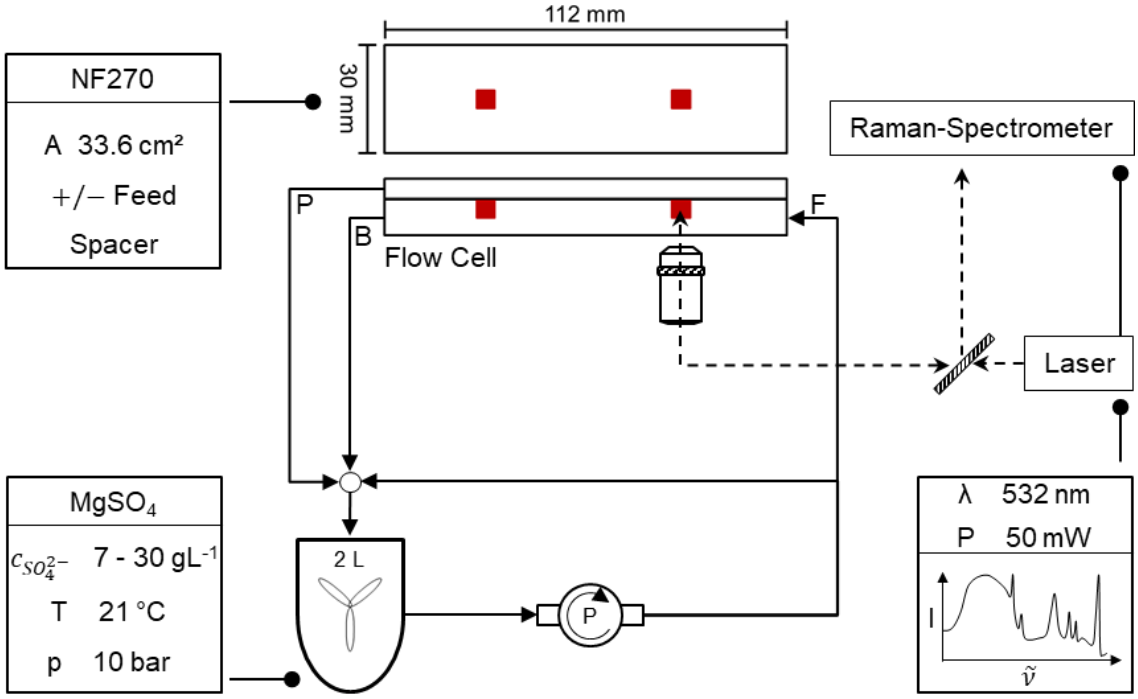

Fig. 3.1 Scheme of the closed cross-flow nanofiltration-Raman-setup with complete recirculation. Red squares show the locations accessible for Raman measurement (5×5 mm). The microscope is of inverted configuration. The membrane is positioned on top of the feed channel. F: feed, B: brine/concentrate, P: permeate/filtrate. Boxes show membrane data, operational data, laser specifications and Raman output (Raman spectra).

The membrane cell was designed to mimic conditions in common spiral wound modules. Total membrane area is 33.6 cm² at a channel length of 11.2 cm. A 28 mil (thickness of 711 µm) spacer can be used in the feed channel. The cell features two sapphire windows of 1.3 mm thickness. The windows demonstrate excellent pressure resistance and provide cell integrity at higher operating pressures. Placement of the windows enables 3D Raman mapping of two areas, each about 36 mm². Both areas are in the center of the feed channel. The first area starts 2.6 cm past the inlet and the second area covers a length of 8.1 to 8.7 cm past the inlet.

Membrane sheets used were cut from a single sheet of DOW FILMTEC™ NF270 nanofiltration membrane. Clean water permeability was recorded as 13.1 $L \cdot m^{-2} \cdot h^{-1} \cdot bar^{-1}$. Rejection of magnesium sulfate was determined to be greater 95 % for all relevant operating conditions. The NF270 membrane is a thin-film composite membrane with an active layer of polyamide (PA) and a supporting layer of polyether sulfone (PES).

The Raman microscope is a SENTERRA I from Bruker in inverted configuration. The inverted configuration means that the membrane is located on top of the feed channel as shown in Fig.

3.1. Thus, the direction of filtration is against gravity. The direction of Raman measurements for the depth profiles is towards the membrane and covers half the thickness of the feed channel. The root point for the coordinate system was set to the bottom left corner of the membrane (Fig. 3.2). The center of the flow channel is at y = 15 mm and the beginning of the flow channel is at x = 0 mm. The SENTERRA I is equipped with a 532 nm laser (Cobolt Lasers, Solna, Sweden) with a nominal power of 50 mW. The confocal aperture in front of the spectrograph is set to a 50×1000 µm slit for high signal throughput. The objective, Olympus LUCPLFLN 60×, has a NA of 0.7, magnification of 60×, working distance of 1.5 mm beyond cover glass and is corrected for a cover glass thickness of 1.3 mm (thickness of the sapphire windows). Spectra are recorded using OPUS 7 software. The Raman raw signal output is a light intensity (I) over wavenumber shift ($\tilde{\nu}$) as shown in the box in Fig. 3.1. The integral of a Raman band correlates with the concentration of the species responsible for the signal peak. Sulfate is Raman active with four vibrational modes. The linear stretching vibration (1st mode $\tilde{\nu}_1$) shows one distinct Raman band at $\tilde{\nu}$ = 994 -966 cm^{-1} with a peak at 981 cm^{-1} (Fig. 2.4). This Raman band is used to measure the concentration distribution of sulfate within the feed channel. The supporting layer of the membrane (PES) shows three distinct Raman bands at wavenumber shift ($\tilde{\nu}$) 1165 to 1060 cm^{-1}. The cumulative band area over these three bands is used to identify the membrane. The maximum Raman intensity of this signal was then used to identify the location of the membrane surface, setting z (distance along optical axis) to z = 0 µm for this position. The NF270 shows no Raman interference with the sulfate band area.

As has been explained in chapter 2, the measurements presented in this study require two modes of operation, a calibration setting and a measurement setting (section 2.1.2). In the calibration setting, no flux should occur and the solute concentration is varied for the range expected in the subsequent measurement run. The recorded calibration data set allows for the conversion of Raman intensity to sulfate concentration for each point in the 3D measurement matrix. For the 1D and 3D measurements performed without feed spacer, the sulfate concentrations applied for calibration were 7, 10, 15, 20, 25 and 30 g·L^{-1}. For the 3D measurements with feed spacer, 7, 9, 10, 11, 12 and 15 g·L^{-1} were applied. All calibration runs were performed with a velocity of 0.04 m·s^{-1}. Pressure was only applied to keep a constant flow rate (about 150 mbar).

The measurement setting was fixed to a constant system pressure of 10 bar. At this setting a steady state CPL is formed quickly. Due to the high solubility of magnesium sulfate, no scaling can occur and all parameters are kept constant. Variables in the measurement setting are feed sulfate concentration, cross-flow velocity and presence of feed spacer. Feed sulfate concentration was varied between 10 and 20 g·L^{-1} (0.104 and 0.209 mol·kg^{-1}). Thus, due to

the osmotic pressure difference of the two concentrations, effective TMP is also varied with 7.2 and 4.4 bar respectively (i.e. before formation of the CPL).

Cross-flow velocity was varied by adjusting the brine flow rate. Cross-flow velocity is not constant through the feed channel due to the laminar flow profile and filtration. With greater recovery, a greater variance of cross-flow velocity between inlet and outlet occurs. Therefore, the velocity is an average value and was set to about 0.2, 0.04 and 0.004 $m \cdot s^{-1}$ as mean velocities for the individual measurement runs. The RM measurements were done with the inverted microscope setup, which means that the membrane was located at the top of the feed channel. This orientation is referred to as “TOP”. Additional experiments were performed to measure general membrane performance parameters with the opposite orientation, i.e. membrane located on the bottom of feed channel. This orientation is referred to as “BOTTOM”. In BOTTOM configuration no Raman measurements could be conducted as the Raman microscope can only be operated in its inverted configuration.

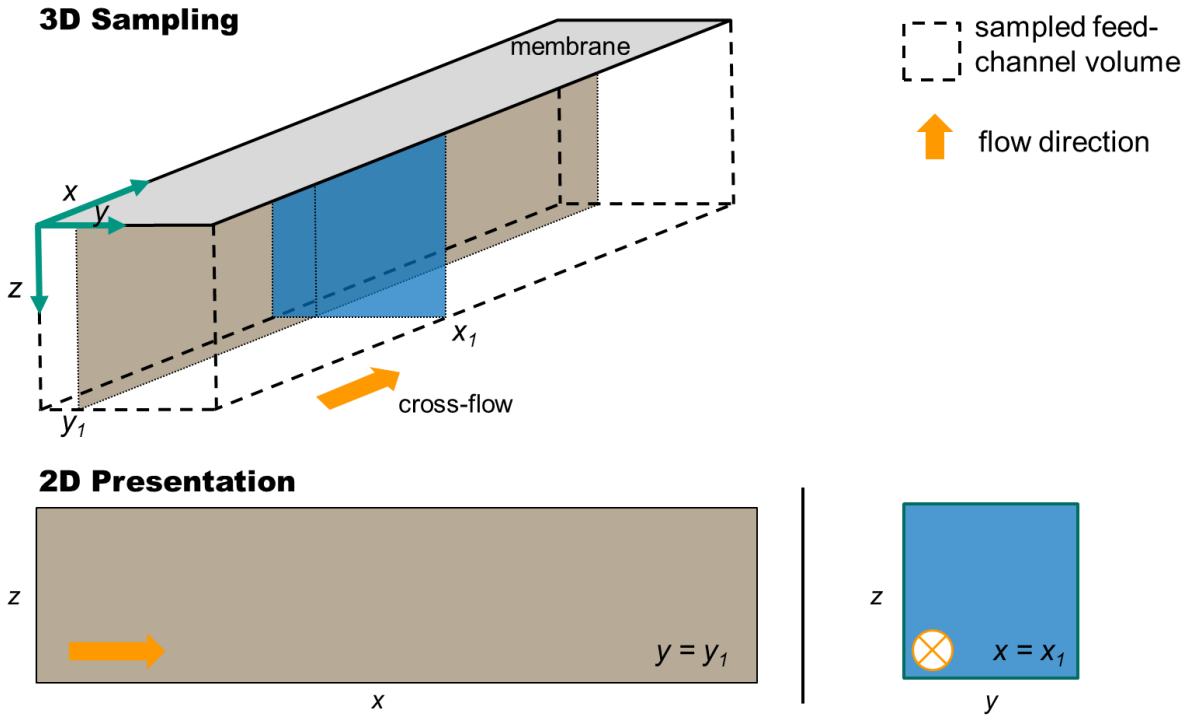

Fig. 3.2 Coordinate system for sample volume and format for data presentation in 2D

3D Raman mapping is done by specifying a 3D grid of independent resolution in *x*, *y* and *z*. Data is measured at every node of the grid. Resolution of *x* and *y* varies in the study while resolution of *z* is fixed in all measurements to 10 µm. The 3D mapping data is presented as

2D cross-sections at a specified cut-out location. Figure 3.2 shows the principal scheme for this study. The graphs were made with OriginLab™ Origin 7 software. Data in between the grid nodes is interpolated using the default Origin settings for contour plots.

3D Raman mapping made use of the two sampling modes shown in Fig. 3.3. Common to both is the time of illumination per focus point (time of exposure). Total exposure time is 30 s per focus point, which is divided into 6 times (co-edition) of 5 s exposure (integration time). This yields a joint output of one spectrum. 1D measurements are depth scans with each depth point being recorded consecutively towards the membrane surface. A series of 1D measurements can be bundled into a 3D map. This is the “point for point” sampling mode. The second sampling mode is “plane for plane”. At this mode, all points in a plane at the same depth are recorded before moving on to the next depth point. The difference of the two modes is the time sensitivity towards changes along the axes. At a resolution along the optical axis (z) of 10 µm, 36 points are necessary to yield a profile from z = 0 to z = 350 µm with z = 0 µm being the membrane surface. Total measurement time for this case would be 20 min to record one 1D depth profile through half of the feed channel height. Extracting the same 1D measurement from the “plane for plane” sampling mode, data collection is spread over a much longer time. Total measurement time of recording 36 planes varies with the number of measurement points per plane and takes up to 30 h for the high-resolution images presented in this study and about 5 h for the low-resolution images.

Raman measurement data sets are converted to sulfate concentration using a Raman calibration data set with the same sampling grid. Calibration was done once before a measurement series. The calibration data set has two functions. First, it correlates the Raman intensity values to sulfate concentration (COD for all points is greater 0.994) and second, it corrects for spherical aberration.

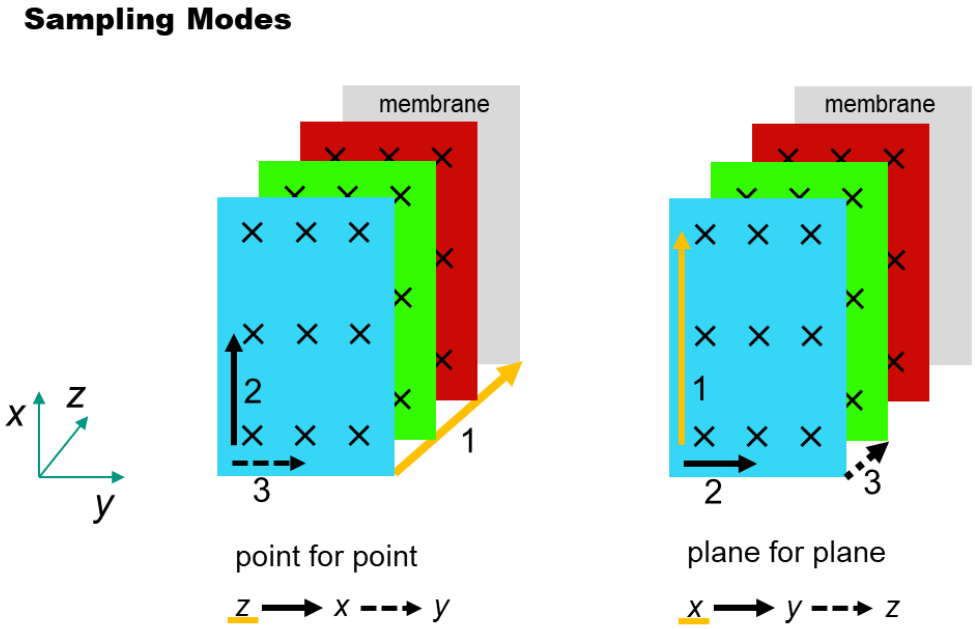

Fig. 3.3 Comparison of sampling modes for data acquisition. Point for point: series of 1D depth profiles. Plane for plane: series of 2D depth profiles.

In chapter 2 it was established, that an "oversampling" occurs along the *z*-axis with the resolution of the sampling grid (10 µm) being higher than the depth resolution (75 µm). Rather than a "pure" signal intensity, the depth profiles show changes in signal intensity from one focal plane to the next. The Raman setup is sensitive enough to resolve these changes with a resolution along *z* of at least 5 µm (section 2.2.1). The spatial resolution of the optic setup was not determined. Spatial resolution is also affected by the refractive power at various interfaces but less than the depth resolution. Therefore, data points in the *x*-*y*-plane are considered "pure" with a spatial resolution of the sampling grid of 75 µm or more.

3.2 Results and Discussion

General Filtration Performance Parameters

The general performance parameters, i.e. flow rates, pressure and conductivities, are the most trustworthy data obtained from the membrane system but only inform globally, showing an average over the entire membrane module. Permeate flux and rejection are higher at the beginning of the flow channel and lower towards the end since effective TMP decreases with concentrating the bulk solution. Yet, the present system does not allow to measure this

difference. However, the RM measurements are locally resolved and should show expected qualitative differences. Those results have to be in agreement with the general performance data.

In this study, system pressure is kept constant at 10 bar and only flow rates (cross-flow velocity) and feed concentration are adjusted. In a cross-flow NF system at constant pressure, decreasing cross-flow velocity (u) increases recovery (Δ) and brine concentration. Higher brine concentration decreases TMP and, thus, leads to decreased permeate flux (J_P). Solute flux (J_S) is determined by the solute concentration at the membrane surface (c_m). With higher concentration, solute flux increases and rejection (R) is diminished. Decreased rejection also points to more severe concentration polarization (CP). Overall, this means that by decreasing cross-flow velocity, rejection and permeate flux should decrease while recovery increases. The overview of performance parameters in Table 3.1 confirms, that the present system behaves accordingly. Also, a feed spacer increases mass transfer and decreases the effect of CP. Hence, a feed spacer leads to increased permeate flux, which the data also shows. However, only at the lowest cross-flow velocity of 0.004 $m \cdot s^{-1}$, the data suggests an influence of membrane orientation. Recovery and rejection are substantially increased with the membrane orientation “TOP” (underlined values). The effect is similar to the effect of the feed spacer suggesting increased mass transfer with the “TOP” orientation. This interesting finding will be discussed in detail later.

Table 3.1. General membrane performance parameters at constant system pressure of 10 bar. Application with and without 28 mil feed spacer. Orientation “TOP”: membrane on top of feed channel (filtration against gravity), Orientation “BOTTOM”: membrane on bottom of feed channel (filtration in direction of gravity)

Flux J_P, $L \cdot m^{-2} \cdot h^{-1}$	Recovery Δ, %	Rejection R, %	Velocity u, $m \cdot s^{-1}$	Sulfate Concentration in Feed c_{feed}, $g \cdot L^{-1}$
Feed Spacer: No				
Orientation: TOP				
41.1	1.0	98.1	0.2	10
24.9	2.8	98.3	0.04	10
22.9	25	98.0	0.004	10
19.8	0.5	97.8	0.2	20
12.9	1.6	97.1	0.04	20
9.6	12	97.2	0.004	20
Orientation: BOTTOM				
24.8	2.8	98.2	0.04	10
12.2	15	96.6	0.004	10
5.9	6.7	96.0	0.004	20
Feed Spacer: Yes				
Orientation: TOP				
53.0	6.5	98.0	0.04	10
27.4	31	96.9	0.004	10
Orientation: BOTTOM				
26.5	28	96.5	0.004	10

System stability

Membrane filtration in a system with no fouling and with recirculation of all volume streams is a stable system, which reaches an equilibrium state quickly. Therefore, observation of the CPL is not time sensitive after the CPL is established, which occurs within a timeframe of seconds in the present system. This can be verified globally with measuring the general performance parameters. A change in system pressure or flow rate changes permeate flux as well as permeate and concentrate conductivity. These changes are recorded without delay and remain stable as long as parameters are constant. This stability was also verified locally by comparing the data of the first and second sampling mode for a 1D depth profile. In the first case the depth profile is recorded within a timeframe of 20 minutes. In the second case, the depth profile of the same point is collected over a timeframe of 5 hours or more. In both cases, the exposure time to the laser is identical at each point. The experiment results show that, indeed, in both cases the same depth profile is obtained at laminar flow conditions. Thus, the results show that, at laminar flow conditions and with constant operating conditions, CP is a steady state phenomenon globally as well as locally on a microscale.

3.2.1 RM Measurements without Feed Spacer

In chapter 2, the RM results have shown the change in the CPL with variation of cross-flow velocity at a specific position of the feed channel. Fig. 3.4 A and B show the mean of several independent measurements with the same variation in velocity but with the additional variation of feed concentration and at an additional position. Each measurement run was distinct, meaning that operating conditions were set from unpressurized operation before each recorded data set. Depicted is the concentration polarization factor (CPF), which is the sulfate concentration (c) relative to the sulfate concentration in the feed (c_{feed}). Mean cross-flow velocity was set to 0.04 and 0.2 $m \cdot s^{-1}$ and sulfate concentration was set to 10 and 20 $g \cdot L^{-1}$. With the change in concentration, effective pressure is varied from 7.2 to 4.4 bar. Recovery is decreased by about 50% at the lower effective pressure, which suggests a smaller CPL since convective flux to the membrane is reduced. The decrease in cross-flow velocity by a factor of 5 leads to an increase in recovery by about 300% with the expectation of a bigger CPL.

Looking at the CPF, the RM data shows higher CPF values for lower cross-flow velocity. The actual maximum CPF measured is 1.6 and 1.16 for 10 and 20 $g \cdot L^{-1}$ respectively in Fig. 3.4 B. However, these CPFs were measured 30 µm above the membrane. Closer 30 µm to the membrane, all measured depth profiles show a drop in value and an increase in standard

deviation. This is a measurement error and not a true representation of the sulfate concentration, as discussed in chapter 2. The measurement error is caused mainly by overlap of the focal volume with the opaque membrane due to the relatively poor depth resolution of 75 µm. Additionally, the calibration methodology fails to work when calibration conditions and filtration conditions are significantly different. Due to the exponential shape of the CPL, the greatest divergence between the two conditions is present in direct vicinity of the membrane surface, which may contribute to the measurement error. In conclusion, the calibration does not accurately correct for optical aberration, which results in major undervaluation of the concentration in the CPL in the area 0 to 30 µm above the membrane. Thus, membrane surface concentration needs to be estimated by extrapolation.

Extrapolation according to the methodology in chapter 2 for Fig. 3.4 B gives CPFs of 1.8 and 1.5 as well as 1.35 and 1.1 for the two concentrations respectively. The associated recoveries are 2.8 and 1.0 as well as 1.6 and 0.5%. The CPL should be more severe with increased recovery. However, the concentration profiles seem to suggest a more severe CPL for a recovery of 1.0% compared to 1.6% (black triangles and white circles). This is, in fact, not the case. Plotting the CPF leads to flatter profiles for higher feed concentrations. In absolute terms, the concentration gradient (dc/dx) is a better representation of the severity of CPL. With a CPF of 1.35 at c_{feed} = 20 g·L^{-1}, the value for Δc is 7 g·L^{-1}, while for a CPF of 1.5 and c_{feed} = 10 g·L^{-1}, the value for Δc is 5 g·L^{-1}. Thus, the measurements show that the CPL is increasing consistently with increased recovery in agreement with the FT-model.

The comparison of Fig. 3.4 A and B shows that the CPL builds up gradually along the feed channel. The CPF increases by 20% from x = 30 to x = 85 mm for all conditions. With the high cross-flow velocity and low effective TMP scenario, no CPL could be measured at x = 30 mm. Considering that at x = 85 mm the CPF for this scenario is about 1.1, the CPF is expected to be close to 1.

The CPL thickness (δ) of the measured profiles show the same general trend of increased thickness with higher recovery. Although δ appears to be similar for c_{feed} = 20 g·L^{-1}, u = 0.04 m·s^{-1} and c_{feed} = 10 g·L^{-1}, u = 0.2 m·s^{-1} despite the difference in recovery (1.6 and 1.0%), again, it should be noted that the CPL profiles for the high concentration are flatter, suggesting a greater thickness, which the measurement could not sufficiently resolve. The flatness of the profiles at the onset of the CPL poses difficulties in exact quantitative determination of δ. Nevertheless, the change in cross-flow velocity from 0.04 to 0.2 m·s^{-1} can be estimated to increase CPL thickness in the range of 30 to 40% for both positions and both concentrations.

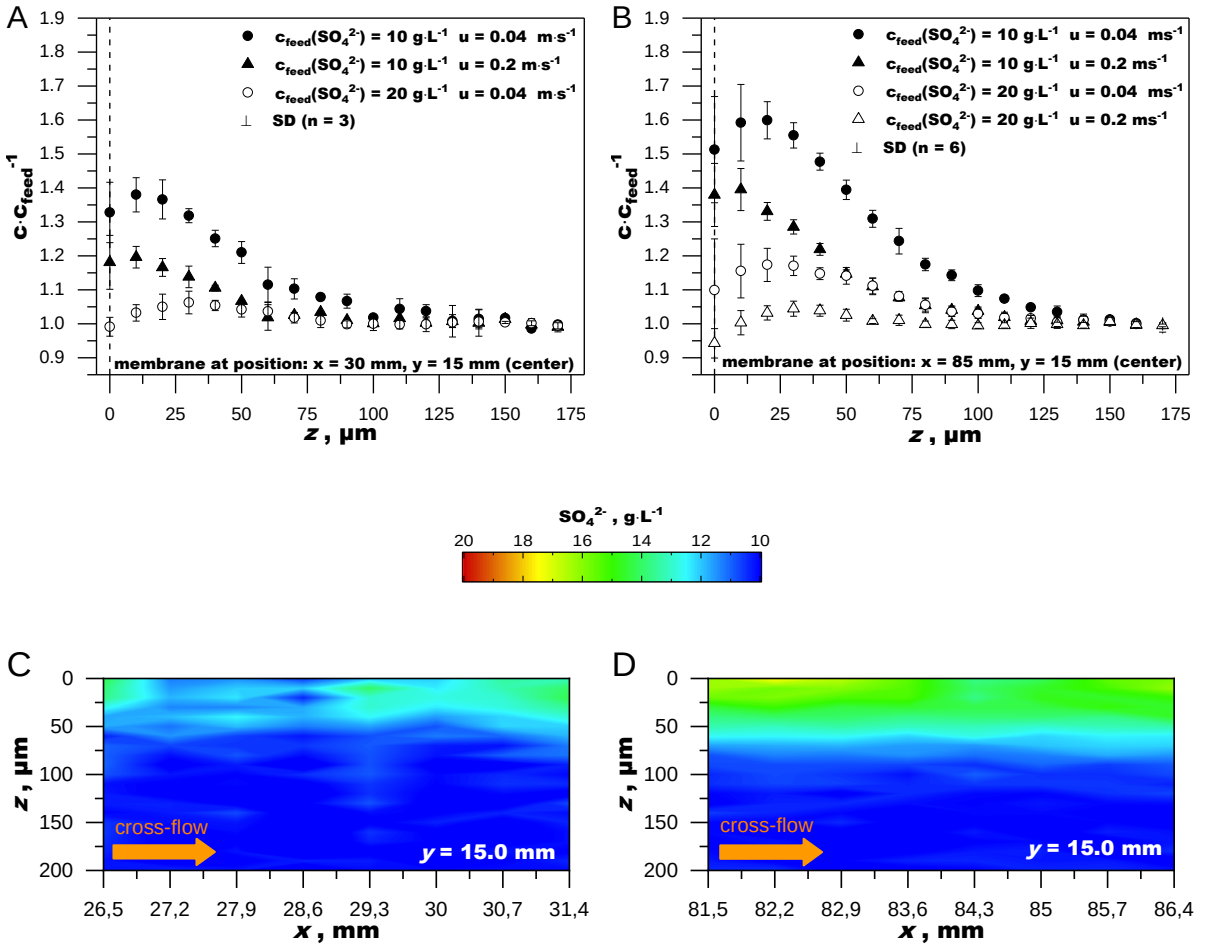

Fig. 3.4 CP profiles measured with RM at both windows of the membrane flow cell without feed spacer at two feed sulfate concentrations (10 and 20 g·L^{-1}) and two mean cross-flow velocities (0.04 and 0.2 m·s^{-1}). System pressure: 10 bar. A: Window 1, center (y = 15 mm) of feed channel 30 mm from inlet, shown is the relative increase in the CPL compared to the feed concentration (c·c$_{feed}^{-1}$); B Window 2, center of feed channel 85 mm from inlet; C and D: development of CPL along (x) the center of feed channel for both windows (specific measurement with c_{feed} = 10 g·L^{-1} and u = 0.04 m·s^{-1}), *Resolution: z: 10 µm; x: 700 µm*

Figures 3.4 C and D show the buildup of the CPL along the feed channel as 2D contour plots for the higher recovery (2.8%) scenario. In the first window (C) the CPL appears not yet fully established, while in the second window (D) a dense CPL can be seen. With the color legend ranging from 10 to 20 g·L^{-1}, it would be expected to see the color progressing to orange at the membrane surface if data was not undervalued at the membrane surface. It should be kept in mind, that the RM data is only accurate to about 25 µm above the membrane surface (first dash). Nevertheless, this data was not excluded in order to not skew perception of CPL thickness and membrane location.

High Recovery - Low cross-flow Velocity

With spiral wound modules, practical recoveries can reach 15% or more per membrane element(DOW 2005). To get similar recoveries with the setup used in this study, the mean cross-flow velocity was reduced to 4 $mm \cdot s^{-1}$. At that velocity, a recovery of 15% is obtained with the membrane at the bottom of the feed channel. However, for RM measurements with "TOP" configuration an increase in recovery to 25% is measured.

Fig. 3.5 shows a depth profile data set for the feed concentration of 10 $g \cdot L^{-1}$. The y-axis now shows the actual sulfate concentration rather than the CPF. Firstly, looking at the center of the feed channel (y = 15.0 mm) at x = 30 mm the depth profiles show an expected increase and buildup of the CPL. The CPL is much more severe than in the u = 0.04 $m \cdot s^{-1}$ scenario shown in Fig. 3.4 and builds up more quickly within a space of 5 mm (top left contour plot). The CPF is already greater than 2 only 26.5 mm from the inlet. However, off center (y = 14.7 and 15.3 mm) as well as further from the inlet (x = 81.5 to 86.4 mm) the measurement shows markedly different results. Off center, the CPL is diminishing along the same 5 mm space. The same can be seen further along the feed channel in the second measurement area at x = 81.5 to 86.4 mm. Furthermore, off center in the second area, the bulk concentration is noticeably increased (bottom center contour plot). The cutout view of the y-z plane shows a narrowly confined CPL, first in the center (x = 31.4 mm) and then further along off center (x = 84.3 mm) of the feed channel.

To summarize, the RM data shows, that the CPL is no longer building up gradually along the feed channel. Instead, the data shows confined areas of buildup and detachment throughout the feed channel. Furthermore, the bulk appears to be no longer uniform but to exhibit streams of high concentration. Detachment of the CPL reduces the solute concentration and, hence, allows for higher flux and higher solute rejection. Thus, the RM measurement data is consistent with the observed increase in recovery to 25% and the increase in rejection from 96.6 to 98.0%.

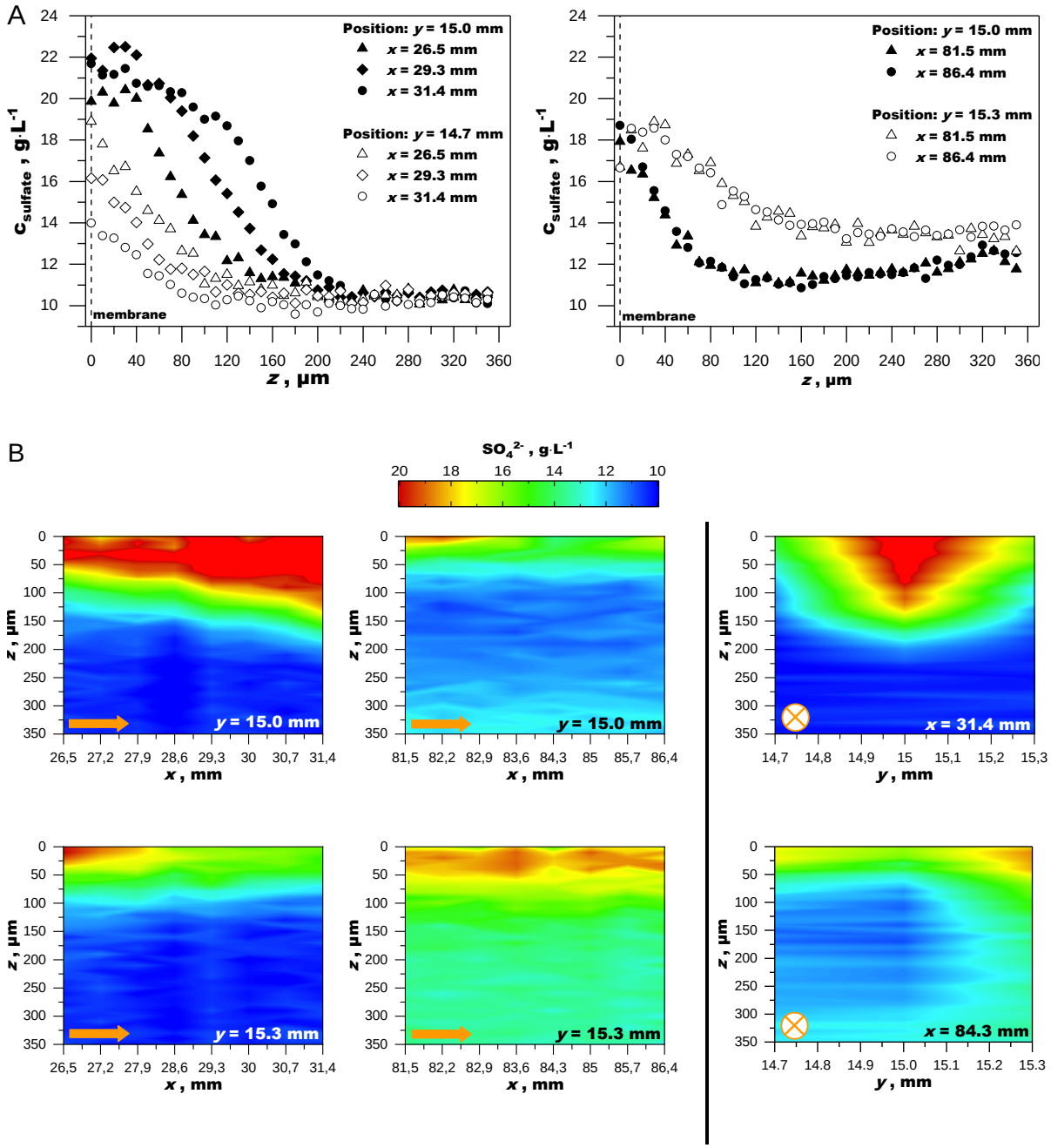

Fig. 3.5 Progression of CPL along center of feed channel: data set for system pressure 10 bar, cross-flow velocity 0.004 m·s^{-1} and sulfate concentration 10 g·L^{-1} in feed. A: 1D measurements; B: 2D graphs of 3D measurement showing the sulfate concentration along (left) and across (right) the center of the feed channel. *Resolution: z, 10 µm; y, 300 µm; x, 700 µm*

The RM results with a feed concentration of 20 g·L^{-1} depicted in Fig. 3.6 show the same trend and a similar pattern of the CPL. The buildup of CPL at x = 26.5 to x = 31.4 is not as severe, which is expected, since the effective TMP is reduced. Qualitatively, however, the concentration distribution within the feed channel is noticeably similar to the scenario in Fig. 3.5. Quantitively, it is noteworthy that bulk concentrations at and below the feed concentration

of 20 g·L^{-1} were measured. Particularly in the area x = 81.5 to 86.4 mm, y = 15.0 mm, low concentrations are measured close to the membrane (z = 50 - 200 µm). This is despite the expectation of generally increased concentration in the bulk at the end of the feed channel. This particular finding will be discussed later at the end of this section.

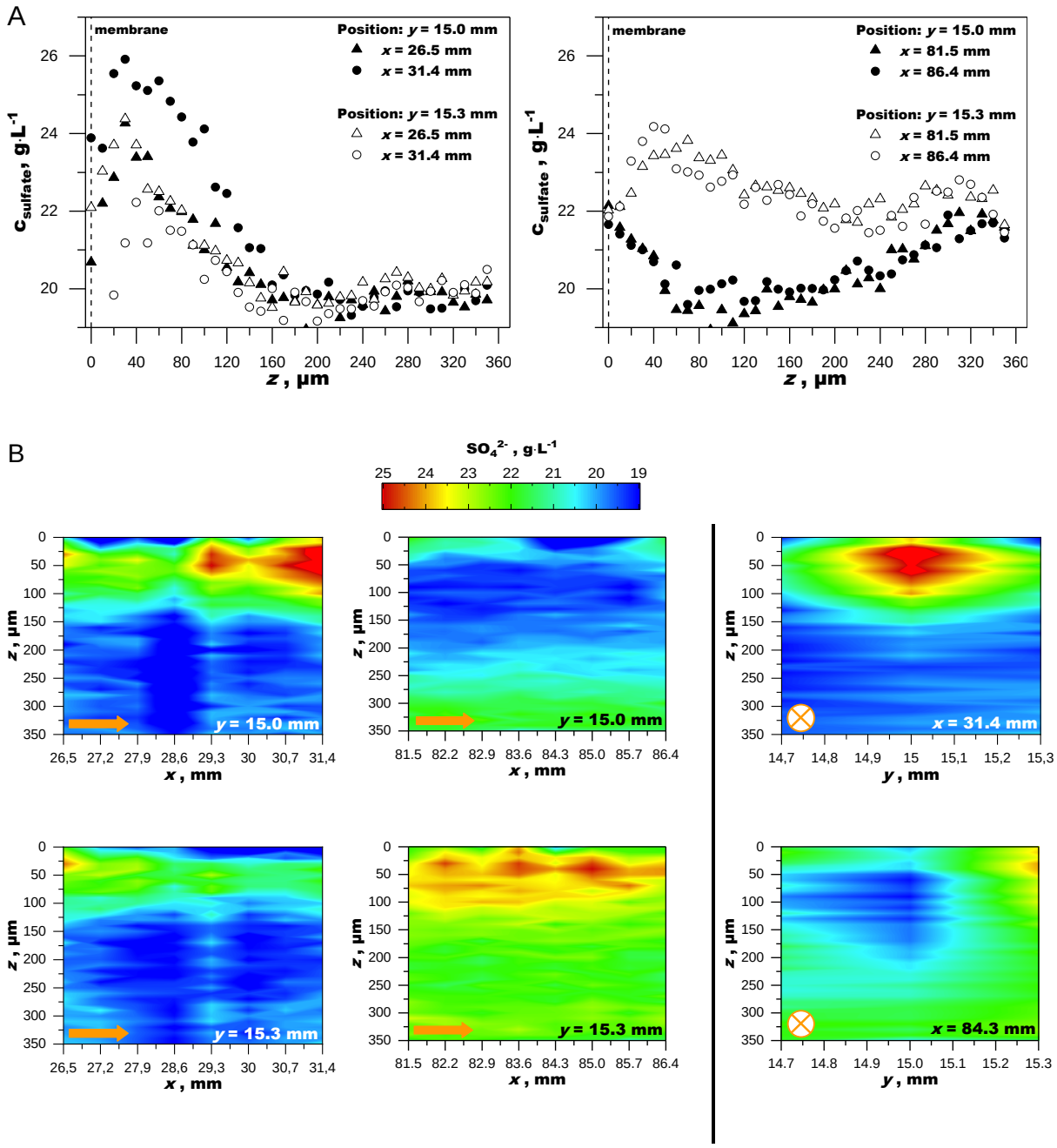

Fig. 3.6 Progression of CPL along center of feed channel: data set for system pressure 10 bar, cross-flow velocity 0.004 m·s^{-1} and sulfate concentration 20 g·L^{-1} in feed. A: 1D measurements; B: 2D graphs of 3D measurement showing the sulfate concentration along (left) and across (right) the center of the feed channel. *Resolution: z, 10 µm; y, 300 µm; x, 700 µm*

Firstly, to further clarify the mechanism of apparent detachment of the CPL from the membrane surface, high resolution images were recorded for measurement area 1, x = 26.5 to 31.4 mm. The spatial resolution of the grid was increased from 300 to 25 µm. Fig. 3.7 A shows three high resolution images of the center of the feed channel. The CPL builds up quickly to about 20 g·L^{1} (CPF = 2) at which point a process of detachment has started, which is evidenced by the accumulation of concentrate into a sphere. Over the next 4 mm, sulfate concentration in the center is further increasing and concentrated solution is displaced downward, forming a narrow stalactite structure (a “spike”), which appears to “bleed” into the bulk solution. With the displacement of concentrate volume downward, less concentrated bulk solution is displaced upward, pushing towards the membrane and diminishing the CPL off center. The width of the “spike” is very narrow at about 100 µm. The wide image (Fig. 3.7 B) shows this process happening at regular intervals, about 700 µm apart, across the feed channel. The measurements do also show that these structures are stable and a steady state phenomenon. This is confirmed by comparing the two sample modes specified in Fig. 3.3, which yield the same concentration profiles. The shape of the structures suggests that each forms a convection cell with a falling current at the center and a rising current off center. This describes natural convection.

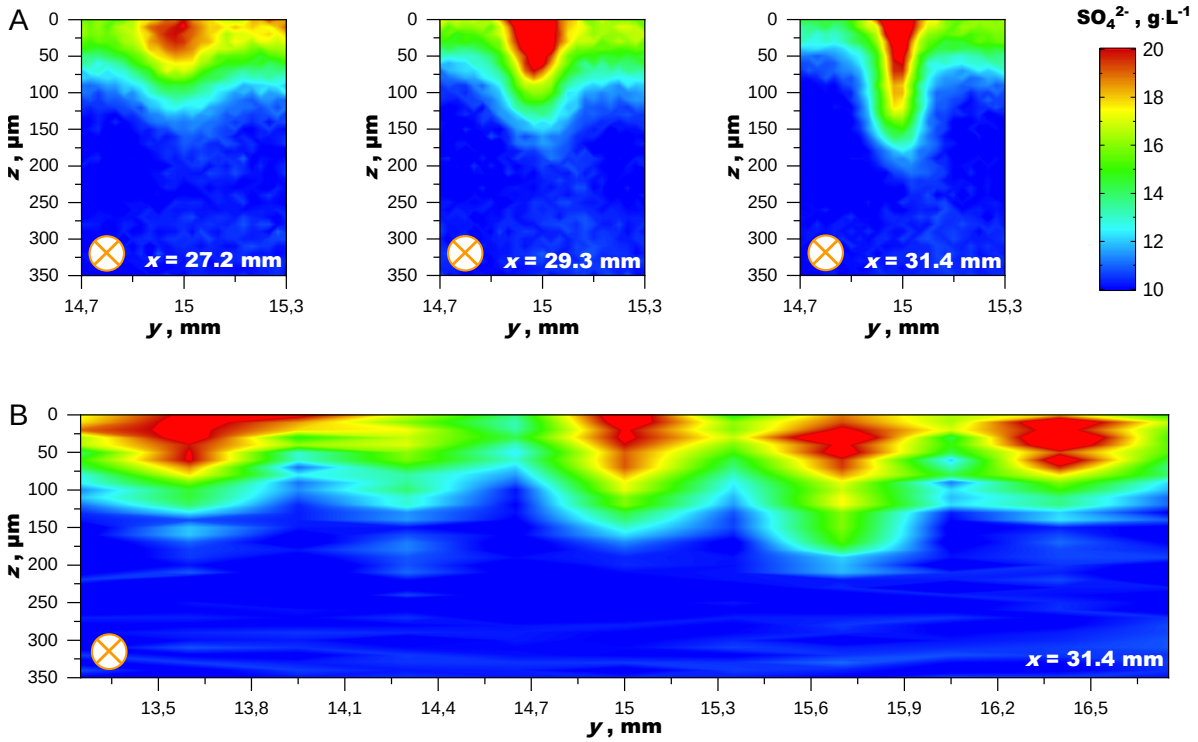

Fig. 3.7 A: High resolution 3D measurements of sulfate concentration at center of feed channel with cross-flow velocity of 0.004 m·s^{-1}, sulfate concentration 10 g·L^{-1} in feed. *Resolution: z, 10 µm; y, 25 µm*; B: Wider cross section of feed channel at position x = 31.4 mm. *Resolution: z: 10 µm, y: 350 µm*

Natural convection phenomena in low Reynolds filtration scenario with opposing membrane orientation have been reported in at least two studies using ultrafiltration (Cheng and Lin 2004, Youm et al. 1996). Both studies found substantially increased permeate flux at "TOP" membrane configuration compared to "Bottom" membrane orientation. Youm et al. (1996) reported a flux increase of 1.95 times without feed spacer and at a similar Reynolds number to this study. From Table 3.1, the permeate flux increase with opposite membrane orientation is 1.9 and 1.6 times for sulfate concentrations of 10 and 20 $g \cdot L^{-1}$ respectively.

Comparing all values from Table 3.1, we can deduce that the influence of natural convection is, at the least, dependent on membrane orientation, cross-flow velocity and the severity of CP. Table 3.2 lists three physical parameters of the sample solution, density (ρ), dynamic viscosity (η) and refraction index (n) for sulfate concentrations of 10, 20 and 30 $g \cdot L^{-1}$. The occurrence of CP increases density between bulk solution and solution at the membrane surface by 1.2% with a CPF of 2 (10 to 20 $g \cdot L^{-1}$) and by 2.4% with a CPF of 3 (10 to 30 $g \cdot L^{-1}$). Respectively, dynamic viscosity is increased by 7.1% and 14.2%. Solution of increased density is subject to greater gravitational force and lower density solution experiences buoyancy. Thus, the membrane orientation "TOP" is an hydrodynamically unstable orientation, at which solutions of varied density experience an acceleration towards each other. Furthermore, more viscous solution exhibits higher shear stress, slowing down transversal movement introducing interfaces with tangential velocity gradients. However, at higher cross-flow velocities, forced convection appears to mask natural convection phenomena.

Table 3.2. Physical properties of aqueous magnesium sulfate solution for 20 °C, 1 atm (values interpolated from values given in CRC Handbook of Chemistry and Physics (2005), Section 8).

$MgSO_4$ - magnesium $sulfate_{(aq)}$

Molality m, $mol \cdot kg^{-1}$	Density ρ, $g \cdot cm^{-3}$	Dynamic Viscosity μ, mPa·s	Refraction Index n
0.104	1.011	1.069	1.3355
0.209	1.023	1.145	1.3380
0.313	1.035	1.221	1.3404

Youm et al. (1996) have established a simple boundary condition for the occurrence of natural convection in a membrane filtration system using the dimensionless Reynolds (Re) and Grashof (Gr) numbers (Eq. 11). The Grashof number represents natural convection by describing the ratio of buoyancy to viscous force acting on a fluid due to concentration

gradients. The Reynolds number represents the term for forced convection due to cross-flow velocity. In other words, the Grashof number is representative of the severity of CP and the Reynolds number is representative of the rate of cross-flow velocity. If the ratio is greater than a threshold limit value (TLV), natural convection is expected to occur. The authors suggest a TLV of 1 to 3 for an empty channel (no feed spacer) (Youm et al. 1996).

$$\frac{Gr}{Re^2} \geq TLV \tag{11}$$

The Reynolds and Grashof numbers can be calculated according to Eqs. 12 and 13 with hydraulic diameter (d_h) being approximately twice the height of the thin feed channel (h), dynamic viscosity (μ), density of bulk solution (ρ_b), mean cross-flow velocity (u), thickness of the CPL (δ), gravitational acceleration (g) and the difference in concentration and density between bulk and membrane surface (Δc, $\Delta\rho$). The term "α" represents the volume expansion coefficient (buoyancy) due to concentration difference and the term "β" represents the concentration gradient (Youm et al. 1996).

$$Re = \rho_b \frac{u \cdot d_h}{\mu} \tag{12}$$

$$Gr = \underbrace{\frac{1}{\rho_b}\frac{\Delta\rho}{\Delta c}}_{\alpha} \cdot \underbrace{\frac{\Delta c}{\delta}}_{\beta} \cdot g \left(\frac{\rho_b h^2}{\mu}\right)^2 \tag{13}$$

Calculating Eq. 11 for this study using the results of the Raman measurements for CPL thickness (δ) and CPF, which were approximated from Figs. 3.4B (x = 85 mm, u = 0.04 m·s^{-1}), 3.5A (x = 26.5 mm, u = 0.004 m·s^{-1}) and 3.6A (x = 31.4 mm, u = 0.004 m·s^{-1}) yields the values presented in Table 3.3. In both cases where the ratio exceeded the proposed TLV natural convection was observed at the point of measurement as evidenced by the non-uniform concentration distribution. Since the point of measurement for both low cross-flow scenarios was within the first 25% of the feed channel length, natural convection causes substantial disturbance of the flow field through most of the feed channel. The improved mass transfer leads to the improved filtration performance, which is quantitively similar to the effect of a feed spacer (see Table 3.1).

Table 3.3. Ratio of Grashof to Reynolds squared (Eq. 11) for three filtration scenarios. At low Reynolds number natural convection was observed. Values for CPL thickness (δ) and CPF taken from Figs. 3.5A, 3.6A and 3.4B, density (ρ) and viscosity (μ) interpolated from Table 3.2.

$Gr \cdot Re^{-2}$	Re	Natural	CPF	δ
-	-	Convection	$g \cdot L^{-1}$	µm
6.3	5.2	Yes	2.4	200
4.6	4.8	Yes	1.4	160
0.05	51.8	No	1.8	150

Youm et al. (1996) as well as Cheng and Lin (2004) attributed their findings to natural convection generally but did not speculate about the type of convection instability. The measurement presented in Fig. 3.7 shows “spikes” and presents two solutions of different density being accelerated towards each other. The latter is the defining condition for Rayleigh-Taylor-Instability (RTI) and the former is a typical formation during the initial stage of RTI development (Kull 1991, Zhou 2017a). Thus, this study presents the first measurement of RTI in a nanofiltration membrane system. Mathematically RTI is described by a wave function. From Fig. 3.7, the distance between “spikes” represents the wavelength (λ) of the disturbance at the interface. The formation between “spikes” are called a “bubble”. “Spikes” are heavy solution pushing into light solution and “bubbles” are light solution pushing into heavy solution. The height difference between them is equal to two times the amplitude (a) of the wave function. The measurement suggests a wavelength of 700 µm and an amplitude of about 25 µm at x = 27.2 mm and about 65 µm at x = 31.4. From these values a growth rate of the amplitude can be calculated using the local cross-flow velocity. The initial growth rate of RTI is linear and can be described using the wavelength, gravitational acceleration and the Atwood number (A), a dimensionless density ratio. However, a modeling description of RTI for this system is outside the scope of this work and can be found in great detail in published reviews (Kull 1991, Zhou 2017a, b).

Another natural convection phenomenon to be considered is the Kelvin-Helmholtz-Instability (KHI). KHI occurs when there is a tangential velocity gradient between currents. The changes in the hydrodynamic flow field due to RTI inevitably introduce tangential velocity gradients but more importantly the cross-flow operation of the membrane system intensifies these gradients particularly towards the center of the feed channel. Rather than “spikes”, due to the cross-flow velocity, the formation across the membrane shapes up like ridges, which will eventually

dissolve into the bulk solution or form currents of higher salinity within the bulk solution. Thus, in later stages of the convection instability KHI rather than RTI may be the dominant natural convection instability.

As a result of the more complex hydrodynamics, the bulk solution is no longer uniform, which effects the RM measurement. Some volumes are of higher salinity than others and those volumes stack on top of each other to form confined currents. This is most clearly seen in Fig. 3.6 B at the center contour plot. This effects the RM measurement since the refraction index changes with salinity (Table 3.2). Confined volumes of different refraction index stacked on top of one another introduce additional refraction interfaces. This results in loss of signal intensity, which the calibration data set does not account for. This means, that values after the first local concentration maxima along the optical axis are undervalued. This explains, why concentrations below the feed concentration are measured in Fig. 3.6 (also later in Fig. 3.8). It is not clear how severely this affects the quantitative measurement. However, considering that the change in refraction index is small (less than 0.2%) and the measurements at x = 81.5 and x = 86.4 in Fig. 3.6 A show an expected concentration increase at the membrane surface (new buildup of CPL), it is reasonable to assume that the measurement is not affected in its qualitative value. Therefore, the decrease in concentration in these profiles from z = 350 to z = 160 is unlikely to be a measurement artifact.

3.2.2 RM Measurements with Feed Spacer

The purpose of feed spacers in spiral wound modules is to firstly, keep membrane sheets apart and secondly, to improve filtration performance. Therefore, feed spacers are always present in membrane elements. The fact, that RM allows to measure the CPL with the presence of feed spacers is, thus, a large advantage of the technique. A feed spacer changes the flow field inside the feed channel and improves mass transfer and mixing. As a result, neither the CPL nor the bulk solution remains uniform and becomes fractionated into local areas of high and low concentration as well as higher and lower cross-flow velocity. Previous modeling of the fluid dynamics in spacer-filled feed channels has shown that the flow field is similar in each spacer element (Picioreanu et al. 2009, Shakaib et al. 2009). The measurement result of one spacer element should, thus, be qualitatively representative for all spacer elements not affected by additional boundary effects at the feed channel walls.

Fig. 3.8 shows the RM measurement of a filtration experiment with feed spacer, feed sulfate concentration of 10 $g \cdot L^{-1}$ and cross-flow velocity of 0.04 $m \cdot s^{-1}$. Depicted is one spacer element in the center of the feed channel at x = 82.4 to 86.0 mm. The spacer filaments are shown in

grey. Spacer filaments are about 2.7 mm in length and vary in diameter from 350 to 500 µm. Total thickness at the nodes is about 700 µm (28 mil). Spacer filaments are stacked on top of one another with opposite filaments being at the same height. The top left and bottom right filament are in contact with the flow cell window, whereas the bottom left and top right filaments are in contact with the membrane. Each 2D plot shows the distribution of the sulfate concentration at a specific depth with the membrane surface located at z = 0 µm. In the RM measurement, a signal intensity below 8.5 g·L^{-1} was defined as spacer.

The three plots show a similar concentration pattern. The highest concentration is measured in direct vicinity of the spacer filaments in contact with the membrane. However, apart from these areas of high concentration, concentration is measured to be below the feed concentration. This is, most likely, again a result of a layer of increased concentration obstructing the illumination pathway. The additional refraction occurring, results in loss of signal intensity, thus undervaluing true concentration. This means, that the RM measurement cannot quantitively measure the true concentration near the membrane surface. However, qualitatively, it shows how the concentration is distributed within the spacer element.

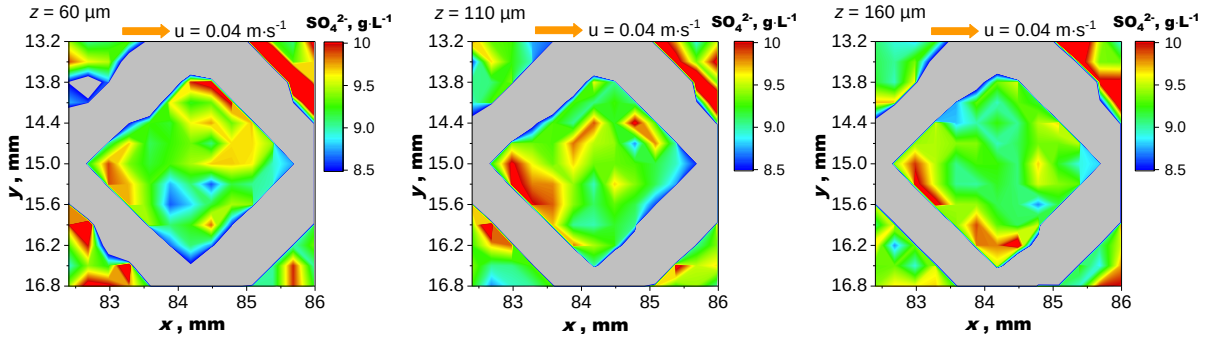

Fig. 3.8 2D cross-sections of 3D measurement with feed spacer. Filtration conditions: c_{feed} = 10 g·L^{-1}, u = 0.04 m·s^{-1}. *Resolution: z, 10 µm; y, 300 µm; x, 300 µm*

With increased recovery and lower cross-flow velocity, the RM measurement shows a more distinct pattern inside the spacer element. The cross-flow velocity was reduced tenfold to 0.004 m·s^{-1}, which increases recovery from 6.5 to 31%. Fig. 3.9 A - C shows the same 2D cross-sections as in Fig. 3.8. However, with the increase in concentration gradients, the concentration pattern is shown more clearly. Within z = 0 to 160 µm, the spacer element can be divided into two halves, separating at the center line (y = 15.0 mm). In the top half (y < 15 mm), concentration increases gradually towards the membrane and in direction of cross-flow. In the bottom half (y > 15 mm), maximum concentration is measured at z = 110 µm in the center of the spacer element (y = 15.0 to 15.6 mm) as well as near the bottom left spacer filament. Towards the bottom right spacer element sulfate concentration decreases to near

feed concentration. A similar pattern can be seen in Picioreanu et al. (2009) Fig.2H, which shows a CFD simulation of the velocity distribution inside a spacer filled channel of similar dimension about 80 µm above the membrane surface. According to their results, maximum velocity appears at the spacer filaments away from the membrane and stretches into the center of the spacer element. Minimum velocity appears at the spacer filaments in contact with the membrane and also stretches into the center of the spacer element. Thus, the spacer element is divided into two halves with high velocity in one and low velocity in the other. The resulting pattern is clearly similar to the one shown in Fig. 3.9. Cross-flow velocity was much greater in the simulation, yet the RM measurement shows that a flow field comparable to the simulation develops within the spacer element. Furthermore, the concentration distribution should be inverse to velocity. Since the spacer orientation in the simulation is the same as in this study, both graphs can be directly compared. The comparison of the two graphs shows that, indeed, the concentration distribution with the RM measurement is inverse to the velocity distribution in the simulation.

The divide in the center of the spacer element is further illustrated with the concentration profiles and the 3D cutout of the center area shown in Fig. 3.9 D and E. At y = 14.7 mm, the graph shows a gradually increasing concentration profile towards the membrane surface suggesting low cross-flow velocity. At y = 15.3 mm the concentration is about constant suggesting high cross-flow velocity, preventing the formation of a larger CPL near the membrane surface. At the center, y = 15.0 mm, the concentration profile follows a U-shape, suggesting bulk solution to enter and dilute the center volume as well as low cross-flow velocity, which favors the formation of a CPL. The 3D image provides a good perceptional overview of the concentration distribution at the center of the spacer element. It shows the division in the center clearly as well as the concentration increase towards the membrane.

A comparison of the filtration performance with the opposite membrane configuration (BOTTOM) reveals little difference. Recovery is decreased from 31 to 28% and rejection decreases from 96.9 to 96.5%. This suggests little influence of natural convection. The disruption of the flow field due to the feed spacer appears to prevent the local formation of convection cells. Without the influence of natural convection, the measured concentration pattern should be representative for higher cross-flow velocity as well.

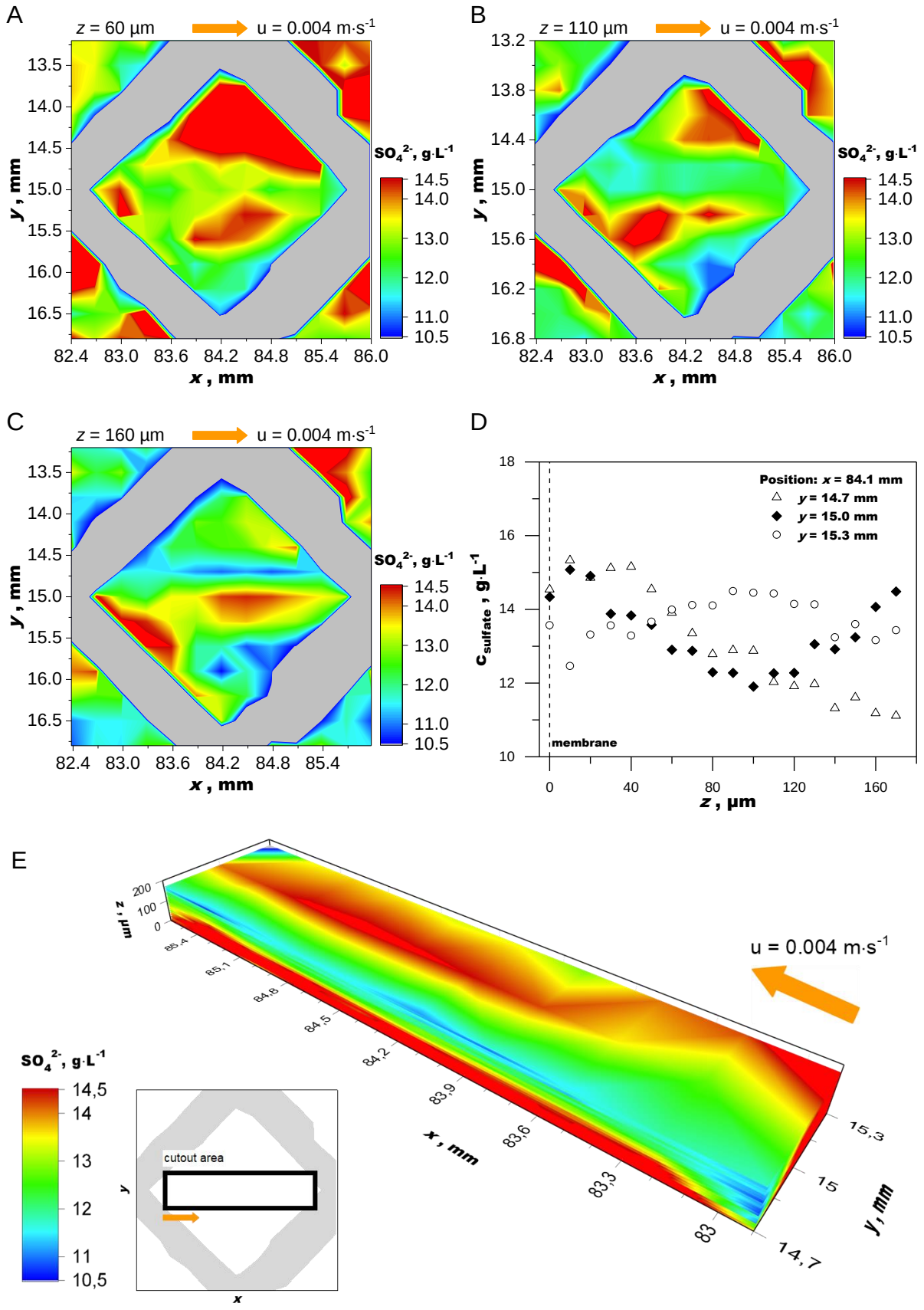

Fig. 3.9 3D measurement with feed spacer. Filtration conditions: c_{feed} = 10 g·L^{-1}, u = 0.004 m·s^{-1}. A-C: 2D cross-sections, D: 1D measurements in the center of spacer element. E: 3D

cutout of the channel along the center of the feed spacer element. *Resolution: z, 10 µm; y, 300 µm; x, 300 µm*

3.3 Conclusion

In this chapter the innovative approach of RM for the measurement of CP in membrane feed channels presented in chapter 2, has been applied to investigate a variety of filtration conditions. It was shown that the measurement results are in good qualitative agreement with the known theory about CP. The measured profiles without a feed spacer and at laminar conditions show an increase in CPL thickness and membrane surface concentration (CPF) consistent with increased recovery. Reducing cross-flow velocity to the magnitude of $mm \cdot s^{-1}$, revealed an influence of membrane orientation. With the membrane positioned on top of the feed channel, as is required with an inverted RM setup, recovery and rejection were substantially improved. The RM measurements were able to show that the CPL was no longer uniform across the membrane area and that mass transport is improved due to natural convection. The inverted configuration is inherently unstable since density increases due to CP and the lighter bulk solution pushes the heavier solution above at the membrane surface. This is the defining condition for the occurrence of Rayleigh-Taylor-Instability (RTI), making this the first study to measure RTI in a NF system. High resolution RM measurements could show the development and dimension of “spikes” and “bubbles” typical for RTI during the initial development of the disturbance. Due to the present cross-flow velocity, “spikes” were prolongated along the feed channel to form “ridges”, which eventually dissolve into the bulk solution or form currents of higher salinity. The width of these “ridges” was measured to be about 100 µm and the wavelength of the instability was measured to be about 700 µm. It was proposed that due to the cross-flow operation Kelvin-Helmholtz-Instability (KHI) may also be important for the description of the hydrodynamic conditions. Making use of the two sampling modes, it was shown that the RTI convection patterns were stable locally and over time. At higher cross-flow velocities the influence of natural convection appears to be masked by forced convection. This study supports the boundary condition for natural convection to be influential, which was proposed by Youm et al. (1996).

RM was used to measure the concentration distribution inside a spacer-filled membrane feed channel *in-situ*, which has not been done before in published literature. The measurement suffered with loss in signal intensity due to the more complex flow field created by the spacer, which leads to changes in refractive power within the feed channel. The calibration methodology does not account for those additional refractive volumes. However, qualitatively, the concentration distribution could be resolved and it was shown that the measured

concentration pattern is in agreement with simulations of velocity distribution in published literature. Thus, RM can also be applied at conditions of complex fluid dynamics for qualitative purposes.

Although it is outside the scope of this work to challenge the acquired results with a modeling approach, the value of contrasting these results with sophisticated models of mass transport is recognized. Modeling the experimental results presented in this chapter would help, especially, with gaining more inside into the accuracy of the absolute concentration values obtained with the RM measurement. Comparing the measured data with simulation results may help with the development of another method of correcting for the loss in signal intensity due to changes in refractive power within the feed channel volume. It is very important that any modeling approach recognizes the special characteristics of this study, particularly paying attention to the physical properties of pure magnesium sulfate solution of higher concentration. If done properly, combining the experimental results of this study with a modeling approach would certainly add great value to this research.

4 Raman Microspectroscopy for the Study of Combined Membrane Fouling

Introduction

Membrane technology has developed into a leading process for water treatment (Hamingerova et al. 2015). Currently, process efficiency is increasing and new areas of application are being explored. Accompanying the spread of membrane processes are biofilms for which membranes offer excellent cultivation conditions. In most common membrane water treatment processes however, the formation of biofilm on membrane surfaces is undesired and referred to as biofouling. The mitigation of biofouling is challenging, complex and limited. Biofouling can be retarded rather than avoided. This makes biofouling one of the major fouling problems that operators of membrane systems for water treatment are currently faced with. Thus, improvements in understanding how biofilm affects membrane filtration performance is valuable (Bucs et al. 2018). The presence of biofilm on a membrane in reverse osmosis membrane systems degrades operational performance. Among others, this is generally caused by: (i) increase of feed channel pressure drop, (ii) change of feed channel flow dynamics, (iii) enzymatic membrane degradation, (iv) facilitation of other fouling phenomena (e.g. scaling) and, most importantly, (v) increase of transmembrane solute passage as well as (vi) increase of transmembrane pressure (TMP) (Flemming 1997).

In nanofiltration (NF) and reverse osmosis (RO) an increase in TMP and solute passage due to biofilm is primarily caused by its influence on the phenomenon of concentration polarization (CP). The presence of biofilm on the membrane surface leads to an increased membrane wall concentration of the solutes, which means that biofilms clearly affect the concentration polarization layer (CPL) (Chong et al. 2008, Herzberg and Elimelech 2007). The CPL in NF/RO is not easily accessible experimentally, hence, focus has been on describing the phenomenon theoretically using numerical simulations. Furthermore, research into membrane fouling often focuses on one type of fouling at a time, e.g. scaling (Benecke et al. 2018, Shirazi et al. 2010), biofouling (Herzberg and Elimelech 2007) or organic fouling (Lee et al. 2006). However, membrane autopsies and studies investigating membrane fouling in practical applications have consistently shown the presence of more than one fouling type and also that mitigation strategies for one type can facilitate another, e.g. antiscalants facilitating biofouling (Antony et al. 2011, Darton et al. 2004, Dudley and Darton 1996, Vrouwenvelder and van der Kooij 2001, Xu et al. 2010). Therefore, future research should put greater emphasis on combined fouling and on the mechanisms by which one type of fouling affects another (Bucs et al. 2018, Thompson et al. 2012). For example, biofouling is linked to scaling by affecting mass transport

inside the membrane feed channel. Radu et al. (2015) have investigated this connection by developing a novel modeling approach for combined biofouling and scaling (Radu et al. 2015). The present work is the first study attempting to measure the influence of biofouling on salt concentration near the membrane surface on a micro-scale using Raman microspectroscopy (RM).

RM as well as surface-enhanced Raman spectroscopy (SERS) already occupy a place in the description of biofouling in membrane processes. These techniques have previously been demonstrated to be viable tools for the characterization and monitoring of biofilms and biofilm formation (Ivleva et al. 2017, Lamsal et al. 2012, Virtanen et al. 2017). This study is based on the experimental technique developed in chapter 2. The Raman activity of sulfate is utilized to measure the signal intensity distribution within the membrane feed channel with and without the presence of biofilm of varying thickness.

Biofouling

Biofouling is a special kind of fouling as it is the only kind of fouling that involves living organisms. Rather than the microorganisms themselves, it is their metabolic activity, which eventually leads to problems in technical systems. Microorganisms can feed on a wide variety of nutrients, which in a membrane system are usually present as dissolved or suspended organic material in the water phase. Yet, depending on the material, microorganism can also attack and degrade functional plant components such as cellulose acetate membranes and glue lines (Flemming 1997). What makes the presence of microorganisms either particularly problematic or particularly symbiotic for membrane systems is their ability to attach to surfaces and form biofilms. A biofilm is typically 95 to 99% water and made from polysaccharides (extracellular polymeric substances, EPS) produced by the organisms themselves, forming a stable EPS-matrix (Flemming 2020, Flemming and Wingender 2010).

A biofilm is an adaptation for survival. It secures fixation of nutrients and provides shelter from stress factors such as toxic chemicals and physical forces, e.g. shear force. These properties are desirable in bioreactors utilized in waste water treatment and water purification but are undesirable in applications such as RO and NF for high quality water purification. In those applications, biofilm formation eventually leads to loss in filtration performance at which point it is referred to as biofouling (Flemming 1997). Of all forms of membrane fouling, biofouling is also special in its ubiquity, being recognized “as at least a contributing factor to more than 45% of all membrane fouling” (Komlenic 2010). Membrane systems are always susceptible to colonization of microorganisms since sterility is not a practical option, nutrients are always

available and colonies can form from low initial numbers of cells even at very low nutrient concentration (microgram per liter level) (Bucs et al. 2018, Flemming 1997).

Thus, biofouling is not a sudden event but rather a gradual development over the operational time of membrane systems and its installed membranes. It can be present in all systems independent of pre-treatment and there is no typical fouling organism to be identified and eliminated (Flemming 2002). As a result, biofouling has been affecting RO and NF applications since their introduction and, despite extensive efforts, research into mitigation of biofouling has only brought about incremental improvements, prompting calls to approach this issue anew, from the start, looking for new solutions (Komlenic 2010).

However, biofouling may not be a problem to be solved but rather one to manage intelligently. In the end, life tends to find ways (Flemming 2020). In the same spirit, Bucs et al. (2018) state that biofouling control strategies should focus foremost on delay of biofilm formation, advanced cleaning strategies and reducing its impact on membrane performance. When viewing biofouling as an unavoidable problem of biofilm formation, then focus can pivot from common control strategies like inactivation of microorganisms (dosing of disinfectants/biocides) and removal of biomass (extensive pre-treatment) towards understanding the interactions of biofilms with membrane performance and how to influence them.

Once a biofilm has been established on a membrane surface, it influences and changes properties governing the filtration process in multiple ways. Fluid dynamics are changed locally and within the membrane element with additional pressure loss across the membrane and along the membrane channel. Surface properties of the membrane may be altered or masked, diffusion of solutes may be hindered and advective flows altered. Biofilm geometrical properties, mechanical characteristics and hydraulic properties should all be influential and may be tailored towards beneficial outcomes(Bucs et al. 2018). At this point, experimental techniques to characterize biofilms in combination with techniques measuring the biofilms effect on mass transport or the interaction of the EPS-matrix with feed water compounds, becomes a promising prospect for future research.

4.1 Materials & Methods

This study introduces optical coherence tomography (OCT) to the Raman-Membrane-Setup. OCT is an interferometric imaging technique herein used to provide imaging data of the mesoscopic structures of the organic fouling layer (biofilm) on the membrane surface. A

Thorlabs GANYMEDE II SD-OCT system from Thorlabs GmbH, Lübeck, Germany, was used. This system has an axial resolution (r_z) of about 6 µm in air and a lateral resolution of about 8 µm. The system is equipped with a super luminescence diode (SLD) with a central wavelength of 930 nm as a light source with low coherence. The measurement principle uses the principle of a Michelson-interferometer to record and analyze the echo time delay of backscattered light. The source light is split into a reference arm and a sample arm. The sample arm focuses the incoming light through a lens into the sample, i.e. the biofouling layer. At the sample, light is reflected and scattered, causing a phase shift (echo with a time delay). When recombined with the light from the reference arm, an interference pattern occurs. After digital processing of the signal, a 1D intensity distribution along the optical axis (*z*), called an A-Scan, is recorded. Repeated scanning along the lateral axis (*x*) gives a 2D z-x-image of the sample, termed a B-Scan. Further sampling along the *y*-axis gives a 3D image, termed a C-Scan. A comprehensive description is given in Fujimoto and Drexler (2008) and the terminology follows Wagner and Horn (2017).

In this study, C-Scans are recorded and processed to evaluate the thickness of the fouling layer/biofilm on the membrane surface. Image post-processing was done using Fiji (Schindelin et al. 2012). For analysis, C-Scans of the dimension 0.5×0.5×1 mm³ (*x*-*y*-*z*) were recorded. A greater area was sampled for manual optical evaluation of fouling layer structures and morphology. Post-processing consists of smoothing and adjustment of brightness and contrast. For evaluation of biofilm thickness, several subroutines are used following the procedure outlined in Wagner et.al. (2010). The effect of these post-processing steps is shown in Fig. 4.1. The first subroutine locates the membrane surface by searching for the brightest signals for each axial line and setting them to white (Fig. 4.1 b). With the next subroutine, all image data below the white line is cut, thus, establishing the membrane surface as new baseline (Fig. 4.1 c). This also straightens the membrane and corrects for tilt. The next step is to convert the image into a binary. This is done by setting contrast to 100% and adjusting brightness until artifacts in the bulk are eliminated (Fig. 4.1 d). The last subroutine measures biofilm thickness. For each axial line, the number of white pixels is determined. The number of pixels can be converted to length using the pixel resolution. Pixel resolution is a known property and dependent on refractive index. Setting the refractive index to that of water, n = 1.3, gives a pixel ratio of 2.12 $\mu m \cdot px^{-1}$. Thus, biofilm thickness (L_F) is herein defined as the height over membrane surface with exclusion of voids.

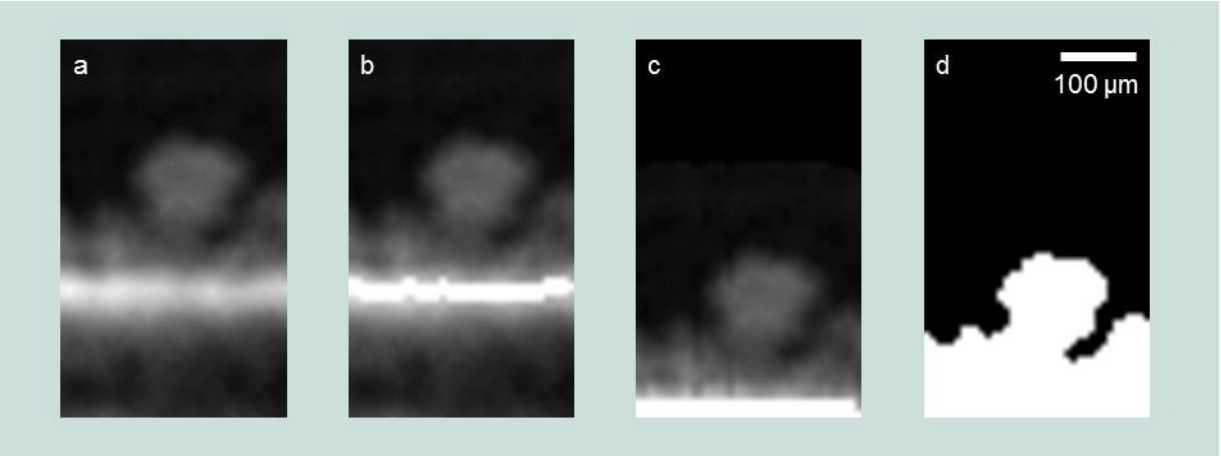

Fig. 4.1 OCT image post processing: a: contrast enhanced, smoothened; b: membrane surface located and set to white; c: straighten and set membrane surface to baseline; d: binary image

Figure 4.2 shows a scheme of the measurement setup used to investigate the effect of biofouling on the CPL of sulfate. The core setup is the same as presented previously employing a flow cell equipped with the DOW FILMTEC™ NF270 nanofiltration membrane. Permeate and concentrate streams are recirculated into the feed. Additional equipment is added to grow biofilm on the membrane. Each experimental run follows four steps.

(1) Formation of biofilm to cover the membrane surface.
(2) Replacement of growth medium with pure magnesium sulfate solution.
(3) Calibration series.
(4) Measurement series.

During biofilm formation, the feed container is filled with autoclaved growth medium (composition listed in Table 4.1), which is continuously replenished from reservoir 1 using a peristaltic pump. The feed container is equipped with an overflow to waste in order to remove suspended biomass and promote biofilm formation. Air is pumped into the feed container to saturate the solution with oxygen for aerobe growth conditions. At the start of the experiment, the feed container is inoculated with a fresh, single colony of *Bacillus subtilis*. The culture was pre-grown on a Luria-Broth (LB-)-agar-plate, suspended in 20 mL LB-medium, shaken and tempered at 37 °C for six hours.

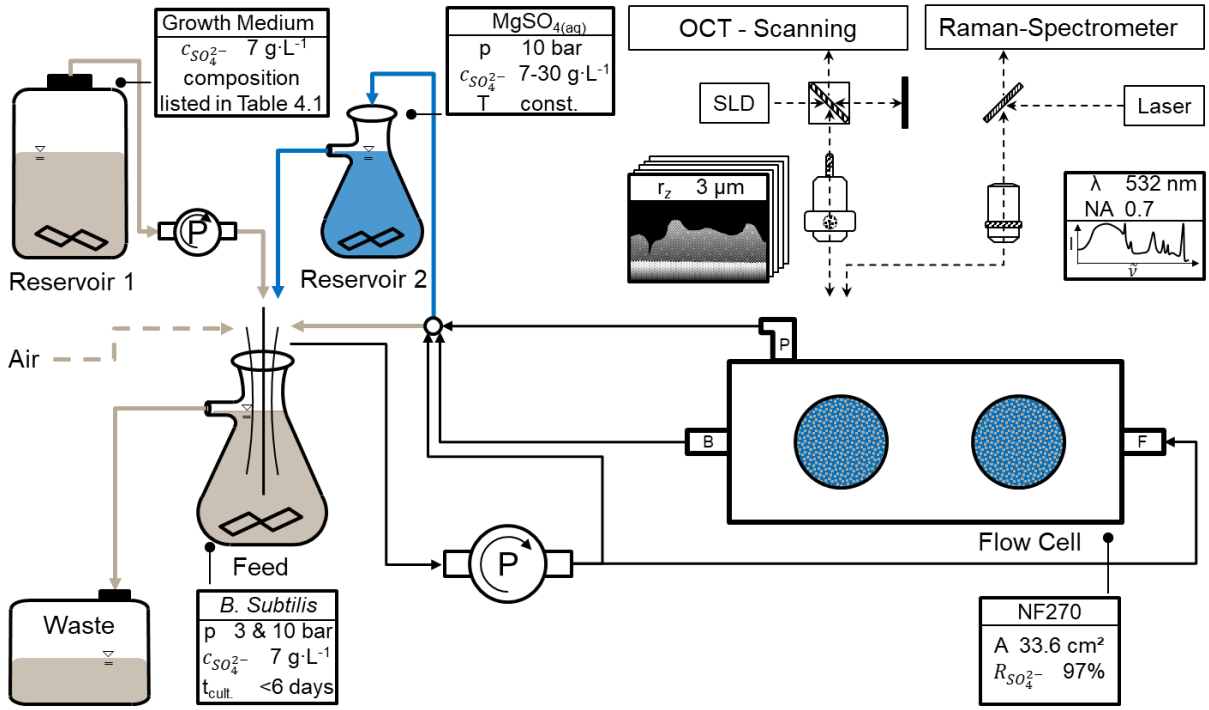

Fig. 4.2 Scheme of the experimental setup for measurement of sulfate concentration gradients after subjecting the membrane to enhanced biofouling conditions. Brown arrows: circulation of growth medium inoculated with *Bacillus subtilis* for up to six days; Blue arrows: replacement of growth medium with pure magnesium sulfate solution for measurement with Raman microspectroscopy (RM). Optical coherence tomography (OCT) used for biofilm characterization and monitoring during growth.

The flow cell is pressurized with an alternating pressure regimen, which repeats every 48 hours. For the first 16 h, 10 bar pressure is applied. For the next 8 h, pressure is alternated every 2 h between 3 and 10 bar, followed by 16 h of 3 bar and 8 h of alternating between 3 and 10 bar again. This regimen was adopted to grow a stable biofouling/biofilm layer, which means that no detachment in the later phases of the experiment occurs. Furthermore, pressurized growth promotes biofilm formation on the membrane surface instead of other surfaces, i.e. cell windows, which is critical. At 3 bar system pressure, permeate flux is minimal but still greater zero. This was done as a safety buffer against back diffusion, which can occur when system pressure falls below osmotic pressure. During the growth phase, cross-flow velocity was kept in range of 0.04 to 0.08 m·s^{-1}.

OCT is utilized to monitor the growth of the fouling layer and determine its thickness. Once a desired thickness is reached, the growth phase is terminated by replacing the feed solution with pure magnesium sulfate solution of equal sulfate concentration, which comprises step 2. Reservoir 1, the air pump and waste are disconnected and reservoir 2 is connected. Using

the additional reservoir containers allows for flushing and replacement of solution without shutting down the main pump and keep pressure and cross-flow conditions within range. System pressure must never fall below feed osmotic pressure or back diffusion with possible fouling layer detachment may result.

Table 4.1 Composition of solution for enhanced biofouling regimen (bacterial growth medium)

Chemicals (supplier), analytical grade	Quantity, $g \cdot L^{-1}$
$CaCl_2 \cdot 2\ H_2O$ (VWR)	0.11
$MgCl_2 \cdot 6\ H_2O$ (Roth)	0.41
Glycerol (Roth)	5
Tryptophan (Roth)	$5 \cdot 10^{-3}$
Phenylalanine (Merck)	$5 \cdot 10^{-3}$
$ZnCl_2$ (Roth)	$0.136 \cdot 10^{-3}$
Thiamin hydrochloride (SIGMA)	$0.674 \cdot 10^{-3}$
$MnCl_2 \cdot 4\ H_2O$ (Merck)	$9.89 \cdot 10^{-3}$
$FeCl_3 \cdot 6\ H_2O$ (Merck)	$13.52 \cdot 10^{-3}$
$MgSO_4 \cdot 7\ H_2O$ (Roth)	17.96
Buffer solution, 0.5 M ($Na_2HPO_4 \cdot 2\ H_2O$ (AppliChem) & KH_2PO_4 (Merck))	1
NaOH, 5 M	pH 7
DI water	

The third step, calibration, is similar to the method described in the previous studies (Chapter 2 and 3). The only difference is that system pressure is fitted to osmotic pressure. This is necessary to prevent back diffusion and still record the Raman response of the sulfate signal with no permeate flux and thus, no CPL present.

The final step is the measurement series applying 10 bar with a fixed cross-flow velocity of 0.04 $m \cdot s^{-1}$. Feed sulfate concentrations were fixed to 10 and 20 $g \cdot L^{-1}$. Measurements were taken at window 2 only, about 8.5 cm from the inlet and at the center of the feed channel. The Raman response of the biofouled membrane does not differ to the clean membrane response in the relevant spectral range except for signal intensity, which is lower. This means, that the biofilm does not introduce interfering Raman bands. Hence, the same Raman bands and the same routine can be used for evaluating clean and biofouled Raman signal. With the biofouling layer present, Raman illumination time was doubled to total 60 s by doubling the integration

time to 10s and keep co-additions at 6. Laser power output was kept at 50 mW. The raw Raman spectrum output at the surface of the biofouled membrane is shown in Appendix Fig.A2.

OCT was applied jointly with Raman measurements to determine the fouling layer thickness at the same point of measurement and at the same operating conditions. The membrane was prepped with three black markings prior to installation, shown in Fig. 4.3. With the distance of the area scanned with OCT to the black dots known, the area could be located with the Raman microscope.

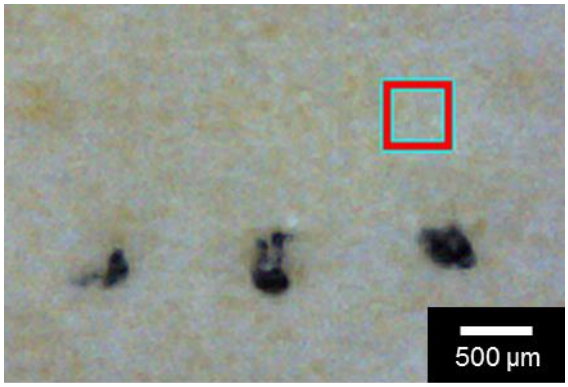

Fig. 4.3 Membrane with biofilm and markings for localization (OCT microscope picture). The red square marks the area of interest for OCT scanning and RM measurements. The distance to the black markings is used to localize the area for Raman measurements.

4.2 Results & Discussion

4.2.1 Biofilm Characteristics

OCT is particularly suitable for combination with the herein presented Raman microspectroscopy analysis. The method is *in-situ*, non-invasive, allows for three-dimensional observation of the biofilm over a large area and over time. The biofilm can be analyzed precisely at the area or point of measurement without staining or altering of biofilm properties. Image acquisition is very fast (seconds) to the point that time requirements are mainly dependent on the ease of the setup to switch between OCT and RM. OCT has been shown to yield a number of biofilm properties related to its morphology, structure and mechanical behavior, e.g. volume, roughness, porosity, shear modulus and Young's modulus (Blauert et al. 2015, Gierl et al. 2020, Picioreanu et al. 2018, Wagner and Horn 2017). For the purpose of this study, OCT is mainly used to determine biofilm thickness at the point/area of

measurement. Thickness is determined as mean thickness from OCT C-Scans obtained during biofilm growth and during membrane filtration operation at variable operating conditions.

Apart from biofilm thickness and compressibility, OCT provides a visual representation of biofilm morphology. The study bacteria, *Bacillus subtilis* is a Gram-positive soil bacterium, which is widely used as a model bacterium for investigation of biofilm formation. It can grow in terrestrial and aquatic environments. Although mainly aerobe, *B. subtilis* has been shown growing anaerobically using nitrate as oxidant (Earl et al. 2008). The biofilm of *B. subtilis* is reported to be “robust, highly ordered and stable” and to exhibit hydrophobic properties (Arnaouteli et al. 2016, Epstein et al. 2011). Furthermore, Wilking et al. (2013) describe the formation of interconnected flow channels to facilitate nutrient transport in *B. subtilis* biofilm.

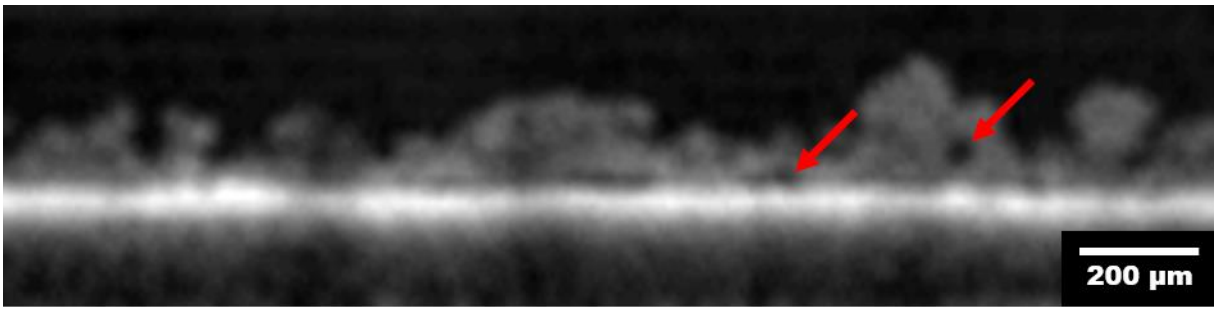

Fig. 4.4 OCT image of *B. subtilis* biofilm grown over 6 days showing morphology. The red arrows point to voids believed to be interconnected flow channels.

The biofilm was grown following an alternating pressure regimen as described in section 4.1. During pressurized operation, permeate flux is induced and suspended cells are deposited on the membrane. Cell accumulation is aided by convective permeate flow and, as we have seen in earlier experiments, the formation of a cake layer is promoted. This type of fouling layer was found to be unstable, meaning that it quickly detaches from the membrane surface once permeate flux is stopped by lowering system pressure to be equal to osmotic pressure. Letting biofouling commence without permeate flux, cell adhesion via biofilm formation is promoted. However, in this case, biofilm formation is facilitated over all surfaces of the flow cell, including the glass window causing measurement interference. Furthermore, the biofilm is fluffy, exhibits streamers and shows a very high compressibility. This type of biofilm should not be representative of biofilm seen in practical membrane filtration applications. The alternating pressure regimen compromises between promoting biofilm formation and cake layer deposition. This results in a denser biofilm not exhibiting streamers and which is stable under all pressure conditions used in the study.

Fig. 4.4 shows an OCT picture of *B. subtilis* biofilm after six days of growth. The setup is not optimized for OCT imaging (e.g. window material), which shows in a substantial amount of background brightness diminishing contrast. The original OCT picture is shown in Appendix Fig.A3. However, after manipulation of brightness, contrast and smoothing, suitable images for analysis are created. The membrane yields the brightest signal, which distinctly defines the membrane surface in the picture. The biofilm is seen on top of the membrane. Biofilm growth is uneven, exhibiting some mushroom-like structures, which are a normal occurrence with biofilms. Thickness analysis of the displayed area gives a mean thickness of 127 µm with a maximum of 246 µm, minimum of 56 µm and standard deviation of 46 µm. Black spots in the picture are believed to be voids in the biofilm matrix, which may represent interconnected flow channels as Wilking et al. (2013) reported.

The study of Biofilm properties and characteristics as well as metabolic considerations are not a focus of this study. Biofilm was grown solely for the purpose of establishing a biofouling layer of specific thickness on the membrane to investigate the potential of RM for the study of the combined effects of biofilm and concentration polarization. Nevertheless, the study presents some interesting findings of mechanical biofilm characteristics, which shall be discussed. Furthermore, morphology and biofilm behavior under varying pressure have a profound impact on the Raman methodology and interpretation of the Raman results.

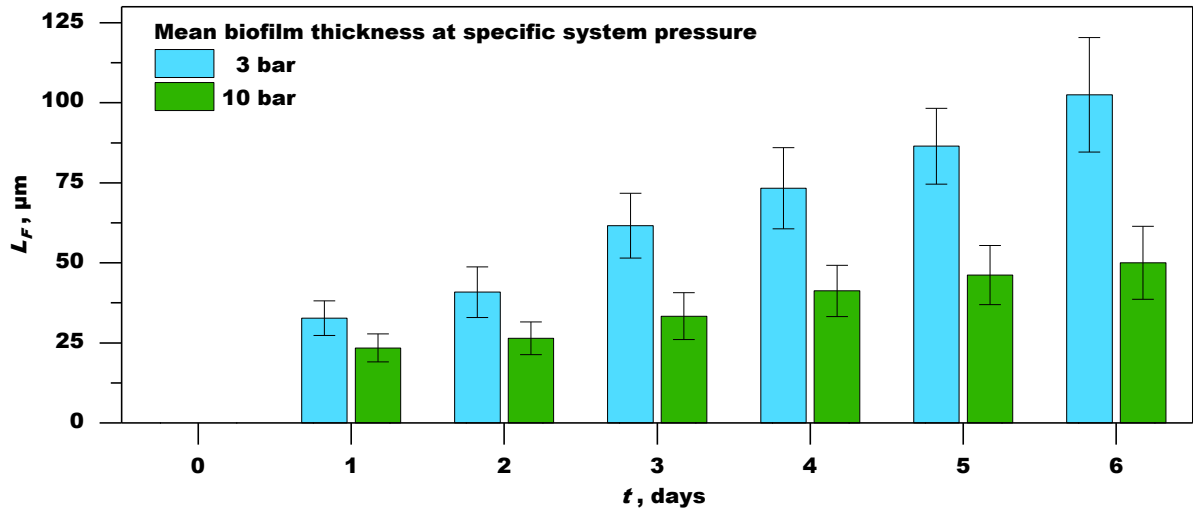

Fig. 4.5. Development of mean biofilm thickness over a growth period of six days with an alternating pressure regimen (see section 4.1), 7 g·L^{-1} sulfate, 0.1 m·s^{-1} cross-flow velocity. Each day represents a compression experiment, where the data was recorded 5 min before and after the system pressure change.

Fig. 4.5 shows the biofilm growth over a period of six days. Mean biofilm thickness increased throughout, showing accumulation of biomass each day with no apparent detachment event. Biofilm growth appears steady rather than exponential as would be expected from principal considerations or as shown in similar experiments (Dreszer et al. 2014, Flemming 1997). Biofilm growth does not show a plateau phase at the end of six days. This suggests that the biofilm is still likely at an early stage of development and a maximum biofilm thickness is not yet reached. The experiment was terminated after day 6 as the objective of the experiment was to obtain a biofilm of about 100 µm in thickness for the Raman study rather than a complete description of biofilm growth.

Each day represents a compression experiment with the data acquired before and right after the system pressure was changed. The data shows how the biofilm is compressed upon increasing the system pressure. At 10 bar pressure, permeate is produced with an effective pressure of about 7.2 bar. At 3 bar, no measurable permeate flux occurs. Cross flow velocity is kept constant throughout the growth of the biofilm in order to not subject the biofilm to increased shear forces. Fig. 4.6 shows the compressibility as the amount of shrinkage normalized to the original thickness before the high pressure event. Compressibility increases through the first three days but appears to be reaching a maximum at 45-50%.

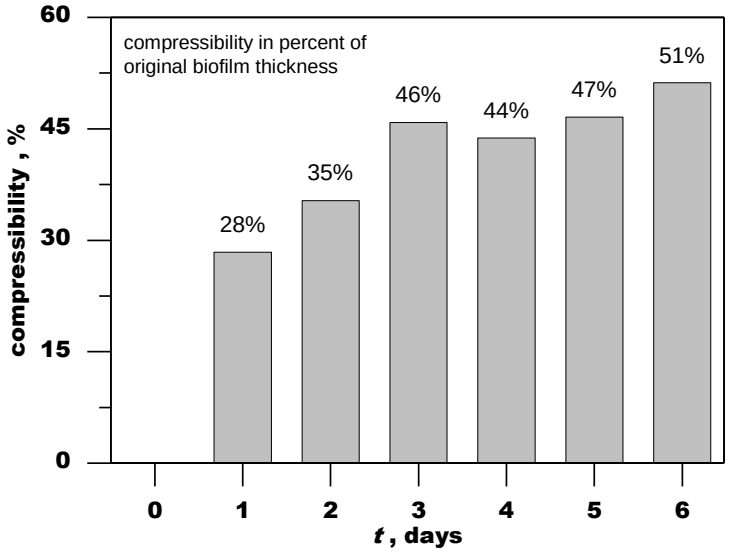

Fig. 4.6 Compressibility of the biofilm after changing system pressure from 3 bar (effective pressure about 0 bar) to 10 bar (effective pressure about 7 bar)

Accompanying the accumulation of biomass on the membrane surface is a decrease in permeate flux and an increase in permeate conductivity. This is to be expected and well documented in literature (Dreszer et al. 2013, Flemming 1997, Herzberg and Elimelech 2007).

Fig. 4.7 shows permeate flux and permeate conductivity over five days of enhanced biofouling at 10 bar system pressure. For reference, day 0 shows permeate flux and conductivity for the clean membrane and with a pure salt solution without organics. The addition of organics and chloride salts as part of the growth medium has a large impact on salt passage for the nanofiltration membrane. The NF270 rejection towards chloride is low. Although all cations are multivalent, due to the Donnan effect, increased permeation of multivalent ions is to be expected. The effect of biofouling on membrane performance is profound. During biofilm growth and accumulation of biomass on the membrane from day 1 to day 5, permeate flux has decreased by 75% from 18.8 to 4.6 $L \cdot m^{-2} \cdot h^{-1}$, whilst permeate conductivity has increased by 47% from 1.1 to 1.6 $mS \cdot cm^{-1}$. This data is not quantitively connected to the biofilm data obtained from Fig. 4.5 as both experiments were conducted at different operating conditions. Permeability data was obtained with higher salt concentration in the feed and at constant system pressure throughout.

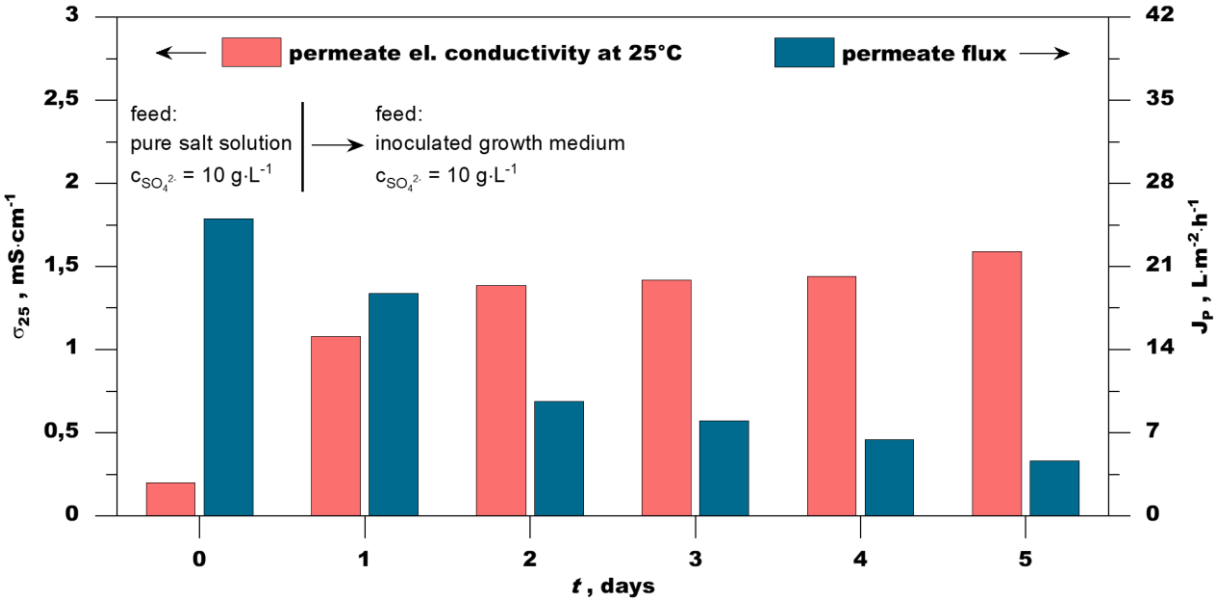

Fig. 4.7 Permeate flux and permeate conductivity in enhanced biofouling conditions with feed sulfate concentration of 10 $g \cdot L^{-1}$. System pressure = 10 bar.

Nevertheless, the data is connected qualitatively. The results show that the biofilm responds to changes in permeate flux with compression and relaxation as well as that permeate flux is decreasing with biofilm formation. When osmotic pressure is adjusted by changing the salt content of the feed solution to match the system pressure, biofilm thickness is unaffected. Compression was only observed in connection with increased permeate flux, indicating a purely kinetic (physical) effect, rather than an osmotic effect, i.e. variations in the water volume of cells. Permeate flux is correlated to permeation velocity. It appears that a force equilibrium

between the kinetic force of the water flow (velocity) and the elastic force of the EPS matrix is established under filtration conditions. This connects biofilm characteristics such as the Young's modulus to permeate flux. Thus, membrane filtration experiments with OCT may be a viable experimental strategy to determine mechanical biofilm characteristics.

Considering further the decrease in permeate flux with increasing biofilm thickness, it follows that compressibility as shown in Fig. 4.6 should reach a maximum before decreasing. With less permeate flux, less compressing force is put on the biofilm matrix. However, the data does not show a reduction in compressibility but rather a stabilization along with the stabilization of permeate flux. If less force leads to higher compression (absolute), than biofilm density may be decreasing with further biofilm development. In a prior experiment biofilm was grown at atmospheric pressure (no permeate flux). Compressibility of that biofilm was measured to be 80%, supporting the assumption that permeate flux increases biofilm density. Hence, as permeate flux is decreasing with biofilm development, biofilm density may decrease as well. From these results it follows, that biofilms developing in practical pressure driven RO/NF membrane systems should exhibit higher density and lower elasticity than biofilms cultivated with no permeation of water flux through the biofilm matrix.

Compressibility of biofilm in membrane filtration experiments has also been observed by Dreszer et al. (2014). The authors have related compressibility to compaction by observing that a compressed biofilm provides an increased hydraulic resistance to permeation. The authors remark, that the biofilm properties were not reversible and that after an event of compaction, biofilm resistance remained elevated and biofilm thickness was not fully restored. Thus, their experiments show that biofilm thickness is but one variable to describe hydraulic permeability and other structural properties may be more important.

In this study, biofilm thickness was completely reversible, which may be attributed to the fact that the biofilm was subjected to the highest permeate flux and feed pressure during its growth period, instead of after. Therefore, it might be more appropriate to, in this study, consider the variation of biofilm thickness with TMP as relaxation events rather than referring to them as compression.

4.2.2 RM Measurements

Four biofilms of varying thickness were successfully cultivated to meet RM measurement criteria. RM calibrations and measurements were done at the same position and with the same

operating conditions as prior measurements with clean membranes to permit a direct comparison. Fig. 4.8 shows the recorded depth profiles for feed sulfate concentrations of 10 and 20 $g \cdot L^{-1}$ (effective pressure of 7.2 and 4.4. bar respectively) at constant mean cross-flow velocity of 0.04 $m \cdot s^{-1}$. The mean biofilm thickness (L_F) at the point/area of measurement is displayed inside the green box for each graph, including the standard deviation. The biofilm thickness without permeate flux is given as $L_F(0)$. Rather than the absolute sulfate concentration, the graphs show the CPF ($c \cdot c_{feed}^{-1}$).

Fig. 4.8 A shows the clean membrane results from chapter 3 (Fig. 3.4 B) and, for comparison, a depth profile with a severely biofouled membrane (taken from Fig. 4.8 D). The measurement confirms that the presence of biofilm increases the CPL. However, the thickness of the CPL does not appear to be affected the same way. This may be explained by the biofilm morphology (e.g. roughness and porosity) changing the flow field at the biofilm surface and increasing mass transport, which would diminish the CPL outside the biofilm. From the onset of the profile to 90 µm, the CPL does not substantially differ from the clean membrane CPL, which could suggest, that this point marks the biofilm boundary. Indeed, the mean biofilm thickness for this measurement was determined with OCT to be 90 µm. However, this is the only profile of the measurement series, which shows that distinction.

For all measurements, biofilm thickness is less than CPL thickness, which is plausible. However, the thickness of the CPL appears to be not correlated to the biofilm thickness. Instead, CPL thickness may be more dependent on surface morphology and the local hydrodynamic conditions. In contrast to CPL thickness, the CPL gradient does appear to be correlated to biofilm thickness. The comparison of the profiles B - D shows that the CPL gradient increases with increased biofilm thickness. The principal shape of the CPL does not differ from the clean membrane results and is representative of an exponential function. This is an indication that the biofilm does not change the principal mechanisms of CP (e.g. by introducing chemical reactions or physical barriers). Inside the biofouling layer, the diffusion coefficient for sulfate may be decreased leading to decreased diffusive mass transport back to the bulk solution. Maybe more importantly, transverse mass flow should be greatly diminished inside the biofilm as well. Both mechanisms would increase the gradient of the CPL. If transverse mass flow inside the biofilm is about zero, the CPL would also vary greatly locally. The biofilm is not uniform, neither is membrane permeation. Without convective transport to “smoothen” the CPL, greater local variance should be expected.

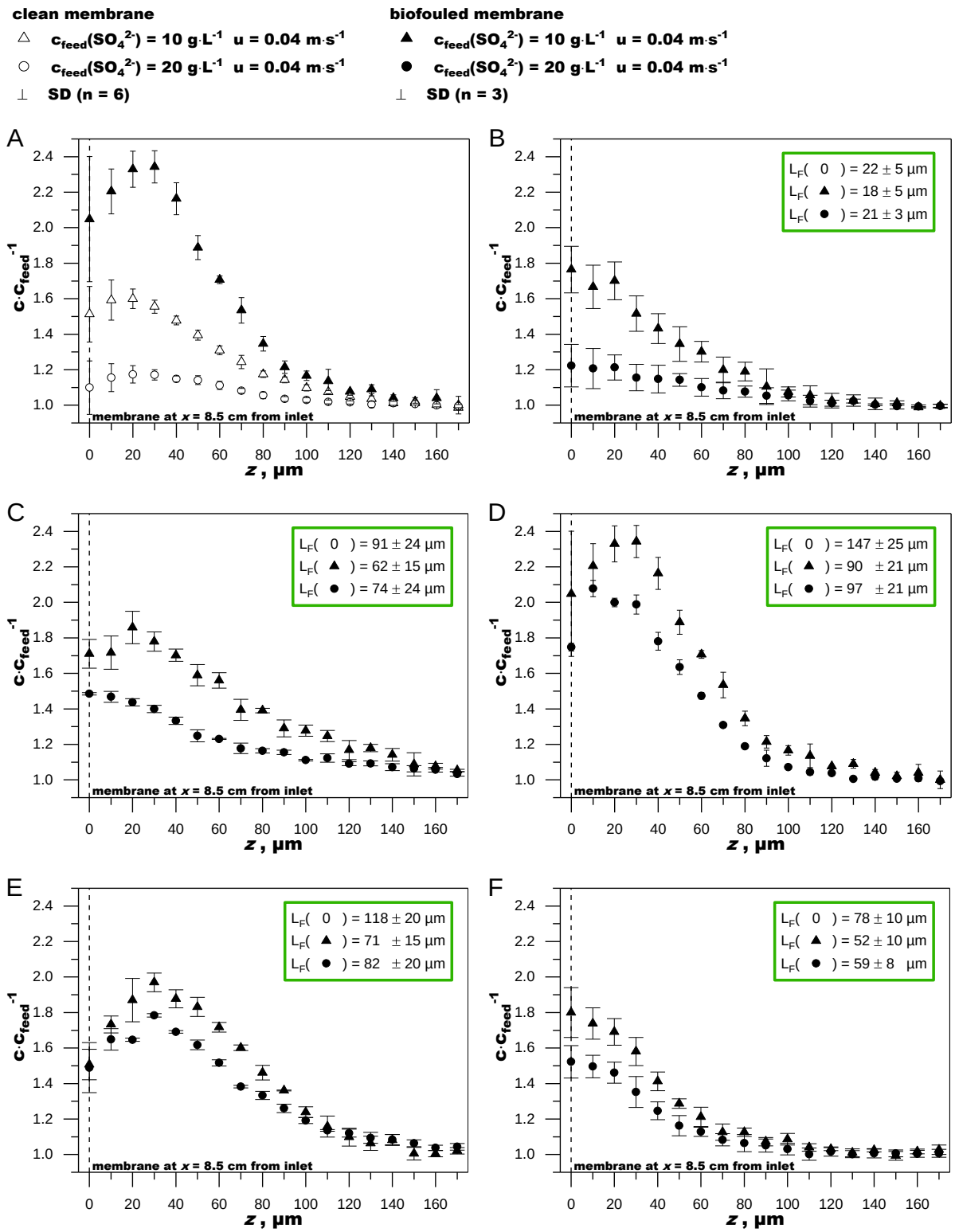

Fig. 4.8 RM measurements of CP profiles with biofouling. Filtration conditions: feed sulfate concentrations: 10 and 20 g·L^{-1}, mean cross-flow velocity: 0.04 m·s^{-1}, system pressure: 10 bar. Box lists biofilm thickness (L_F) from OCT analysis at the point of RM measurement. $L_F(0)$: biofilm thickness at zero permeate flux (calibration condition), A: comparison of clean membrane reference (Fig. 3.4) to biofouled membrane, B-D: CP profiles of biofouled

membranes of different biofilm thickness, E and F: CP profiles of one biofouled membrane, measurement points 1 mm (Δy) apart.

Profiles E and F were recorded with the same biofilm at two positions about 1 mm apart. The OCT analysis shows a difference in mean biofilm thickness of about 20 µm. This is also the magnitude of the standard deviation. Despite being at the same distance from the inlet, the concentration profiles are considerably different. The CPL is more severe at the position with a thicker biofilm structure, consistent with the other measurements. The CPF at the membrane surface differs by 20%. Furthermore, profile F shows the smallest CPL thickness of all measurements. Thus, CPL characteristics appear to greatly vary locally in connection with the condition of the local biofilm. This also means, that the bulk concentration becomes less important in determining the severity of the CPL.

To quantify the effect of biofilm, the CPF at the membrane surface can be compared with and without biofilm. Using the methodology described in chapter 2, the CPF at the membrane surface is obtained from the concentration profiles by linear extrapolation to the membrane surface using the slope of the mid-section of the profiles. For both conditions of 10 and 20 $g \cdot L^{-1}$ sulfate in feed, concentration values from 30 to 60 µm (4 points) were used to fit the linear slope. The clean membrane values were used as reference with $CPF_{clean} = 1.8$ and $CPF_{clean} = 1.3$ for 10 $g \cdot L^{-1}$ and 20 $g \cdot L^{-1}$ sulfate in feed respectively.

The increase of the CPF due to biofilm was calculated as a percentage of the clean membrane reference ($(CPF_{bio} - CPF_{clean}) \cdot CPF_{clean}^{-1}) \cdot 100\%$), which yields the two graphs shown in Fig. 4.9. Graph A shows the data for the lower feed concentration (effective pressure: 7.2 bar). The results show that the CPF is increased by up to 70% due to biofilm with a thickness of less than 100 µm. Furthermore, less than 10% increase was recorded for biofilm thicknesses of less than 60 µm, suggesting that the effect of biofilm on CP is small as long as the biofilm does not reach a critical thickness.

Interestingly, for the higher feed sulfate concentration (effective pressure: 4.4 bar), the effect of the biofilm is qualitatively and quantitively similar. Of course, both operating conditions were recorded with the same biofilms, yet due to compressibility, biofilm thickness is increased at lower TMP. Thus, the data points in graph B are associated with greater biofilm thickness. The data shows a consistent increase of the CPF to 94%, which is almost a doubling of the membrane surface concentration, at a thickness of about 100 µm. Comparing both graphs, a 60 to 70% increase is associated with a biofilm thickness of 80 to 90 µm and a 20% increase is associated with a biofilm thickness of about 70 µm in both graphs respectively. Superposition of both graphs yields the same correlation. This means, that the data supports a specific

increase of the membrane surface concentration to be associated with a specific biofilm thickness. Thus, measuring biofilm thickness could predict the CPF.

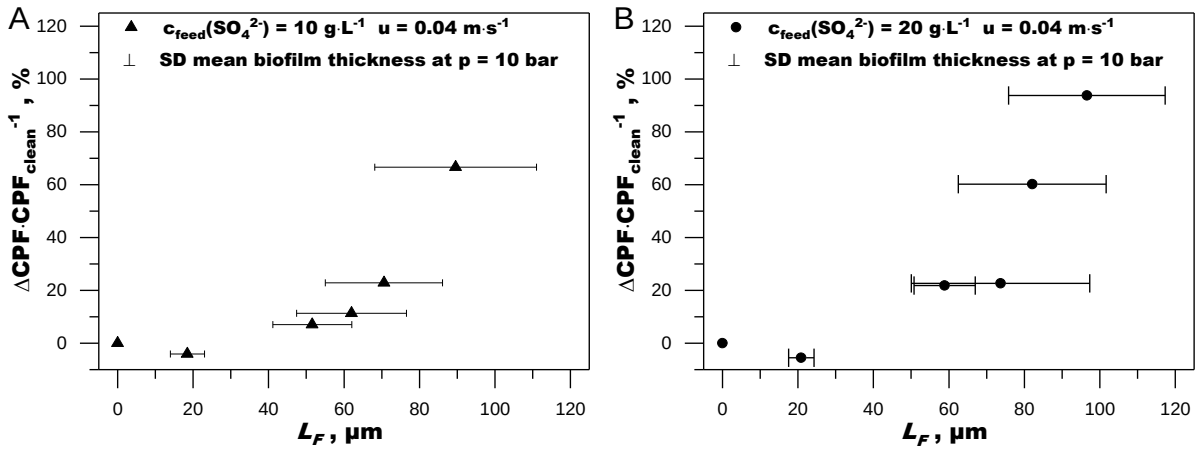

Fig. 4.9 Influence of Biofilm on the membrane wall concentration. Shown is the change of the CPF due to the biofilm as a percentage of the clean membrane reference: $\Delta CPF = CPF_{bio} - CPF_{clean}$.

The data supports the hypothesis that one of the main mechanisms for a decrease in filtration performance with biofouling is due to its effect on the CPL. Higher concentration at the membrane surface diminishes salt rejection and thus the permeate quality. Permeate flux declines because of diminished TMP due to higher osmotic pressure. Herzberg and Elimelech (2007) have termed this mechanism for flux decline “biofilm enhanced osmotic pressure” (BEOP). In their study, they compared biofouling with dead cells and biofouling under enhanced biofouling conditions with living cells in a laboratory setup. They concluded, that the increase of CP is attributed to the deposition of cells rather than the EPS matrix. According to the authors, the EPS matrix is merely responsible for additionally increasing hydraulic resistance to permeate flow and thus only partially adding to the main flux decline due to cell deposition(Herzberg and Elimelech 2007). Considering that EPS is 95-99% water, it is plausible to assume that diffusion coefficients remain similar within the EPS-matrix and cannot be a major cause for diminished back diffusion. A possible mechanism for enhanced CP with the deposition of dead cells can be hindered back diffusion by increased tortuosity within the biofouling layer. With an increased path length, the concentration gradient increases.

The contribution of hydraulic resistance can be assessed by minimizing the feed salt concentration, which was also done in the study by Herzberg and Elimelech (2007). The authors found that dead cells provide minimal hydraulic resistance relative to the hydraulic resistance of the membrane and thus can be neglected. The authors further compared

biofouling with a living biofilm with dead cell deposition. They conclude, that the additional flux decline observed with the living biofilm is caused by EPS, which the living cells produce, and attribute it to increased hydraulic resistance that the EPS-matrix provides. This conclusion is based on the finding that living biofilm shows less flux but with comparable salt passage to the dead cell experiment. This is a clear indication that the EPS-matrix did not contribute to further increase the CPL. The authors further suggest, that the increased hydraulic resistance is caused by a lower porosity of the fouling layer with the EPS filling up the space between cells.

However, it can be argued that comparing living biofilm with dead cell composition is not sufficient to support these claims. Both, deposition of dead cells as well as the EPS-matrix alter the local flow dynamics, mainly the transverse component of the convective flow (cross-flow). Furthermore, the experiments of Dreszer et al. have shown that hydraulic resistance of the biofilm is related to its compressibility (Dreszer et al. 2013, Dreszer et al. 2014). Thus, the thickness of the biofouling layer as well as its water permeability are components affecting the CPL. This work does not differentiate between the contribution of cells and contribution of EPS. It only shows the effect of biofouling layer thickness on the CPL. However, application of this new experimental technique to those experiments may further elucidate the individual contribution of the biofilm's components to overall flux decline.

4.2.3 Measurement Errors

Assessing the absolute values of the CPF data with biofouling reveals some implausible findings. For example, a doubling of the CPF in the case of 20 $g \cdot L^{-1}$ sulfate concentration would exceed the maximum plausible concentration of 35.5 $g \cdot L^{-1}$. At this point, osmotic pressure would be higher than system pressure and the CPL would collapse. This is evidence, that the measurements overestimate true CP with higher biofilm thickness. Nevertheless, the consistency of the measurements should not be overlooked and supports the findings at least qualitatively. From Fig. 4.9, it could be concluded that biofilm enhanced CP increases exponentially with biofilm thickness. However, considering that overestimation likely increases with biofilm thickness, this effect could solely be caused by measurement uncertainty and a linear increase may also be plausible.

It was mentioned earlier that biofilm compressibility has a profound impact on the measurement results due to the experimental methodology. Biofilm compressibility is likely the main cause for overestimation of the data, which also increases with biofilm thickness, since biofilm thickness appears to correlate with compressibility. This can be best demonstrated utilizing the PSF again as previously discussed in chapter 2.2.1. The biofilm causes the PSF

to be more shallow and wider, thus increasing FWHM, effectively lowering signal intensity and blurring the point of focus. Analysis of the membrane Raman bands gives a good representation of the shape of the PSF. Fig. 4.10 shows membrane Raman signals for clean and biofouled membranes. First, it should be noted, that the clean membrane signal has been recorded using half the excitation time of the biofouled recordings, effectively cutting Raman intensity in half too. Therefore, the signal loss due to a biofilm with a thickness of 90 µm is about 70%. With increasing biofilm thickness, signal intensity is reduced even further.

The graph marks the location of the respective half maximum and its intersections with the profiles. It shows that the biofilm is causing a wider profile, increasing FWHM. Interestingly, the effect is relatively small for a biofilm thickness up to at least 90 µm, increasing FWHM by about 20%. However, for the maximum biofilm thickness of 147 µm, the FWHM is more than doubled. Because the experimental methodology requires calibration with zero permeate flux, biofilm thickness is at its maximum during calibration (see also $L_F(0)$ in Fig. 4.8). Hence, calibration data is recorded with worse depth resolution (greater FWHM) and additional intensity loss relative to the measurement data. This effect scales with total biofilm thickness and total compressibility. For the CPL and CPF results recorded with this method (Fig. 4.8 and Fig. 4.9), this means that data points are severely overestimated at higher biofilm thickness (> 90 µm) and moderately overestimated at lower biofilm thickness (< 90 µm).

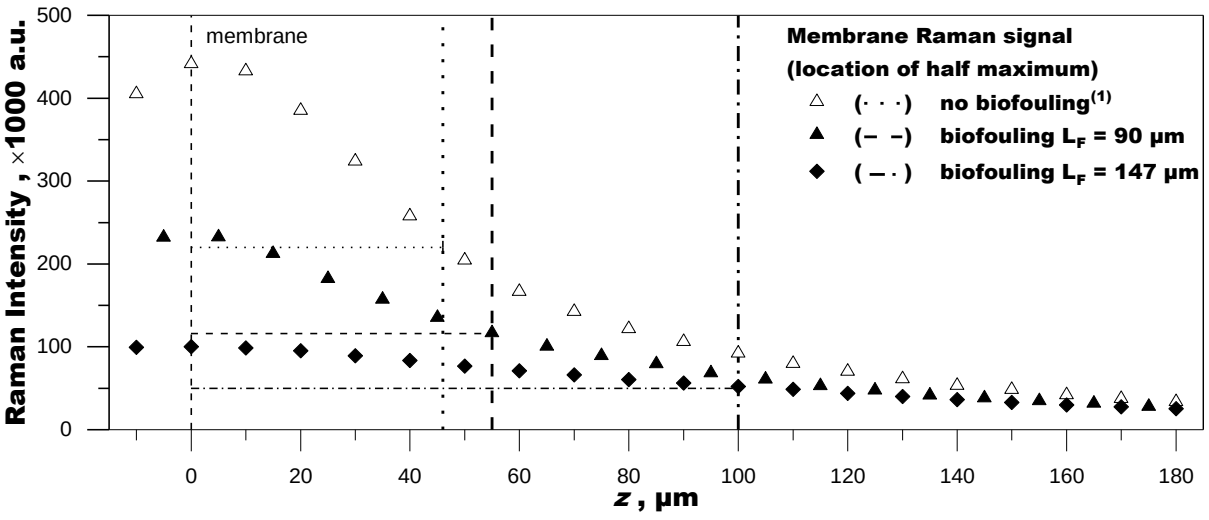

Fig. 4.10 Comparison of the membrane Raman signal with and without biofouling. Horizontal lines show the location of half maximum. Vertical lines show ½ FWHM. (1)data recorded with integration time of 30s instead of 60s.

It should be noted, that the quantification of Raman intensity loss and the changes in depth resolution only refer to the measurement position z = 0 µm (membrane surface) as this is the

only plane where a signal maximum (i.e. membrane Raman bands) can be definitely assigned to. At the plane of the membrane surface, these effects are also greatest and the numbers reflect the maximum signal deterioration. For all other points along the optical axis, the effect is smaller but cannot be quantified from the collected data. For this reason, it cannot be corrected by a single adjustment factor. This is also the reason why the calibration methodology was introduced. To be clear, the loss in Raman intensity due to the biofilm in itself is not problematic and could be overcome by increasing excitation time. The deterioration of depth resolution, too, has little influence, especially at a biofilm thickness of less than 90 µm. It is biofilm compressibility, which is problematic because it causes both Raman intensity loss and depth resolution to change substantially with operating conditions. If the biofilm were not compressible, the methodology would likely provide accurate results.

4.3 Conclusions

The combination of OCT with RM is a promising new technique to analyze the mechanisms of biofilm enhanced osmotic pressure (BEOP). In this study, membrane biofouling was induced by successfully growing a *B. subtilis* biofilm in a NF flow cell over a period of up to 6 days. It was shown that filtration performance deteriorates with accumulation of biomass on the membrane surface. After 5 days of growth, permeate flux was reduced by 75% and permeate conductivity was increased by 47%. Using RM, the CPL was measured with bioufouled membranes and compared to previously measured clean membrane data. The measurements showed, that biofouling increases the solute concentration at the membrane surface, thus also increasing the osmotic pressure. Therefore, the measurements confirm that BEOP is a mechanism for flux decline in NF systems experiencing biofouling.

OCT was used to provide analyzes of biofilm thickness at the point of RM measurement. The analyses revealed that the severity of BEOP scales with biofilm thickness. The measurements suggest, that a critical biofilm thickness has to be reached before BEOP becomes severe. Up to a biofilm thickness of 60 µm, an increase in membrane surface concentration of less than 10% was recorded.

Apart from thickness data, OCT also provides a visual representation of the biofilm morphology. The biofilm is an uneven, rough structure and biofilm thickness greatly varies within the microscale of the RM measurement. Whereas the CPL above a clean membrane with no feed spacer is uniform, it varies with a biofouled membrane along the local biofilm characteristics. The RM and OCT measurements showed no correlation of CPL thickness and biofilm thickness. It is proposed that roughness of the biofilm affects mass transport near the

biofilm surface by changing the local hydrodynamic conditions and that due to this effect, CPL thickness may be more dependent on local biofilm morphology.

The OCT analyses also showed that the biofilm reacts to changes in permeate flux with compression and relaxation. It is therefore suggested, that membrane filtration experiments may be a viable tool to study biofilm characteristics such as elasticity, density or hydraulic permeability. In this study, biofilm compression or relaxation was completely reversible and only dependent on permeate flux.

However, biofilm compressibility poses problems to the RM measurement methodology. The biofilm causes a loss of signal intensity and a deterioration of depth resolution. Although depth resolution is only moderately (<20%) affected up to a biofilm thickness of about 90 µm, it is more than doubled at the highest biofilm thickness of 147 µm. Because calibration measurements require zero permeate flux conditions, biofilm thickness is greater at calibration leading to additional loss in signal compared to CPL measurement conditions. This results in a gross overestimation of the concentration data with thicker biofilms to the point of implausible absolute concentration values. This prevents an accurate quantitative analysis of the CPL data. However, since this measurement error is regular and correlates with biofilm thickness, relative interpretation of the data should be legitimate, which means that qualitative findings should be unaffected and remain valid.

With successfully measuring the CPL *in-situ*, studying the contribution of individual components of the biofilm towards filtration performance should become accessible, i.e. bacterial cells, distribution and composition of EPS, biofilm morphology etc. This kind of research has been identified as areas of primary importance for future studies, e.g. Bucs et al. (2018) and Flemming (2020). Biofilms present a natural phenomenon, which is unlikely to be eliminated. Thus, an “integrated strategy” (Flemming 2020) to mitigate their detrimental effects to technical systems is required. The aim is to live with and understand the mechanism by which a biofilm negatively effects system performance, which may enable new kinds of solutions like methods to tailor biofilm properties towards beneficial outcomes. This work demonstrates that RM in combination with OCT should belong inside the toolkit of this “integrated strategy”. RM offers direct and localized data of concentration and its gradient inside and outside a biofilm matrix. When the aim shifts from preventing biofilm formation, which has only seen limited success, to manage and living with biofilms, mitigating their negative impact through new and innovative solutions, then a non-invasive technique to directly measure the influence of a given biofilm matrix on the CPL in a membrane flow channel should be appealing.

5 Summary and Outlook

This work takes a well-established, readily available measurement technique, confocal Raman microspectroscopy (RM), and applies it to *in-situ* measurement of the concentration distribution inside membrane feed channels. It is motivated by the persistent lack of experimental methods to inform and support theoretical and numerical modeling approaches, which have been implemented with great success, but may be reaching their limits, as evidenced by the declining number of publications in an overall growing research area (Oatley-Radcliffe et al. 2017). RM presents the first measurement method, which can be applied with a NF flow cell representative of common spiral wound modules and to also permit commercial spacers inside the feed channel. Thus, a proof-of-concept laboratory study was designed to investigate the potential of RM for measurement of concentration polarization (CP) in practical membrane applications. A flat-sheet cross-flow membrane cell with two pressure resistant windows was developed and equipped with a commercial NF membrane. The flow cell can be equipped with commercial 28 mil feed spacers and provides an active membrane area of 33.6 cm^2.

The measurement principle utilizes the Raman activity of the sulfate ion to measure the sulfate concentration within an aquatic volume. Coupled with a confocal microscope, the concentration distribution inside membrane feed channels can be scanned. The theoretical maximum resolution is in the range of a few micrometers. Due to the different refractive power of air, water and cover windows, spherical aberration is introduced to the system, which severely deteriorates depth resolution. The actual maximum depth resolution of the present setup was determined to be about 65 µm. With oversampling and evaluation of the relative differences, concentration gradients were measured with a resolution of up to 5 µm with sulfate concentrations in the order of 10 $g \cdot L^{-1}$. A calibration methodology was developed to relate the relative differences to absolute concentration. By scanning through the feed channel at filtration conditions where no permeate is produced, linear correlations of Raman intensity to sulfate concentrations are obtained for each point of the depth scale. These correlations contain the information about the signal loss due to spherical aberration in a uniform medium and thus correct for them. It was found, that accurate data can be obtained up to about 30 µm from the membrane surface.

Concentration profiles were obtained at two positions along the center of the feed channel for sulfate feed concentrations of 10 and 20 $g \cdot L^{-1}$ and cross-flow velocities ranging from 0.004 to 0.2 $m \cdot s^{-1}$. Membrane recovery ranged from 0.5 to 31%. Filtration performance and locally resolved measurement results were in good agreement. At the lowest cross-flow velocity without the presence of a feed spacer, an influence of membrane orientation on filtration performance was observed. With permeate flux in opposite direction to gravitational force,

permeate flux and quality was substantially improved. The RM measurement revealed a non-uniform distribution of the sulfate concentration within the membrane feed channel and local detachment of the CPL from the membrane surface. The RM measurement results indicate a natural convection phenomenon to be responsible for the improved mass transfer. Filtration against gravity presents an unstable orientation, which introduces Rayleigh-Taylor-Instability (RTI). At low cross-flow velocity, RTI becomes significant. High resolution images were able to resolve the typical “spikes” and “bubbles” observed with RTI and show the dimensions and development of the disturbance during the initial stages. Thus, making this the first study, which measured RTI in a NF system. Filtration performance with natural convection was quantitively similar to the performance with a commercial feed spacer. Filtration experiments with feed spacer showed no apparent influence of natural convection. The concentration distribution within a feed spacer element could be resolved at low cross-flow velocity. Comparison with velocity distributions within spacer elements taken from numerical simulations in published literature showed great similarity. The concentration distribution was shown to be inverse to the velocity distribution from the simulation.

Being a laboratory proof-of-concept type study, experimental conditions were simplified as much as possible. The feed solution only contained two divalent ions, Mg^{2+} and SO_4^{2-}, in order to simplify filtration conditions and feed solution chemistry. However, this method principally extends to all Raman active molecules and molecular ions, e.g. nitrate, chlorate etc. and published work already exists proving sodium chloride to not interfere with sulfate Raman measurements up to concentrations of natural salt waters (Murata et al. 1997). Thus, the present experimental concept is likely applicable to particle free natural salt waters and other common NF feed sources. In combination with great usability and accessibility of Raman and membrane filtration equipment, the present concept, thus, provides a great opportunity to complement innovative studies in the field of membrane water treatment.

Although the calibration methodology is an elegant way to account for various optical affects simultaneously, it requires great similarity between calibration and measurement conditions. When the concentration distribution inside the feed channel is mostly uniform, e.g. without feed spacer and no disturbance to the flow field, quantitative evaluation of the measurement results can be expected to be accurate with relatively small measurement uncertainty. At more complex hydrodynamic conditions with larger variations to the local salt concentration along the optical axis, e.g. with feed spacers or natural convection, the calibration methodology fails to accurately account for spherical aberration. This results in underestimation of the absolute concentration deeper into the feed channel. The degree of measurement uncertainty is dependent on the conditions and should correlate with the severity of the concentration gradients along the optical axis.

There are several possible methods to improve the experimental setup as well as measurement data evaluation. Depth resolution can be improved by elimination of refractive interfaces. Immersion objectives are available, however, immersion into the pressurized feed channel is practically challenging and introduces disturbance to the flow field. Non-invasive setups with immersion objectives should also be possible, however shorter working distances of immersion objectives demand compromises in window thickness (pressure resistance) and feed channel height. Mathematical modeling and rigorous scrutiny of the optical pathway (ray tracing) for a given Raman system may be a possibility to correct for spherical aberration. However, the correction will likely only be applicable to the specific system. Data evaluation will likely benefit from combination with models for mass transport in membrane feed channels. Uncertainty of measurement data varies with local conditions. Models could be used for extrapolation based on data points with low uncertainty.

In the final study of this work, RM was combined with OCT to study the influence of biofouling on CP. Both techniques are non-invasive, optical methods, which use light sources in the visible spectrum and, thus, complement each other well. The NF flow cell was subjected to enhanced biofouling conditions by using a growth medium inoculated with *Bacillus subtilis* as the feed solution. In the growth period, the filtration unit was operated with an alternating pressure regimen. OCT was used to analyze the biofilm and determine biofilm thickness. Evaluation with OCT showed that the biofilm reacts to variations in permeate flux with compression and relaxation. It was suggested that biofilm thickness during filtration is determined by a force equilibrium between biofilm elasticity and permeation velocity.

OCT analysis was performed at the same position as RM measurements, which permitted to relate biofilm thickness to concentration profiles. Measurements with four independently grown biofilms showed that severity of CP correlated with biofilm thickness. Thus, the measurements confirmed biofilm enhanced osmotic pressure (BEOP) as a mechanism for flux decline and decreased permeate quality in biofouled membranes. The measurements further suggest a critical biofilm thickness before flux decline and BEOP become severe. By causing increased salt concentration at the membrane surface, biofilms facilitate other fouling types, specifically scaling. The measurements showed the CPL thickness was not correlated to the severity of CP. It was suggested that biofilm morphology affects the flow field at the biofilm surface, which influences local mass transport. In order to quantify the effect of a biofilm on CP, the relative increase of the CPF to clean membranes was determined. The measurements showed that a specific increase in CPF was associated with a specific biofilm thickness.

The presence of biofilm lead to major loss in signal intensity for the RM measurements. It was also demonstrated that the biofilm deteriorates depth resolution, specifically at a thickness

greater 90 µm. Furthermore, biofilm compressibility poses problems to the calibration methodology. Since calibration requires conditions of zero permeate flux, biofilm thickness was increased by up to 60 µm during calibration measurements, which caused additional loss in signal intensity. As a result, the methodology overestimates concentration values near the membrane surface, particularly with thicker (>90 µm) biofilms, which also demonstrated greater compressibility.

The observations regarding biofilm thickness and its relation to permeate flux indicate, that biofilm properties in a fouled membrane system depend on operating conditions. Thus, with regards to future research, controlled permeation studies utilizing membranes may be a viable tool to investigate mechanical biofilm properties. Furthermore, in order to accurately assess biofilm properties of practical biofilms found on membranes in water treatment, it appears necessary to replicate the operating conditions the membrane element is subjected to during practical operation. This study, for example, found that a biofilm subjected to higher permeation velocity during growth showed lower compressibility. Thus, with lower compressibility, the present concept may be more applicable to practical biofouling. Also, the results demonstrate that non-invasive technique like RM and OCT are favorable for researching biofilm properties of practical biofilms in membrane water treatment.

Appendix

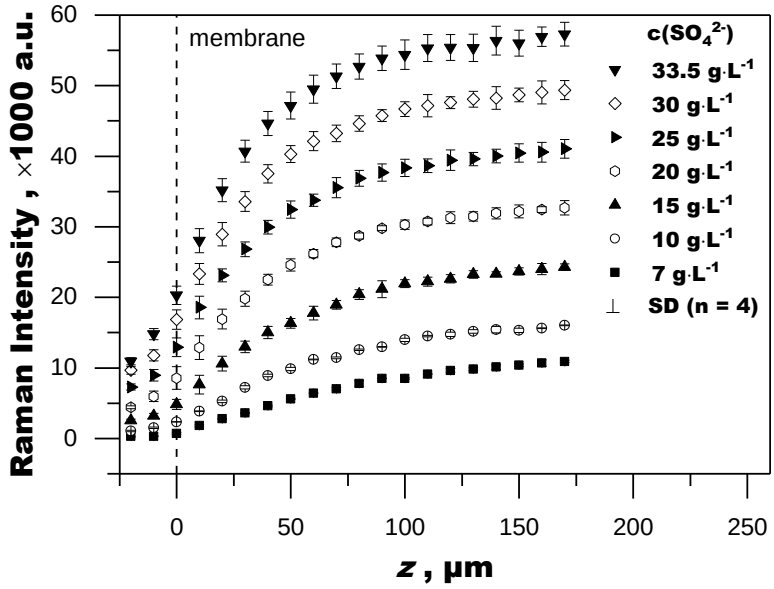

Fig.A1 Calibration data set: depth profiles recorded for multiple concentrations with no filtration operating conditions (unpressurized), u = 0.2 ms-1, p = 0.14 bar (unpressurized operation). SD: standard deviation

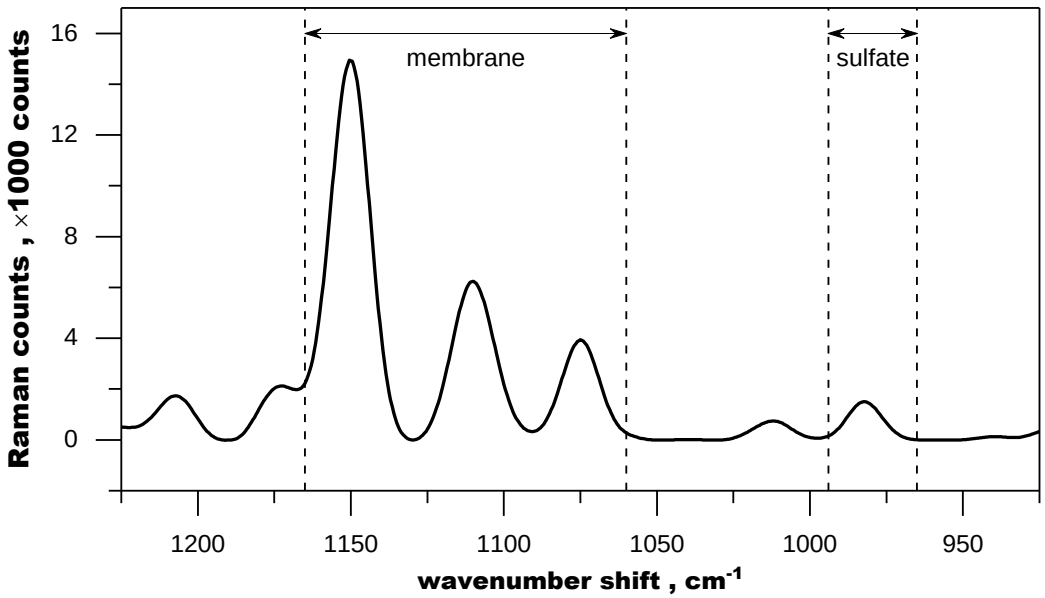

Fig.A2 Raman spectra of the surface of NF270 membrane biofouled with *B. subtilis* in magnesium sulfate solution of 10 g·L-1 sulfate. Raw Raman spectra with baseline correction. Markups show Raman bands used for evaluation. Spectra was taken from the biofilm shown in Fig.A3.

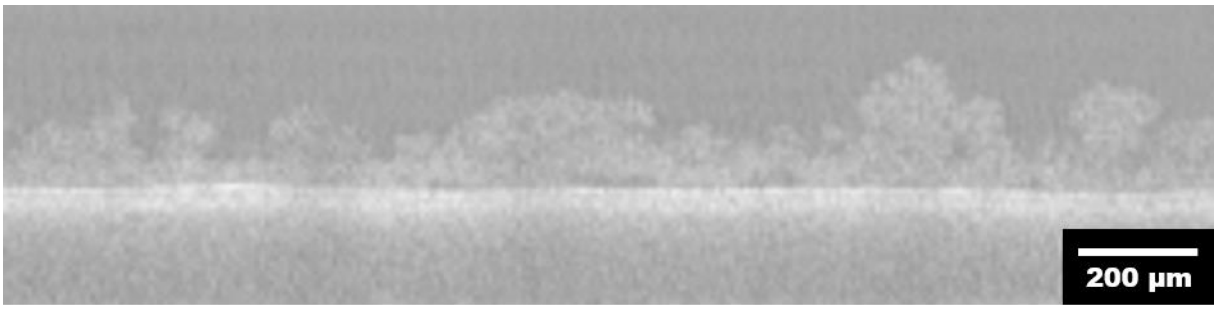

Fig.A3 Original OCT image before manipulation

Table A1. Calibration data for each depth point z = -20 µm to z = 170 µm with Δz = 10 µm correlating Raman intensity to sulfate concentration

Depth position (*z*)	Offset	Slope	R^2 (COD)
170	-1.360	1.717	0.999
160	-1.639	1.714	0.999
150	-1.402	1.678	0.999
140	-2.040	1.706	0.998
130	-2.048	1.687	0.999
120	-2.499	1.696	0.999
110	-2.977	1.698	0.998
100	-3.375	1.693	0.999
90	-3.814	1.683	0.998
80	-4.233	1.660	0.998
70	-5.098	1.644	0.998
60	-5.366	1.598	0.997
50	-6.081	1.558	0.998
40	-6.460	1.484	0.997
30	-6.866	1.372	0.995
20	-6.799	1.213	0.995
10	-6.213	0.994	0.993
0	-4.136	0.651	0.978
-10	-4.156	0.538	0.986
-20	-3.222	0.418	0.988

References

Anger, P.M., Esch, E.v.d., Baumann, T., Elsner, M., Niessner, R. and Ivleva, N.P. (2018) Raman Microspectroscopy as a Tool for Microplastic Particle Analysis. TrAC Trends in Analytical Chemistry.

Anis, S.F., Hashaikeh, R. and Hilal, N. (2019) Reverse osmosis pretreatment technologies and future trends: A comprehensive review. Desalination 452, 159-195.

Antony, A., Low, J.H., Gray, S., Childress, A.E., Le-Clech, P. and Leslie, G. (2011) Scale formation and control in high pressure membrane water treatment systems: A review. Journal of Membrane Science 383(1–2), 1-16.

Araujo, C.F., Nolasco, M.M., Ribeiro, A.M.P. and Ribeiro-Claro, P.J.A. (2018) Identification of microplastics using Raman spectroscopy: Latest developments and future prospects. Water Research 142, 426-440.

Arnaouteli, S., MacPhee, C.E. and Stanley-Wall, N.R. (2016) Just in case it rains: building a hydrophobic biofilm the Bacillus subtilis way. Current Opinion in Microbiology 34, 7-12.

Benecke, J., Rozova, J. and Ernst, M. (2018) Anti-scale effects of select organic macromolecules on gypsum bulk and surface crystallization during reverse osmosis desalination. Separation and Purification Technology 198, 68-78.

Blauert, F., Horn, H. and Wagner, M. (2015) Time-resolved biofilm deformation measurements using optical coherence tomography. Biotechnology and Bioengineering 112(9), 1893-1905.

Bucs, S.S., Farhat, N., Kruithof, J.C., Picioreanu, C., van Loosdrecht, M.C.M. and Vrouwenvelder, J.S. (2018) Review on strategies for biofouling mitigation in spiral wound membrane systems. Desalination 434, 189-197.

Chen, J.C., Li, Q. and Elimelech, M. (2004) In situ monitoring techniques for concentration polarization and fouling phenomena in membrane filtration. Advances in Colloid and Interface Science 107(2–3), 83-108.

Cheng, T.-W. and Lin, C.-T. (2004) A study on cross-flow ultrafiltration with various membrane orientations. Separation and Purification Technology 39(1), 13-22.

Chmiel, G. and Fritz, S.J. (2006) In situ quantification of the concentration polarization layer in a hyperfiltration system. Journal of Membrane Science 285(1), 214-224.

Chong, T.H., Wong, F.S. and Fane, A.G. (2008) The effect of imposed flux on biofouling in reverse osmosis: Role of concentration polarisation and biofilm enhanced osmotic pressure phenomena. Journal of Membrane Science 325(2), 840-850.

CRC Handbook of Chemistry and Physics: "Concentrative Properties Of Aqueous Solutions: Density, Refractive Index, Freezing Point Depression, And Viscosity", Section 8. Internet Version 2005, Lide, D.R. (ed), CRC Press, Boca Raton, FL, 2005.

Darton, T., Annunziata, U., del Vigo Pisano, F. and Gallego, S. (2004) Membrane autopsy helps to provide solutions to operational problems. Desalination 167, 239-245.

Dhamelincourt, P. (2002) Handbook Of Vibrational Spectroscopy. Chalmers, J.M. and Griffiths, P.R. (eds), John Wiley & Sons Ltd.

DOW (2005) Filmtec™ Reverse Osmosis Membranes: Technical Manual, Dow Water & Process Solutions, DOW Liquid Separations.

Dreszer, C., Vrouwenvelder, J.S., Paulitsch-Fuchs, A.H., Zwijnenburg, A., Kruithof, J.C. and Flemming, H.C. (2013) Hydraulic resistance of biofilms. Journal of Membrane Science 429, 436-447.

Dreszer, C., Wexler, A.D., Drusová, S., Overdijk, T., Zwijnenburg, A., Flemming, H.C., Kruithof, J.C. and Vrouwenvelder, J.S. (2014) In-situ biofilm characterization in membrane systems using Optical Coherence Tomography: Formation, structure, detachment and impact of flux change. Water Research 67, 243-254.

Dudley, L.Y. and Darton, E.G. (1996) Membrane autopsy — a case study. Desalination 105(1), 135-141.

Earl, A.M., Losick, R. and Kolter, R. (2008) Ecology and genomics of Bacillus subtilis. Trends in Microbiology 16(6), 269-275.

Egea-Corbacho, A., Gutiérrez Ruiz, S. and Quiroga Alonso, J.M. (2019) Removal of emerging contaminants from wastewater using nanofiltration for its subsequent reuse: Full–scale pilot plant. Journal of Cleaner Production 214, 514-523.

Epstein, A.K., Pokroy, B., Seminara, A. and Aizenberg, J. (2011) Bacterial biofilm shows persistent resistance to liquid wetting and gas penetration. Proceedings of the National Academy of Sciences 108(3), 995.

Everall, N.J. (2000) Modeling and Measuring the Effect of Refraction on the Depth Resolution of Confocal Raman Microscopy. Applied Spectroscopy 54(6), 773-782.

Everall, N.J. (2009) Confocal Raman Microscopy: Performance, Pitfalls, and Best Practice. Applied Spectroscopy 63(9), 245A-262A.

Everall, N.J. (2010) Confocal Raman microscopy: common errors and artefacts. Analyst 135(10), 2512-2522.

Fang, W., Shi, L. and Wang, R. (2013) Interfacially polymerized composite nanofiltration hollow fiber membranes for low-pressure water softening. Journal of Membrane Science 430, 129-139.

Fernández-Sempere, J., Ruiz-Beviá, F., García-Algado, P. and Salcedo-Díaz, R. (2010) Experimental study of concentration polarization in a crossflow reverse osmosis system using Digital Holographic Interferometry. Desalination 257(1–3), 36-45.

Flemming, H.-C. (1997) Reverse osmosis membrane biofouling. Experimental Thermal and Fluid Science 14(4), 382-391.

Flemming, H.-C. (2020) Biofouling and me: My Stockholm syndrome with biofilms. Water Research, 115576.

Flemming, H.-C. and Wingender, J. (2010) The biofilm matrix. Nature Reviews Microbiology 8(9), 623-633.

Flemming, H.C. (2002) Biofouling in water systems--cases, causes and countermeasures. Appl Microbiol Biotechnol 59(6), 629-640.

Fredericks, P.M. (2002) Handbook Of Vibrational Spectroscopy. Chalmers, J.M. and Griffiths, P.R. (eds), John Wiley & Sons Ltd.

Fujimoto, J. and Drexler, W. (2008) Optical Coherence Tomography: Technology and Applications. Drexler, W. and Fujimoto, J.G. (eds), pp. 1-45, Springer Berlin Heidelberg, Berlin, Heidelberg.

García-Martín, N., Silva, V., Carmona, F.J., Palacio, L., Hernández, A. and Prádanos, P. (2014) Pore size analysis from retention of neutral solutes through nanofiltration membranes. The contribution of concentration–polarization. Desalination 344, 1-11.

Gierl, L., Stoy, K., Faíña, A., Horn, H. and Wagner, M. (2020) An open-source robotic platform that enables automated monitoring of replicate biofilm cultivations using optical coherence tomography. npj Biofilms and Microbiomes 6(1), 18.

Griffiths, P.R. (2002) Handbook Of Vibrational Spectroscopy. Chalmers, J.M. and Griffiths, P.R. (eds), John Wiley & Sons Ltd.

Guendouzi, M.E., Mounir, A. and Dinane, A. (2003) Water activity, osmotic and activity coefficients of aqueous solutions of Li2SO4, Na2SO4, K2SO4, (NH4)2SO4, MgSO4, MnSO4, NiSO4, CuSO4, and ZnSO4 at T=298.15K. The Journal of Chemical Thermodynamics 35(2), 209-220.

Hamingerova, M., Borunsky, L. and Beckmann, M. (2015) Techview Report - Membrane Technologies for Water and Wastewater Treatment on the European and Indian Market, Fraunhofer MOEZ.

Hendra, P.J. (2002) Handbook Of Vibrational Spectroscopy. Chalmers, J.M. and Griffiths, P.R. (eds), John Wiley & Sons Ltd.

Herzberg, M. and Elimelech, M. (2007) Biofouling of reverse osmosis membranes: Role of biofilm-enhanced osmotic pressure. Journal of Membrane Science 295(1), 11-20.

Ivleva, N.P., Kubryk, P. and Niessner, R. (2017) Raman microspectroscopy, surface-enhanced Raman scattering microspectroscopy, and stable-isotope Raman microspectroscopy for biofilm characterization. Analytical and Bioanalytical Chemistry 409(18), 4353-4375.

Jamaly, S., Darwish, N.N., Ahmed, I. and Hasan, S.W. (2014) A short review on reverse osmosis pretreatment technologies. Desalination 354, 30-38.

Keresztury, G. (2002) Handbook Of Vibrational Spectroscopy. Chalmers, J.M. and Griffiths, P.R. (eds), John Wiley & Sons Ltd.

Kim, S. and Hoek, E.M.V. (2005) Modeling concentration polarization in reverse osmosis processes. Desalination 186(1), 111-128.

Komlenic, R. (2010) Rethinking the causes of membrane biofouling. Filtration & Separation 47(5), 26-28.

Kull, H.J. (1991) Theory of the Rayleigh-Taylor instability. Physics Reports 206(5), 197-325.

Labban, O., Liu, C., Chong, T.H. and Lienhard V, J.H. (2017) Fundamentals of low-pressure nanofiltration: Membrane characterization, modeling, and understanding the multi-ionic interactions in water softening. Journal of Membrane Science 521, 18-32.

Lamsal, R., Harroun, S.G., Brosseau, C.L. and Gagnon, G.A. (2012) Use of surface enhanced Raman spectroscopy for studying fouling on nanofiltration membrane. Separation and Purification Technology 96, 7-11.

Lau, W.J., Ismail, A.F., Misdan, N. and Kassim, M.A. (2012) A recent progress in thin film composite membrane: A review. Desalination 287, 190-199.

Lee, S., Ang, W.S. and Elimelech, M. (2006) Fouling of reverse osmosis membranes by hydrophilic organic matter: implications for water reuse. Desalination 187(1), 313-321.

Mohammad, A.W., Teow, Y.H., Ang, W.L., Chung, Y.T., Oatley-Radcliffe, D.L. and Hilal, N. (2015) Nanofiltration membranes review: Recent advances and future prospects. Desalination 356, 226-254.

Murata, K., Kawakami, K., Matsunaga, Y. and Yamashita, S. (1997) Determination of sulfate in brackish waters by laser Raman spectroscopy. Analytica Chimica Acta 344(1–2), 153-157.

Nath, K., Dave, H.K. and Patel, T.M. (2018) Revisiting the recent applications of nanofiltration in food processing industries: Progress and prognosis. Trends in Food Science & Technology 73, 12-24.

Oatley-Radcliffe, D.L., Walters, M., Ainscough, T.J., Williams, P.M., Mohammad, A.W. and Hilal, N. (2017) Nanofiltration membranes and processes: A review of research trends over the past decade. Journal of Water Process Engineering 19, 164-171.

Pahlow, S., Meisel, S., Cialla-May, D., Weber, K., Rösch, P. and Popp, J. (2015) Isolation and identification of bacteria by means of Raman spectroscopy. Advanced Drug Delivery Reviews 89, 105-120.

Picioreanu, C., Blauert, F., Horn, H. and Wagner, M. (2018) Determination of mechanical properties of biofilms by modelling the deformation measured using optical coherence tomography. Water Research 145, 588-598.

Picioreanu, C., Vrouwenvelder, J.S. and van Loosdrecht, M.C.M. (2009) Three-dimensional modeling of biofouling and fluid dynamics in feed spacer channels of membrane devices. Journal of Membrane Science 345(1), 340-354.

Qiu, T.Y. and Davies, P.A. (2015) Concentration polarization model of spiral-wound membrane modules with application to batch-mode RO desalination of brackish water. Desalination 368, 36-47.

Radu, A.I., Bergwerff, L., van Loosdrecht, M.C.M. and Picioreanu, C. (2014) A two-dimensional mechanistic model for scaling in spiral wound membrane systems. Chemical Engineering Journal 241, 77-91.

Radu, A.I., Bergwerff, L., van Loosdrecht, M.C.M. and Picioreanu, C. (2015) Combined biofouling and scaling in membrane feed channels: a new modeling approach. Biofouling 31(1), 83-100.

Radu, A.I., Vrouwenvelder, J.S., van Loosdrecht, M.C.M. and Picioreanu, C. (2010) Modeling the effect of biofilm formation on reverse osmosis performance: Flux, feed channel pressure drop and solute passage. Journal of Membrane Science 365(1), 1-15.

Raman, C.V. and Krishnan, K.S. (1928) A New Type of Secondary Radiation. Nature 121(3048), 501-502.

Robinson, R.A. and Stokes, R.H. (1949) Tables of osmotic and activity coefficients of electrolytes in aqueous solution at 25[degree] C. Transactions of the Faraday Society 45(0), 612-624.

Roccaro, P. (2018) Treatment processes for municipal wastewater reclamation: The challenges of emerging contaminants and direct potable reuse. Current Opinion in Environmental Science & Health 2, 46-54.

Sablani, S.S., Goosen, M.F.A., Al-Belushi, R. and Wilf, M. (2001) Concentration polarization in ultrafiltration and reverse osmosis: a critical review. Desalination 141(3), 269-289.

Salcedo-Díaz, R., García-Algado, P., García-Rodríguez, M., Fernández-Sempere, J. and Ruiz-Beviá, F. (2014) Visualization and modeling of the polarization layer in crossflow reverse osmosis in a slit-type channel. Journal of Membrane Science 456, 21-30.

Scharfer, P., Schabel, W. and Kind, M. (2007) Mass transport measurements in membranes by means of in situ Raman spectroscopy—First results of methanol and water profiles in fuel cell membranes. Journal of Membrane Science 303(1–2), 37-42.

Schindelin, J., Arganda-Carreras, I., Frise, E., Kaynig, V., Longair, M., Pietzsch, T., Preibisch, S., Rueden, C., Saalfeld, S., Schmid, B., Tinevez, J.-Y., White, D.J., Hartenstein, V., Eliceiri, K., Tomancak, P. and Cardona, A. (2012) Fiji. An open-source platform for biological-image analysis. Nature Methods 9, 682.

Shakaib, M., Hasani, S.M.F. and Mahmood, M. (2009) CFD modeling for flow and mass transfer in spacer-obstructed membrane feed channels. Journal of Membrane Science 326(2), 270-284.

Shirazi, S., Lin, C.-J. and Chen, D. (2010) Inorganic fouling of pressure-driven membrane processes — A critical review. Desalination 250(1), 236-248.

Singh, P., Singh, M.K., Beg, Y.R. and Nishad, G.R. (2019) A review on spectroscopic methods for determination of nitrite and nitrate in environmental samples. Talanta 191, 364-381.

Thompson, J., Lin, N., Lyster, E., Arbel, R., Knoell, T., Gilron, J. and Cohen, Y. (2012) RO membrane mineral scaling in the presence of a biofilm. Journal of Membrane Science 415-416, 181-191.

Van der Bruggen, B., Everaert, K., Wilms, D. and Vandecasteele, C. (2001) Application of nanofiltration for removal of pesticides, nitrate and hardness from ground water: rejection properties and economic evaluation. Journal of Membrane Science 193(2), 239-248.

Van der Bruggen, B., Mänttäri, M. and Nyström, M. (2008) Drawbacks of applying nanofiltration and how to avoid them: A review. Separation and Purification Technology 63(2), 251-263.

Virtanen, T., Reinikainen, S.-P., Kögler, M., Mänttäri, M., Viitala, T. and Kallioinen, M. (2017) Real-time fouling monitoring with Raman spectroscopy. Journal of Membrane Science 525, 312-319.

Vrouwenvelder, J.S. and van der Kooij, D. (2001) Diagnosis, prediction and prevention of biofouling of NF and RO membranes. Desalination 139(1), 65-71.

Wagner, M. and Horn, H. (2017) Optical coherence tomography in biofilm research: A comprehensive review. Biotechnology and Bioengineering 114(7), 1386-1402.

Wagner, M., Ivleva, N.P., Haisch, C., Niessner, R. and Horn, H. (2009) Combined use of confocal laser scanning microscopy (CLSM) and Raman microscopy (RM): Investigations on EPS – Matrix. Water Research 43(1), 63-76.

Wagner, M., Taherzadeh, D., Haisch, C. and Horn, H. (2010) Investigation of the mesoscale structure and volumetric features of biofilms using optical coherence tomography. Biotechnology and Bioengineering 107, 844-853.

Wang, J., Dlamini, D.S., Mishra, A.K., Pendergast, M.T.M., Wong, M.C.Y., Mamba, B.B., Freger, V., Verliefde, A.R.D. and Hoek, E.M.V. (2014) A critical review of transport through osmotic membranes. Journal of Membrane Science 454, 516-537.

Wijmans, J.G. and Baker, R.W. (1995) The solution-diffusion model: a review. Journal of Membrane Science 107(1), 1-21.

Wilking, J.N., Zaburdaev, V., De Volder, M., Losick, R., Brenner, M.P. and Weitz, D.A. (2013) Liquid transport facilitated by channels in Bacillus subtilis biofilms. Proceedings of the National Academy of Sciences 110(3), 848.

Xu, P., Bellona, C. and Drewes, J.E. (2010) Fouling of nanofiltration and reverse osmosis membranes during municipal wastewater reclamation: Membrane autopsy results from pilot-scale investigations. Journal of Membrane Science 353(1), 111-121.

Yang, Z., Zhou, Y., Feng, Z., Rui, X., Zhang, T. and Zhang, Z. (2019) A Review on Reverse Osmosis and Nanofiltration Membranes for Water Purification. Polymers 11(8), 1252.

Yaseen, T., Sun, D.-W. and Cheng, J.-H. (2017) Raman imaging for food quality and safety evaluation: Fundamentals and applications. Trends in Food Science & Technology 62, 177-189.

Youm, K.H., Fane, A.G. and Wiley, D.E. (1996) Effects of natural convection instability on membrane performance in dead-end and cross-flow ultrafiltration. Journal of Membrane Science 116(2), 229-241.

Zapata, F. and García-Ruiz, C. (2018) The discrimination of 72 nitrate, chlorate and perchlorate salts using IR and Raman spectroscopy. Spectrochimica Acta Part A: Molecular and Biomolecular Spectroscopy 189, 535-542.

Zhou, D., Zhu, L., Fu, Y., Zhu, M. and Xue, L. (2015) Development of lower cost seawater desalination processes using nanofiltration technologies — A review. Desalination 376, 109-116.

Zhou, Y. (2017a) Rayleigh–Taylor and Richtmyer–Meshkov instability induced flow, turbulence, and mixing. I. Physics Reports 720-722, 1-136.

Zhou, Y. (2017b) Rayleigh–Taylor and Richtmyer–Meshkov instability induced flow, turbulence, and mixing. II. Physics Reports 723-725, 1-160.